

# Optimal distribution of discrete heat sources in a two-dimensional data centre

---

*by*

**Thomas Christian Montgomery**

27137792

*Submitted in partial fulfilment of the requirements for the degree:*

**MASTER OF ENGINEERING (Mechanical Engineering)**

*in the*

Department of Mechanical and Aeronautical Engineering

Faculty of Engineering, Built Environment and Information Technology

University of Pretoria

2015-01-10



## Abstract

Title: Optimal distribution of discrete heat sources in a two-dimensional data centre

Author: Thomas Christian Montgomery (27137792)

Supervisors: Prof T. Bello-Ochende and Prof J.P. Meyer

Department: Mechanical and Aeronautical Engineering

University: University of Pretoria

Degree: Master of Engineering (Mechanical Engineering)

*In the study, the optimal distribution of discrete heat sources in a two-dimensional data centre was investigated. The optimal placement of the cool supply air inlet and outlet was also investigated. The governing equations were solved by using the finite volume method. The computational fluid dynamics code Fluent was used to solve the governing equations. Optimisation was achieved using a goal-driven optimisation approach and a response surface methodology.*

*The numerical model was validated using past experimental work and the results were in good agreement with each other, showing an error of less than 6%. The realisable  $k$ - $\epsilon$  turbulence model was used as closure equations to solve the Reynolds-averaged Navier-Stokes equations. Additionally, the viscosity affected near-wall regions were modelled using a wall treatment method.*

*The optimum distribution of constant height (42 U) server racks was established for three different configurations of inlet and outlet locations. After these optimal placements were established, the effect of varying the height of the server racks was investigated for the same inlet and outlet placements and the optimum locations were determined. By means of a sensitivity analysis, it was found that the placement of the first and last servers as well as their respective heights had the most influence on the heat transfer between the server panels and the ambient surroundings.*

*It was concluded that the inlet and outlet should be placed on opposing walls of the data centre and variable server rack heights should be used in order to achieve maximum heat transfer.*

**Keywords:** two-dimensional, discrete heat source, optimisation, response surface, data centre

## Acknowledgements

The author wishes to extend his gratitude to the following individuals who made this study possible:

- Professor Tunde Bello-Ochende for his guidance and support;
- Professor J.P. Meyer for his guidance and financial support;
- my wife, Yolandi, for her patience and understanding;
- my parents, Hubert and Hanlie Montgomery, for their continued support throughout the study;
- Mohammad Moghimi Ardekani for his assistance with regards to Ansys Fluent;

The funding received from the University of Pretoria, NRF, DST, TERSP, SANEDI, CSIR, EEDSM Hub and the NAC is acknowledged and duly appreciated.

# Contents

Abstract.....	i
Acknowledgements.....	ii
List of tables .....	v
List of figures.....	vi
List of symbols.....	ix
List of Greek symbols .....	x
Subscripts.....	xi
Abbreviations.....	xi
1 Introduction .....	1
1.1 Purpose of the study.....	2
1.2 Methodology.....	2
2 Literature study.....	4
2.1 Introduction .....	4
2.2 Data centre cooling strategies .....	4
2.3 CFD modelling of data centres.....	8
2.4 Optimisation .....	10
2.5 Conclusion.....	12
3 Numerical solver .....	13
3.1 Introduction .....	13
3.2 Methodology.....	13
3.3 Geometry and mesh selection .....	15
3.4 Governing equations.....	21
3.5 Solver settings.....	28
3.6 Boundary conditions and initial values .....	29
3.7 Optimisation .....	31
3.8 Conclusion.....	40

4	Validation of numerical solver .....	41
4.1	Introduction .....	41
4.2	Experimental data .....	41
4.3	CFD simulations.....	44
4.4	Comparison .....	46
4.5	Conclusion.....	48
5	Results and discussions.....	49
5.1	Introduction .....	49
5.2	Fixed server height methodology and results.....	50
5.2.1	Case A - Inlet and outlet located on walls.....	51
5.2.2	Case B - Inlet located on wall and outlet on ceiling .....	54
5.2.3	Case C – Inlet located on ceiling and outlet on wall .....	57
5.2.4	Comparison .....	60
5.3	Variable server height methodology and results.....	62
5.3.1	Case A - Inlet and outlet located on walls.....	63
5.3.2	Case B – Inlet located on wall and outlet on ceiling .....	66
5.3.3	Case C - Inlet located on ceiling and outlet on wall .....	68
5.3.4	Comparison .....	71
5.4	Conclusion.....	73
6	Conclusions and recommendations.....	77
	References .....	79
I.	Annexure A- Velocity vector plots .....	I
	Fixed server height simulations .....	I
	Variable server height simulations .....	V

## List of tables

Table 3.1: Common RANS turbulence models.....	24
Table 4.1: Mesh convergence study .....	46
Table 5.1: IBM Model 93074RX 42 U server rack dimensions.....	49
Table 5.2: Number of design parameters used for fixed server height simulations .....	51
Table 5.3: Fixed server height Case A optimal placements .....	52
Table 5.4: Fixed server height Case B optimal placements .....	55
Table 5.5: Fixed server height Case C optimal placements .....	57
Table 5.6: Number of design parameters used for variable server height simulations .....	63
Table 5.7: Variable server height Case A optimal placements .....	64
Table 5.8: Variable server height Case B optimal placements.....	66
Table 5.9: Variable server height Case C optimal placements.....	69

## List of figures

Figure 2-1: Different data centre ventilation schemes .....	5
Figure 2-2: Typical raised floor configuration .....	6
Figure 2-3: Optimal distribution of discrete heat sources on a plate with laminar forced convection	11
Figure 3-1: Typical outline of the finite volume method used to solve CFD problems .....	14
Figure 3-2: Schematic diagram showing the three main inlet and outlet configurations .....	15
Figure 3-3: Axis system used in the study.....	16
Figure 3-4: Geometry created in Ansys DesignModeler .....	17
Figure 3-5: Geometry after meshing.....	18
Figure 3-6: Close-up of mesh without added inflation layers.....	20
Figure 3-7: Close-up of mesh showing added inflation layers.....	21
Figure 3-8: Response surface optimisation outline .....	32
Figure 3-9: Example of a dimension assigned to be a design parameter .....	33
Figure 3-10: Graphical representation of the face-centred CCD method .....	34
Figure 3-11: Example of a response surface .....	35
Figure 3-12: Comparison between the response surface and verification points.....	36
Figure 3-13: Additional verification points added to the region of interest.....	37
Figure 4-1: Dimensions of the experimental room.....	42
Figure 4-2: Measured temperature values as a function of height at $x = 0.52$ m .....	43
Figure 4-3: Measured temperature values as a function of length at $y = 0.52$ m .....	43
Figure 4-4: Mesh used for validation of numerical solver .....	45
Figure 4-5: Comparison between numerical solver and experimental data at $x = L/2$ .....	47
Figure 4-6: Comparison between numerical solver and experimental data at $y = L/2$ .....	47
Figure 5-1: Fixed server height Case A 1 server rack temperature distribution.....	52
Figure 5-2: Fixed server height Case A 2 server racks temperature distribution .....	53
Figure 5-3: Fixed server height Case A 3 server racks temperature distribution .....	53
Figure 5-4: Fixed server height Case A 4 server racks temperature distribution .....	53
Figure 5-5: Fixed server height Case B 1 server rack temperature distribution .....	55
Figure 5-6: Fixed server height Case B 2 server racks temperature distribution .....	56
Figure 5-7: Fixed server height Case B 3 server racks temperature distribution .....	56
Figure 5-8: Fixed server height Case B 4 server racks temperature distribution .....	56
Figure 5-9: Fixed server height Case C 1 server rack temperature distribution .....	58

Figure 5-10: Fixed server height Case C 2 server racks temperature distribution .....	58
Figure 5-11: Fixed server height Case C 3 server racks temperature distribution .....	59
Figure 5-12: Fixed server height Case C 4 server racks temperature distribution .....	59
Figure 5-13: Comparison between fixed server height cases .....	61
Figure 5-14: Variable server height Case A 2 server racks temperature distribution .....	64
Figure 5-15: Variable server height Case A 3 server racks temperature distribution .....	65
Figure 5-16: Variable server height Case A 4 server racks temperature distribution .....	65
Figure 5-17: Variable server height Case B 2 server racks temperature distribution.....	67
Figure 5-18: Variable server height Case B 3 server racks temperature distribution.....	67
Figure 5-19: Variable server height Case B 4 server racks temperature distribution.....	67
Figure 5-20: Variable server height Case C 2 server racks temperature distribution.....	69
Figure 5-21: Variable server height Case C 3 server racks temperature distribution.....	70
Figure 5-22: Variable server height Case C 4 server racks temperature distribution.....	70
Figure 5-23: Comparison between variable server height cases .....	71
Figure 5-24: Server heat transfer comparison of all tested cases .....	74
Figure 5-25: Geometry used to determine input sensitivities.....	75
Figure 5-26: Sensitivity analysis of design parameters.....	75
Figure I-1: Fixed server height Case A 1 server rack velocity vector plot .....	I
Figure I-2: Fixed server height Case A 2 server racks velocity vector plot.....	I
Figure I-3: Fixed server height Case A 3 server racks velocity vector plot.....	II
Figure I-4: Fixed server height Case A 4 server racks velocity vector plot.....	II
Figure I-5: Fixed server height Case B 1 server rack velocity vector plot .....	II
Figure I-6: Fixed server height Case B 2 server racks velocity vector plot.....	III
Figure I-7: Fixed server height Case B 3 server racks velocity vector plot.....	III
Figure I-8: Fixed server height Case B 4 server racks velocity vector plot.....	III
Figure I-9: Fixed server height Case C 1 server rack velocity vector plot .....	IV
Figure I-10: Fixed server height Case C 2 server racks velocity vector plot.....	IV
Figure I-11: Fixed server height Case C 3 server racks velocity vector plot.....	IV
Figure I-12: Fixed server height Case C 4 server racks velocity vector plot.....	V
Figure I-13: Variable server height Case A 2 server racks velocity vector plot.....	V
Figure I-14: Variable server height Case A 3 server racks velocity vector plot.....	VI
Figure I-15: Variable server height Case A 4 server racks velocity vector plot.....	VI
Figure I-16: Variable server height Case B 2 server racks velocity vector plot.....	VI
Figure I-17: Variable server height Case B 3 server racks velocity vector plot .....	VII



Figure I-18: Variable server height Case B 4 server racks velocity vector plot .....VII

Figure I-19: Variable server height Case C 2 server racks velocity vector plot .....VII

Figure I-20: Variable server height Case C 3 server racks velocity vector plot .....VIII

Figure I-21: Variable server height Case C 4 server racks velocity vector plot .....VIII

## List of symbols

Symbol	Meaning	Units
$c$	Speed of sound	m/s
$C$	Specific heat capacity	J/kg.K
$C_f$	Skin friction	-
$D$	Diameter	m
$E$	Energy	J
$\bar{g}$	Gravitational acceleration	m/s <sup>2</sup>
$G$	Generation term	Units vary
$Gr$	Grashof number	-
$\underline{k}$	Thermal conductivity	W/m.K
$k$	Turbulent kinetic energy	m <sup>2</sup> /s <sup>2</sup>
$L$	Length	m
$M$	Mach number	-
$p$	Static pressure	Pa
$Pr$	Prandtl number	-
$R$	Gas constant	J/kg.K
$Re$	Reynolds number	-
$S_{ij}$	Mean rate-of-strain tensor	s <sup>-1</sup>
$S$	Source term	Units vary
$t$	Time	s
$T$	Temperature	K

$\mathbf{u}$	Velocity vector	m/s
$\nu$	Kinematic viscosity	m <sup>2</sup> /s
$V$	Velocity	m/s
$y$	First cell height	m
$y^+$	Non-dimensional wall distance	-

## List of Greek symbols

Symbol	Meaning	Units
$\beta$	Thermal expansion coefficient	K <sup>-1</sup>
$\delta_{ij}$	Kronecker delta	-
$\varepsilon$	Turbulent dissipation rate	m <sup>2</sup> /s <sup>3</sup>
$\varepsilon_{ijk}$	Alternating tensor	-
$\mu$	Dynamic viscosity	kg/m.s
$\mu_t$	Turbulent (eddy) viscosity	kg/m.s
$\rho$	Density	kg/m <sup>3</sup>
$\sigma$	Turbulent Prandtl number	-
$\tau$	Shear stress	kg/m.s <sup>2</sup>
$\omega$	Angular velocity	rad/s
$\overline{\Omega_{ij}}$	Mean rate-of-rotation tensor	s <sup>-1</sup>

## Subscripts

$b$	Buoyancy
$c$	Characteristic
$\varepsilon$	Turbulent dissipation rate
$h$	Hydraulic
$int$	Internal
$k$	Turbulent kinetic energy
$M$	Momentum
$p$	Pressure
$s$	Surface
$t$	Turbulent
$v$	Volume
$\infty$	Free stream

## Abbreviations

CCD	central composite design
CFD	computational fluid dynamics
CRAC	computer room air conditioning
DoE	Design of Experiments
DNS	direct numerical simulation
EWT	enhanced wall treatment

EIA	Electronic Industries Alliance
FVM	finite volume method
KKT	Karush-Kuhn-Tucker
LES	large eddy simulations
MINLP	mixed-integer non-linear programming
MISQP	mixed-integer non-linear sequential quadratic programming
MOGA	multi-objective generic algorithm
RANS	Reynolds-averaged Navier-Stokes
RMS	root mean square
RNG	renormalisation group

# 1 Introduction

The human body, like most systems, has a certain range or limits in which it is found to perform at its best. These limits can be described as thermal comfort levels. The human body continually generates heat and dissipates this heat to the surroundings by means of conduction, convection and radiation. These heat transfer mechanisms are described in greater detail below [1]:

- **Conduction:** Conduction occurs when energy, or heat, is transferred from energetic particles to less energetic particles due to the interactions between these particles. In solids, conduction occurs due to vibrations as well as the energy transported by means of electrons. In fluids, conduction occurs due to diffusion as well as collisions of molecules during random motion.
- **Convection:** Convection is the combined effects of conduction and fluid motion and occurs when energy (heat) is transferred between a solid surface and an adjacent fluid in motion. The fluid motion ensures that matter with a certain energy level moves near or over a surface with a different temperature, thereby promoting heat transfer.
- **Radiation:** When electromagnetic waves are emitted by matter as a result of configuration changes in molecules or atoms, the emitted energy is due to radiation. Radiation heat transfer does not require the presence of a medium.

Systems such as a personal computer (PC), circuit boards, server racks and everyday electronic equipment, when in operation, dissipate heat to the surrounding environment as well. Although these systems operate in a different manner from the human body, they still dissipate heat to the environment by the same three methods of convection, conduction and radiation. The driving force behind this mechanism is the change in energy from electrical energy to heat. In order to keep these systems from overheating, cool air, fans and heat sinks are used to cool these systems. The problem with these systems is that they could potentially generate so much heat that, if not properly managed, they could overheat. It quickly becomes clear that the excess heat should be managed in order to keep the system from overheating and to ensure that optimum operating conditions exist.

An example of a system or set of systems which could dissipate such a large amount of heat is the server racks found in data storage centres. Usually cool air inlets, fans and internal heat exchangers are used to cool these server racks. Therefore, the server racks are cooled or maintained at a certain temperature, by means of convection (cold air supply and fans) and conduction (heat exchangers).

In order to take full advantage of the cold air supply, these server racks should be placed in such a manner that they maximise the contact between the server rack and the cool supply air. The optimal placements of these data storage units could therefore prove to have a significant effect on the cooling efficiency of such systems and, in turn, the cost of cooling these systems.

In the study, a numerical model was investigated, validated and finally implemented to obtain the optimal placements of server racks in a small data centre. The optimal inlet and outlet locations were also investigated. In order to find the optimal distribution of servers in the data centre, Ansys DesignModeler, Ansys Meshing, Ansys Fluent and Ansys DesignXplorer were used.

## 1.1 Purpose of the study

Although numerous papers on large-scale data centres have been presented, the optimal configuration for small-scale data centres seems lacking from literature. Typically, a small business would only incorporate a few data storage racks and therefore the use of floors with plenum heights and hot aisle/cold aisle configurations is unnecessary and could prove too expensive.

The study therefore focused on small-scale data centres that typically only include one to four rows of server racks. The study therefore strived to answer the question of how the servers should be arranged to optimise their cooling. The optimal placement of the supply air inlet and outlet was also determined.

## 1.2 Methodology

This study has the following structure:

- Chapter 2 consists of a review of literature in order to determine guidelines for modelling discrete heat sources. The literature review also assists in determining the manner in which typical data centres are configured.
- In Chapter 3, the chosen numerical solver is discussed. The numerical solver was selected by studying various papers and textbooks. Also presented in Chapter 3 is the method used to obtain the optimal placements of the servers in the data centre.

- In Chapter 4, a validation of the numerical solver is presented. Validating a numerical solver ensures that the solver accurately predicts real-world problems. The numerical solver was, therefore, compared with work already done by other authors.
- Chapter 5 includes the results obtained from using the numerical solver. The results for two different scenarios are discussed as well as the trends that were concluded from the results. Sensitivity analyses are also presented in this chapter.
- Finally, Chapter 6 concludes the study. It also includes recommendations for future work that could be done in order to further this field of study.



## **2 Literature study**

### **2.1 Introduction**

This section consists of all the relevant concepts and terminology as deemed necessary to complete the dissertation. It should be noted, however, that certain basic and fundamental concepts are omitted in the literature survey due to their relative simplicity. Furthermore, the literature study gives an overview of some noted papers on data centre optimisation and distribution.

### **2.2 Data centre cooling strategies**

Server rooms or data centres utilise a number of server racks in order to capture, store, manage and exchange digital information. These server racks generate vast amounts of heat and should therefore be properly cooled. Numerous articles, papers and guidelines [2-5] have been published discussing the various cooling strategies related to data centres.

In order to maximise the cooling of electronic equipment, a variety of cooling configurations have been prescribed and implemented for both the raised and non-raised floor configurations. These configurations include a host of different computer room air-conditioning (CRAC) as well as exhaust vent placements. In order to illustrate some of the configurations used in the cooling of server rooms, consider Figure 2-1 given below.

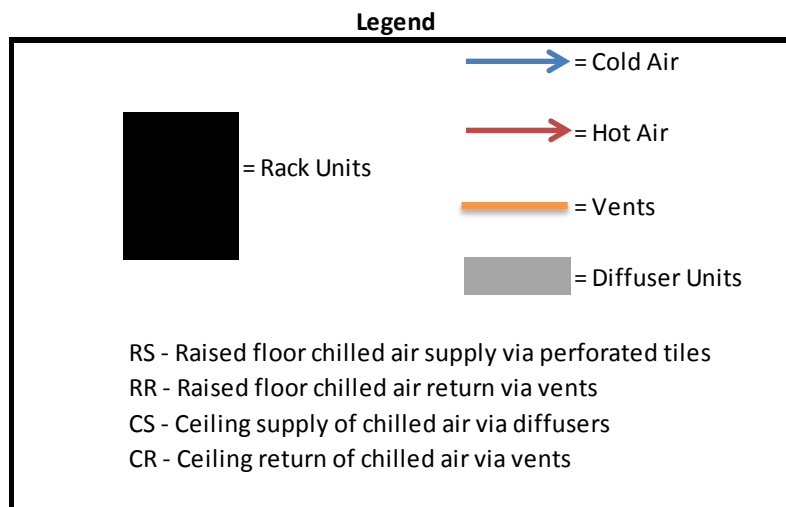
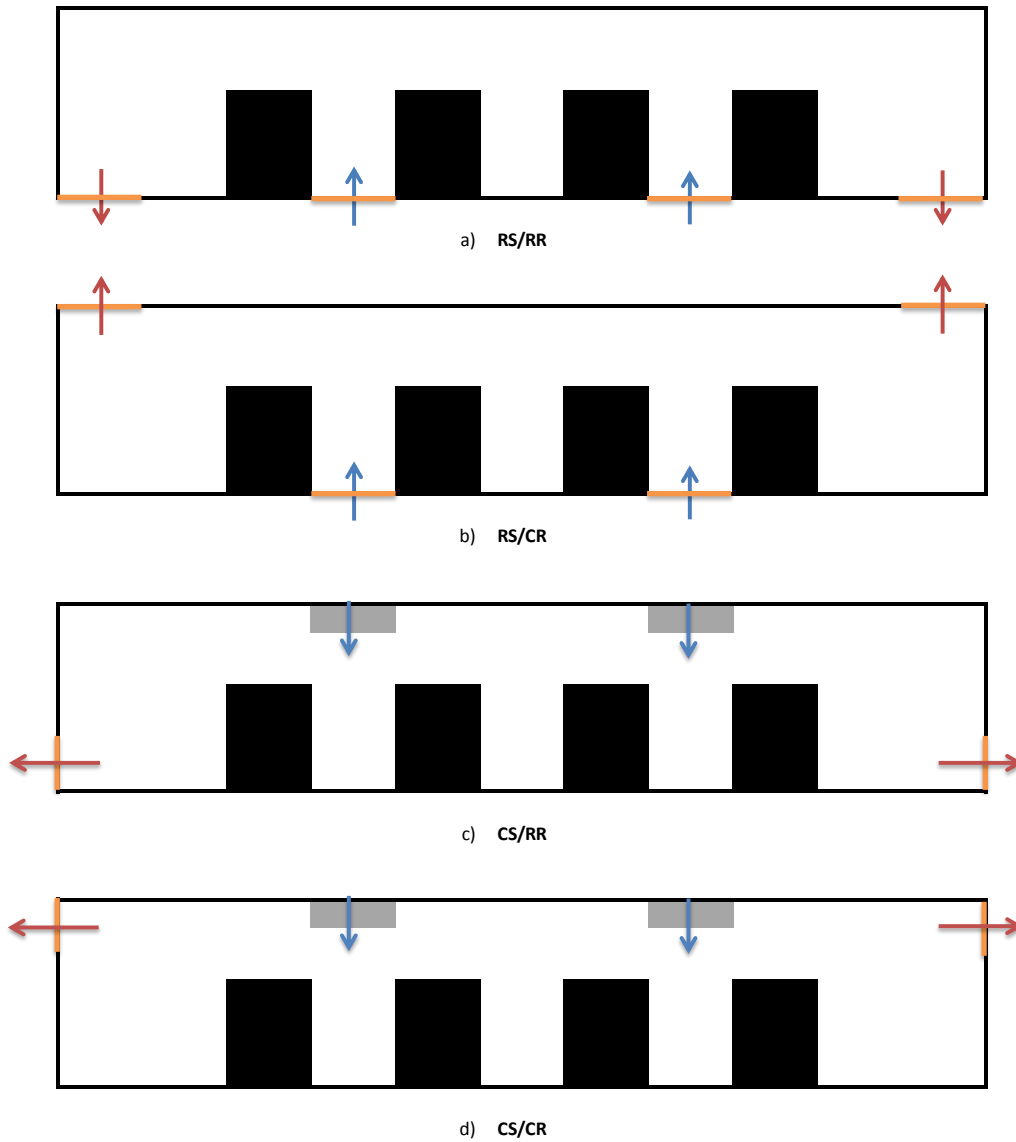


**Figure 2-1: Different data centre ventilation schemes as derived from [5]**

From Figure 2-1, it can be seen that the design is normally of either a raised or non-raised floor configuration. A typical raised floor configuration is shown in greater detail in Figure 2-2 below.

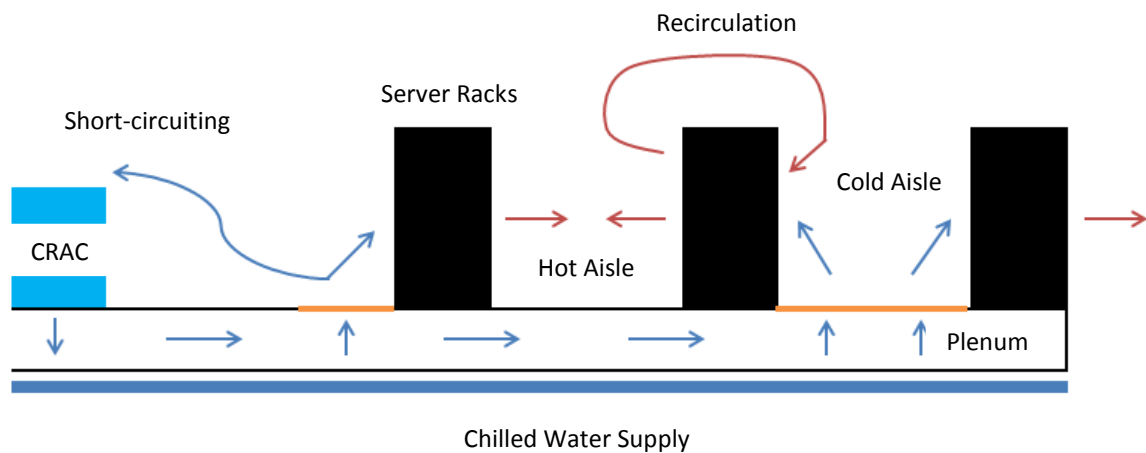


**Figure 2-2: Typical raised floor configuration as derived from [3]**

Note that in Figure 2-2, the server racks or equipment racks are spaced in such a manner as to create hot aisles (when placed back to back) and cold aisles (when facing each other). The CRAC unit then delivers a stream of cool air (blue arrows) via the raised floor to the cold aisles by means of perforated tiles (the brownish lines in Figure 2-2). Recirculation occurs in the event that the heated air (formed when the cold air supply flows through a server rack) flows to a subsequent rack and therefore nullifies the cooling effect. On the other hand, short-circuiting occurs in the event that the flow rate from the perforated tiles is too high and therefore skips the heat exchange phase altogether, as shown in Figure 2-2. This method of cooling is generally used in industry where large server rooms are present [2-6].

The raised floor design has been shown to provide higher energy-efficient cooling than non-raised floors when operating under certain configurations. However, it loses efficiency whenever operation is moved away from these optimal configurations. The non-raised floor cooling strategy is commonly found to be more efficient in small-scale data centres, since it allows for different configurations while still delivering an energy-efficient cooling load [7]. Furthermore, the traditional advantages typically associated with using a raised floor configuration are no longer some of the main concerns when dealing with data centre cooling [7]. Typically, the power cabling and water piping could be laid in the plenum created by using the raised floor configuration. Significant advances in the power supply to data centres have since been made and the need for raised floor configurations seems to be diminishing.

For small server rooms having less than 50 cabinets, the non-raised floor configuration is generally more economical with less expensive designs and more energy-efficient cooling. The non-raised floor is also favoured in the growing technological age since it does not require the additional space of a raised floor, which could rather be used to fit additional server racks [7]. Non-raised floor configurations can vary between different designs for the height of diffusers, the angle of diffusers and the air inlet and outlet locations and conditions. A typical configuration for the non-raised floor is given in Figure 2-1 c.

The studies conducted on non-raised floor cooling designs are typically concerned with the following four design parameters:

1. selection of the air-conditioning units;
2. placement of the air-conditioning units;
3. layout of the server racks;
4. height of the server racks.

The selection of the air-conditioning units to be used is often a decision between a computer room air conditioning (CRAC) unit or a built-up air handler. Most server room cooling designs [3, 5, 6, 8] employ CRAC units while very few built-up air handlers are used [9].

The placement of the CRAC units is one of the most important design parameters in cooling a data centre. Various arrangements of cold air inlets and hot air outlets have been used in the past. In this study, the optimal placement of both the cool air inlet and hot air outlet was investigated. In almost all past studies, the air inlets were placed parallel to the server rack rows [3, 5, 6, 9]. In this study, the effects of placing the inlet and outlet vents parallel to the servers were similarly investigated. Additionally, the study investigated the optimal placements of the inlet and outlet if they were placed on the ceiling of the data centre.

The layout of the server racks is the next significant design parameter. The server racks were spaced out evenly in some studies [3, 6, 9] and in other studies, the placement alternated between hot and cold aisles [8]. However, the constant hot and cold aisle designs did have a tendency to generate different zones in which the dissipated heat loads were non-uniform [6]. Patel *et al.* [4] studied the effect of having a slight perturbation from the symmetrical placement of server racks. It was found that even a slight perturbation from symmetry would result in significant differences in the overall cooling load for the CRAC units. Therefore, it should be possible to obtain an optimal distribution of server racks in the data centre, and this formed one of the main objectives of the study.

The height of the server rack is another design parameter which has not received enough attention. In most instances, case studies [6, 8, 10] were conducted based on the Electronic Industries Alliance (EIA) rack unit dimensions. In most cases, the 42 U rack was implemented with a height of 2 metres. The effect of the height of the server rack was very seldom dealt with and in various studies, no reference was made to the height or geometry of the server racks [4, 9]. The optimal distribution of 42 U (2 metre high) racks was, therefore, investigated first, after which the effect of varying the server heights was investigated.

### **2.3 CFD modelling of data centres**

Computational fluid dynamics (CFD) has become a useful method for predicting airflows in indoor environments. It offers more detail at a much lower cost than experimental studies [11]. CFD modelling involves expressing a fluid flow problem by means of equations adhering to the governing laws of physics [12]. These equations are usually solved in order to determine velocities, temperatures and pressures at various locations in the indoor environment.

When modelling fluid flow problems, it is important to note whether the flow regime is laminar or turbulent in nature. In the laminar regime, the flow is smooth with no mixing of the fluid layers. On the other hand, turbulence refers to the flow being mixed and non-uniform in nature. The transitional regime is found between the laminar and fully turbulent regime in which some mixing of the layers is present.

Because the flow regime in indoor environments tends to be turbulent in nature [11-13], the effect of turbulence on the flow field must be predicted. Since turbulence in itself is very intricate, it becomes difficult to represent mathematically. This means that the exact effects of turbulence cannot easily be presented numerically and, in turn, solved [12]. A simplified theory is, therefore, used in order to model its effects. The assumption is made that turbulent flow can be divided into its mean and fluctuating components.

It should be noted that many methods are available to predict the effects of turbulence. The Reynolds-averaged Navier-Stokes (RANS) method is, however, considered to be the most widely used turbulence modelling method. By including the mean and fluctuating components in the governing equations, additional terms known as Reynolds stresses are formed. The modified Navier-Stokes equations are then known as the RANS equations. It then becomes necessary to introduce

additional equations or closure equations in order to solve the Reynolds stresses. As expected, the computational cost involved in solving the Reynolds stresses increases as the number of additional equations increases. Therefore, a trade-off is made between accuracy and computational limits. A very popular method for solving the RANS equations is the  $k$ - $\epsilon$  model. The  $k$ - $\epsilon$  model introduces two new equations to predict the turbulent kinetic energy ( $k$ ) and the turbulent dissipation rate ( $\epsilon$ ). The  $k$ - $\epsilon$  model is also known as an eddy viscosity model.

The  $k$ - $\epsilon$  turbulence model itself is split into three popular models. The standard  $k$ - $\epsilon$  model [14] was the first of the  $k$ - $\epsilon$  models and is still used extensively to this day. The renormalisation group (RNG)  $k$ - $\epsilon$  model was first proposed by [15] and showed some improvements in certain cases with regard to the standard  $k$ - $\epsilon$  model. Finally, the realisable  $k$ - $\epsilon$  model [16] was introduced to fulfil some shortcomings of both the standard and RNG  $k$ - $\epsilon$  models. The main difference between these models is the manner in which they calculate the eddy viscosity as well as the turbulent dissipation rate ( $\epsilon$ ). Note that a more detailed explanation of the  $k$ - $\epsilon$  models follows in Section 3.4.

Numerous articles have been published on modelling indoor environments with the aforementioned  $k$ - $\epsilon$  turbulence models. [17] used the standard  $k$ - $\epsilon$  model to predict the airflow and temperature in a room with a convective heat source. The numerical results were compared with experimental values and a 1-2 °C difference was noted in the temperature predictions between the two. Zhang *et al.* [18] evaluated various turbulence models on their ability to accurately predict airflow in enclosed environments. It was found that the RNG  $k$ - $\epsilon$  model performed well with regard to the experimental values. Abanto *et al.* [19] used a realisable  $k$ - $\epsilon$  model to successfully predict the airflow in a computer room. It was also found that the numerical results were in good agreement with the experimental results.

Chen and Srebric [13] and Zhai *et al.* [11] concluded that the standard and RNG  $k$ - $\epsilon$  models can predict satisfactory results for a large selection of indoor environments. Although these papers compared the standard  $k$ - $\epsilon$  and RNG  $k$ - $\epsilon$  models, a comparison of the realisable  $k$ - $\epsilon$  model with these two models for indoor environments seems somewhat lacking in literature. However, it is noted [11] that the realisable  $k$ - $\epsilon$  model predicts the effects of buoyancy better than the standard  $k$ - $\epsilon$  model. It was, therefore, decided to use a realisable  $k$ - $\epsilon$  model to predict the effects of turbulence in the data centre.

## 2.4 Optimisation

In basic terms, optimisation is the process of determining the best solution to a certain problem while adhering to specified constraints. Optimisation is generally used to determine the solution which would either minimise effort (or loss) or maximise profit (or gain). The most basic optimisation outline is that of a standard design optimisation model [20].

In the standard design optimisation model, the objective function or cost function is determined subject to a set of equality (=) and inequality ( $\leq$ ) constraints. The goal is to find an  $n$ -vector of  $\mathbf{x} = (x_1, x_2, \dots, x_n)$  design variables that will [20]:

minimise the objective function:

$$f(\mathbf{x}) = f(x_1, x_2, \dots, x_n) \quad 2.1$$

subject to the  $p$  equality constraints:

$$h_j(\mathbf{x}) = h_j(x_1, x_2, \dots, x_n) = 0; \quad j = 1 \text{ to } p \quad 2.2$$

and the  $m$  inequality constraints:

$$g_i(\mathbf{x}) = g_i(x_1, x_2, \dots, x_n) \leq 0; \quad i = 1 \text{ to } m \quad 2.3$$

Although the standard design optimisation model is but one of numerous optimisation methods, it is important to note that the basic principles (or the outline of Equations 2.1-2.3) remain more or less the same for all design problems [20]. Not all optimisation problems are the same however, the objective function, for example, may be either constrained or unconstrained. Furthermore, these problems can be linear or non-linear as well as discrete or continuous. In order to find the optimal solutions, a large variety of techniques are used in industry. These techniques range from nature-inspired methods to meta-models. An example of each of these methods is given below.

In [21], different optimisation methods have been used to determine the optimal distribution of discrete heat sources. In this research, it was found that the heat sources (denoted by the red blocks in Figure 2-3) should be spaced close to each other at the onset of the boundary layer. It was also found that the heat sources should be spaced further apart (not uniformly) as the boundary layer grows in length.

In order to illustrate the significance of this research, consider Figure 2-3 given below. In Figure 2-3, the plate has a length  $L$  and is subject to a free-stream velocity and temperature denoted by  $V_\infty$  and  $T_\infty$  respectively.

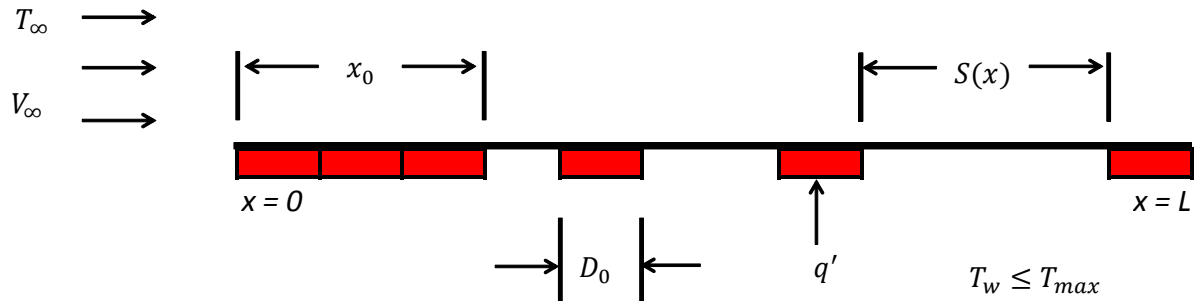


**Figure 2-3: Optimal distribution of discrete heat sources on a plate with laminar forced convection as derived from [21]**

Note that in Figure 2-3, the heat sources are line sources that extend perpendicular into the figure.  $S(x)$  refers to the heat source spacing [m] and is a function of the distance travelled along the plate length.  $D_0$  refers to the size (width) of the heat source (m), while  $q'$  denotes the heat transfer per unit length (W/m). Note that the continuously heated region in Figure 2-3 is denoted by  $x_0$ . Finally,  $T_w$  and  $T_{max}$  refer to the wall temperature and maximum allowable temperature (K) respectively.

In the study, constructal theory was applied to seek a solution. Constructal theory is a nature-inspired method of solving problems, which utilises ratios and flow patterns, for example, commonly found in the branches of trees or arteries in living beings. According to constructal theory, the entire system will perform at its best when all the elements of the system work as hard as the hardest-working element [21]. Therefore, it is assumed that if the system has a maximum allowable temperature of  $T_{max}$ , the entire system should operate at  $T_{max}$ . The solution would, therefore, be the heat source distribution, which would result in the wall temperature ( $T_w$ ) being as close as possible to the allowable maximum temperature ( $T_{max}$ ). The resulting conclusion, by inspection of Figure 2-3, is that the spacing of heat sources should increase exponentially with regard to the distance travelled along the leading edge of the plate.

A similar study was done but for a vertical plate (or wall) with natural convection [22]. The study concluded that the heat source spacing should increase exponentially with regard to the distance travelled along the height of the plate (or wall). Therefore, it can therefore be concluded from these two studies that the heat sources should not necessarily be spaced equal distances apart.



In optimum design, the effect of a change in input parameter on the outcome of the solution (or the response) is of great importance. To construct a detailed model able to accurately predict any response could quickly prove too expensive in computational resources. In order to solve this problem, meta-models are introduced. The meta-models act as an approximation of the actual model, thereby greatly reducing the computational resources needed to predict a response. A popular meta-model used extensively in industry is a response surface meta-model. The response surface is therefore an approximation of the system's response to input design parameter changes.

Once a response surface has been generated, optimisation algorithms can be applied to the response surface in order to yield optimum results. In [23], the optimal distribution of heat sources in a vented enclosure was successfully determined using a response surface method of optimisation. A response surface mimics an actual function by means of a surface fit through experimentally determined points.

The process of response surface optimisation is discussed in greater detail in Section 3.7. A response surface optimisation technique was used to determine the optimal distribution of server racks in the data centre.

## 2.5 Conclusion

This chapter provided an insight into some of the past work done involving data centres. Typical data centre cooling strategies were discussed as well as how to model turbulence in indoor environments using a CFD code. A brief overview of optimisation strategies was also provided.

With the literature review now complete, the next step in the study was to select a numerical solver.

## 3 Numerical solver

### 3.1 Introduction

Computational fluid dynamics (CFD) programs incorporate certain governing equations to solve problems regarding fluid or solid behaviour. CFD packages are widely used in industry today due to their relative simplicity, cost and flexibility. CFD programs become especially favourable if large quantities of repetitive calculations are needed. For example, consider having to determine the temperature at a specific location in a room. By correctly modelling the room in CFD, the temperature could be calculated at different locations throughout the room. Having to determine the temperature experimentally would involve temperature sensors (such as thermocouples) placed strategically throughout the entire room. This could not only prove expensive, but extremely time consuming as well.

Therefore, it becomes clear that CFD has significant potential if utilised correctly. However, it must be noted that, if possible, CFD should not be used as the sole solution to a problem, but should be verified and validated by means of experimental procedures and theory. This chapter explains the various methods used to set up and solve numerical problems. A brief overview is also given of the difference between solvers. The following sections are based on the work of Versteeg and Malalasekera [24] as well as the Ansys Fluent User's Guide [25].

### 3.2 Methodology

In general, three major methods or techniques are followed to yield numerical results. These methods are as follow: i) finite difference methods, ii) finite element methods and iii) spectral methods [24]. A special case of the finite difference method is the finite volume method and is most commonly used in CFD solvers. Although two or more methods could yield the same numerical results, the outline of the problem normally dictates which solver will be the easiest and most cost effective to use.

In general, the finite volume method utilises the following sequence of steps, as shown in Figure 3-1 below, to solve numerical problems [25]:

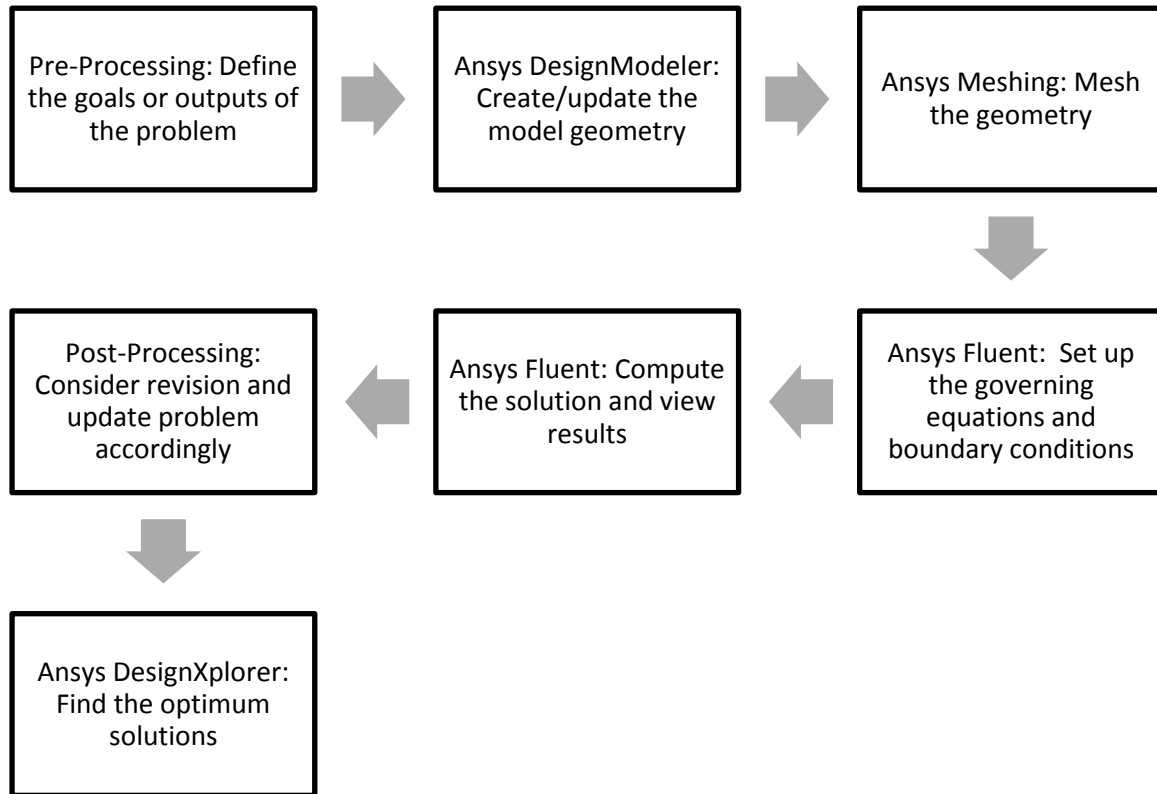


**Figure 3-1: Typical outline of the finite volume method used to solve CFD problems**

In the case of this study, the finite volume method (FVM) was used to determine the temperature and velocity fields in the data centre. The finite volume method was chosen due to familiarity and relative ease of use.

In order to determine the optimal distribution of servers in the data centre, three different inlet and outlet configurations were chosen to investigate. These configurations are shown in Figure 3-2 below. Case A had the inlet and the outlet on the left and right walls of the data centre respectively. In Case B, the outlet was moved to the ceiling of the data centre. Case C featured the inlet on the ceiling and the outlet was moved back to the right wall of the data centre. Note that more detail of the data centre dimensions as well as choices follows in subsequent chapters.

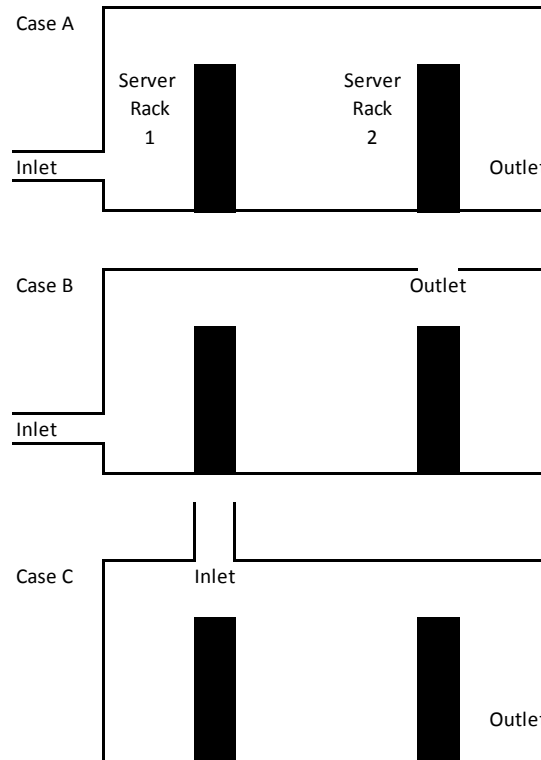


**Figure 3-2: Schematic diagram showing the three main inlet and outlet configurations**

The inlet and outlet configurations were based on previous studies and would ensure that a variety of configurations was tested. With the main configurations set, the next step was to determine accurate dimensions to assign to the data centre.

### 3.3 Geometry and mesh selection

The second step (in Figure 3-1) in a typical CFD simulation is to create the needed geometry or physical problem domain. The geometry should accurately describe the problem at hand and should be as realistic as possible. It is worthwhile to note that in this case, the geometry would be the fluid itself. This means that in the data centre, the profile of the enveloped air would form the geometry of the study. Figure 3-3 below shows the axis system that was used for the study. Note that the gravitational acceleration  $\bar{g}$  was assumed to work in the negative  $y$ -direction at all times, as shown in Figure 3-3 below.

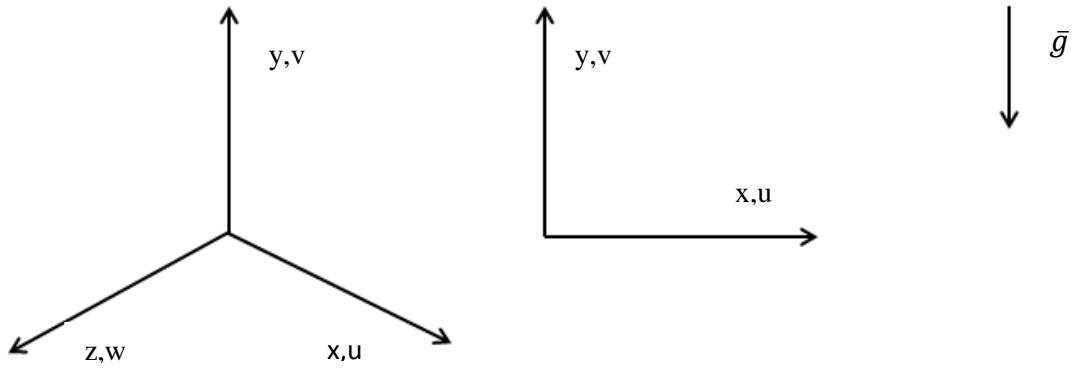


**Figure 3-3: Axis system used in the study**

As previously mentioned, the data centre in this case did not include a raised floor configuration. Although a small data centre could utilise a raised floor configuration, the idea was to simulate a typical room in an office environment that would at most have four rows of server racks.

In order to better understand the geometry of the data centre, refer to Figure 3-4 given below. Note that the dimensions of the data centre were loosely based on the dimensions of the experimental room at Hewlett Packard's Richardson site [10]. These dimensions were deemed realistic for a small-scale data centre. The dimensions for the length, width and height of the data centre were 7 m, 5 m and 3 m respectively. An inlet and outlet were also added to the data centre and both their heights were chosen to be 0.5 m. The geometry was created in Ansys DesignModeler and is given in Figure 3-4 below. In this case, the server (data) racks were taken to have standard 42 U rack dimensions of 2 m, 1 m and 0.6 m for the height, length and width respectively [26].

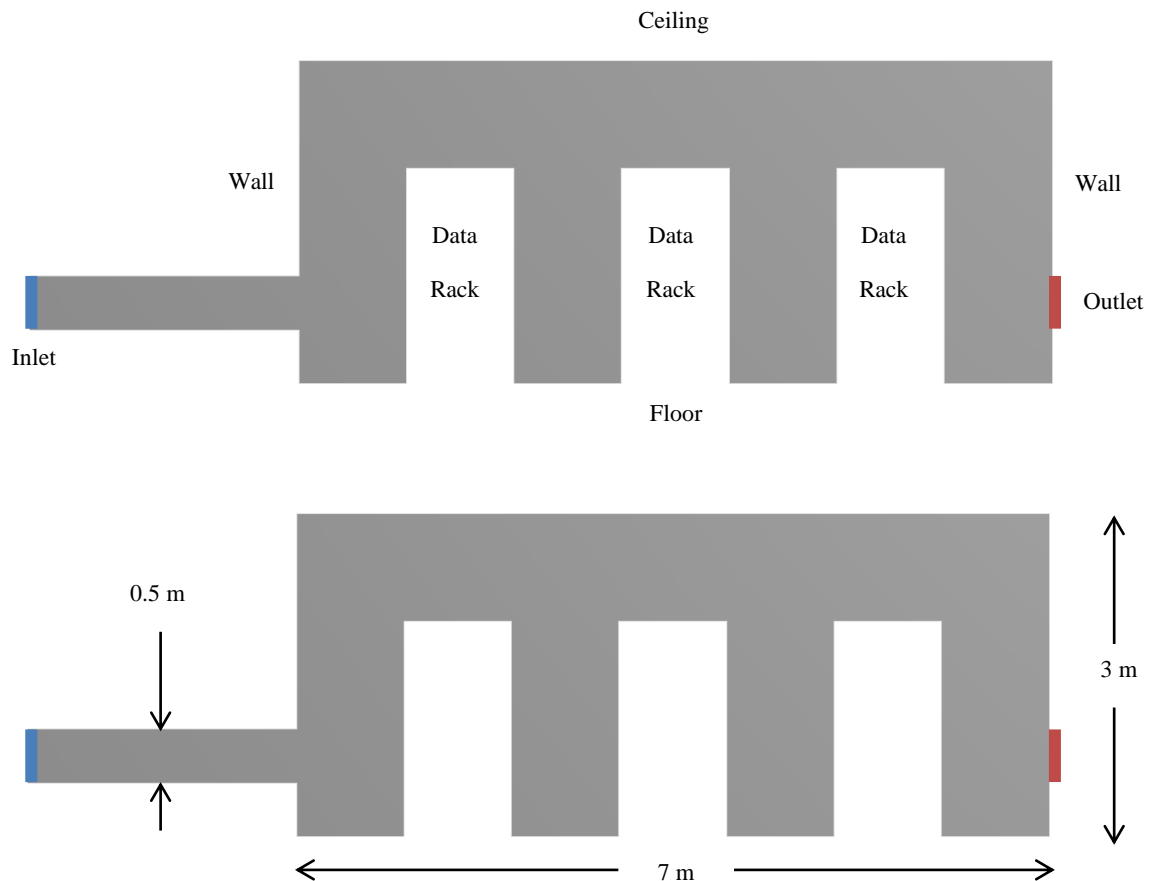


**Figure 3-4: Geometry created in Ansys DesignModeler**

Note that the elongated inlet as shown in Figure 3-4 above was inserted to ensure that the cool air would enter the room in a parabolic fashion. This approach is more realistic than simply having a uniform velocity inlet. The same effect could have been achieved by setting the inlet to a parabolic inlet, but since the height of the inlet itself was set to a design parameter (and could therefore move freely), it was easier to simply model an additional length of ducting. The method of setting a parabolic inlet requires that the exact coordinates of the inlet be known, which, since the inlet can move vertically up and down the wall, makes it somewhat more difficult than modelling the additional section of duct.

Once the geometry was created, the next step (in Figure 3-1) was to mesh the geometry. Meshing is the process of dividing the geometry into smaller control volumes and is done in order to obtain discretised equations for each of the small control volumes known as cells.

It is important to note that the forms of the control volumes differ between two-dimensional and three-dimensional geometries. For the case of a two-dimensional geometry, the cells are typically triangular or quadrilateral in nature. In the study, quadrilateral cells were chosen to construct the mesh. The size or quality of the mesh forms another crucial input to the CFD problem at hand. Normally, the finer the mesh becomes, the better or more realistic the solutions are. Therefore, it is important to construct a mesh that is fine enough to solve the problem accurately, but, in turn, the mesh should ideally not use more computational resources than is deemed necessary. To help solve the problem, a concept is introduced known as a “mesh refinement study”. A mesh refinement study typically involves choosing a mesh size and calculating the solution. The mesh is then refined and the new results are recorded. This process is repeated until the difference in subsequent results is deemed small enough by the user.

The mesh in this case was created in Ansys Meshing. In order to illustrate the two-dimensional mesh with three rows of server racks, consider Figure 3-5 given below. Note that this is the same geometry as given in Figure 3-4, but the geometry has since undergone meshing.

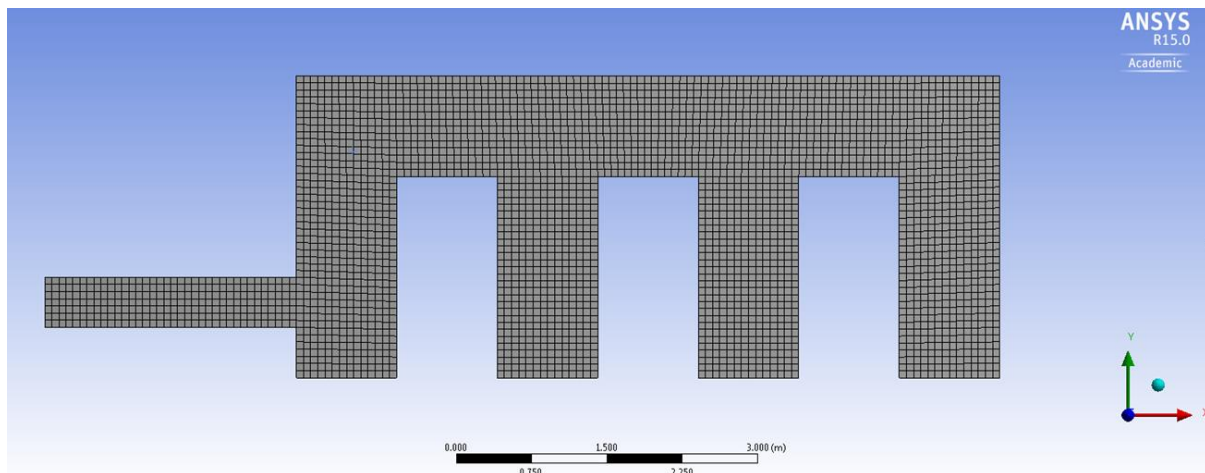


**Figure 3-5: Geometry after meshing**

Note that in Figure 3-5, the mesh is purely quadrilateral in nature. Although this mesh size was determined to be sufficient, by means of a mesh refinement study (an example of which is shown later in the dissertation), it was decided to include inflation layers on all the boundaries as well. Inflation layers were added to the boundaries because higher gradients or differences were expected in these regions. The fluid in contact with the walls, for example, will have a zero velocity due to the no-slip conditions imposed at the wall. However, just a few millimetres inside the fluid

domain, a high velocity might be experienced by the fluid. To ensure that this region was accurately modelled, the number of cells in the near-wall region was increased. The simplest way to refine the cells at the wall is to add inflation layers.

Generally, the near-wall region can be subdivided into three layers. The layer bordering the wall is called the viscous sublayer and molecular viscosity plays an important role in this layer. The furthestmost layer is the fully turbulent layer and is largely considered with the effects of turbulence. Between these two layers exists a buffer zone in which the effects of turbulence and molecular viscosity are equally important [25]. To ensure that the model successfully predicts flows in these regions, either a wall function or a wall treatment method is used. The wall function approach models the viscous sublayer and buffer zone via semi-empirical formulae known as wall functions [23]. It is important to note, however, that wall functions tend to deteriorate when buoyancy effects are present. Alternatively, a wall treatment methodology can be followed to fully resolve the viscosity-affected near-wall regions [23]. The wall treatment method can be more accurate than the wall function method, but care should be taken because the use of wall treatments requires the mesh to be refined in the near-wall regions, thereby increasing computational resources. In the study, the enhanced wall treatment (EWT) was used in Ansys Fluent since buoyancy effects would be present.

The height of the first cell centroid ( $y$ ) can be calculated using Equation 3.1 given below [25]:

$$y = \frac{y^+ \mu}{U_\tau \rho} \quad 3.1$$

in which  $\mu$  is the dynamic viscosity and  $\rho$  the density of the fluid. Furthermore,  $y^+$  is a non-dimensional wall distance and  $U_\tau$  is a velocity calculated using Equation 3.2 below [25]:

$$U_\tau = \sqrt{\frac{\tau_{wall}}{\rho}} \quad 3.2$$

Note that in Equation 3.2,  $\tau_{wall}$  is the wall shear stress and, in turn, is calculated using Equation 3.3 below [1]:

$$\tau_{wall} = 0.5 \rho C_f V_\infty^2 \quad 3.3$$

where  $C_f$  denotes skin friction and  $V_\infty$  the free-stream velocity of the fluid. Finally,  $C_f$  is calculated from [1]:

$$C_f = 0.058 Re^{-0.2} \quad 3.4$$



In Equation 3.4,  $Re$  is the non-dimensional Reynolds number and is the ratio of inertia forces to viscous forces acting on a fluid element calculated as follows [1]:

$$Re = \frac{\rho V_{\infty} L_c}{\mu} \quad 3.5$$

in which  $L_c$  is the characteristic length of the geometry.

The non-dimensional wall distance should be less than five ( $y^+ < 5$ ) in order to take full advantage of the EWT [23]. Although the first cell height was checked in the post-processing stage, a calculation was done using Equations 3.1-3.5 in order to obtain satisfactory initial values for the first layer thickness. The calculation assumed a dimensionless wall distance of four in order to minimise the increase in computational resources caused by using EWT. In this case, the server racks were taken to have standard 42 U rack dimensions of 2 m, 1 m and 0.6 m for the height, length and width respectively [26]. Furthermore, the free-stream velocity was assumed to be 1 m/s and the density and dynamic viscosity were taken at 20 °C (293.15 K) and 1 atmosphere pressure to be 1.204 kg/m<sup>3</sup> and 1.825e-5 kg/m.s respectively [1]. By using these values and Equations 3.1-3.5, the first cell centroid was calculated to be

$$y \approx 0.00115 \text{ m}$$

However, note that this is only the distance from the wall to the centre of the cell, the first layer thickness is twice this distance and so it was established that the first layer height should be 0.0023 m. Given in Figure 3-6 below is an example of the mesh before inflation layers were added. Figure 3-7, in turn, shows the same close-up view of the geometry with inflation layers now added.

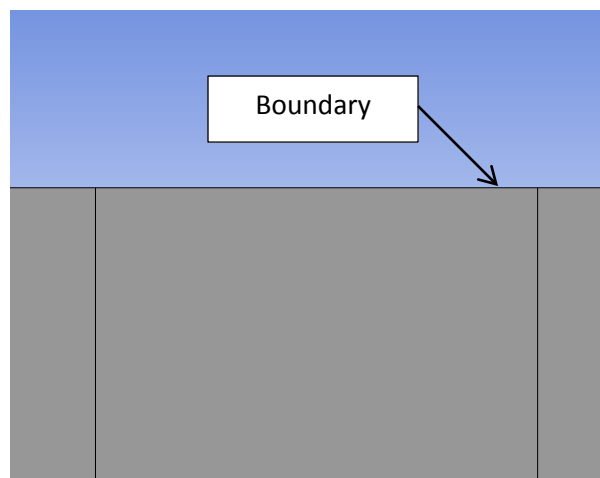


**Figure 3-6: Close-up of mesh without added inflation layers**

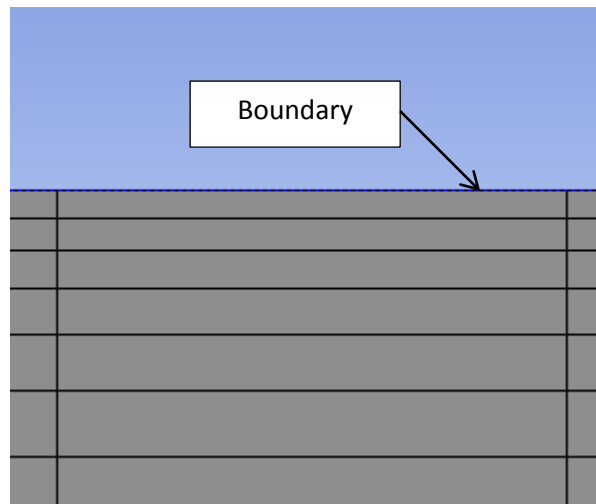


**Figure 3-7: Close-up of mesh showing added inflation layers**

After the inflation layers were added to the mesh, the number of cells almost doubled (from approximately 6 500 cells to 11 477 cells), but still fell within the acceptable computational limitations and did not show a significant increase in computational time. With the geometry and mesh now complete, the next step was to determine the governing equations that would be used.

### **3.4 Governing equations**

In order to obtain accurate results, the governing equations should be fully understood. These equations are applied to each cell in the meshed geometry in order to ensure that, on a cell-by-cell basis, the continuity laws are fulfilled. The basic conservation laws of physics must be kept at all times and are as follows [24]:

- The mass of a fluid must be conserved.
- The rate of change of momentum must be equal to the forces acting on a fluid particle (this is also known as Newton's second law).
- The rate of change of energy must be equal to the sum of heat addition and work done on the system (this is also known as the first law of thermodynamics).

From these laws, governing equations to which each cell must conform can be derived. The most basic of these governing equations are the conservation of mass (or continuity) equation and the momentum equations respectively, given below in Equations 3.6-3.9 [24]:

$$\frac{\partial \rho}{\partial t} + \nabla \cdot (\rho \mathbf{u}) = 0 \quad 3.6$$

in which  $\mathbf{u}$  is the velocity field with components (u, v, w) in the x-, y- and z-directions respectively.

The momentum equations for a compressible Newtonian fluid are given by [24]:

$$\text{x-momentum: } \frac{\partial}{\partial t} (\rho u) + \nabla \cdot (\rho u \mathbf{u}) = -\frac{\partial p}{\partial x} + \nabla \cdot (\mu \nabla u) + S_{Mx} \quad 3.7$$

$$\text{y-momentum: } \frac{\partial}{\partial t} (\rho v) + \nabla \cdot (\rho v \mathbf{u}) = -\frac{\partial p}{\partial y} + \nabla \cdot (\mu \nabla v) + S_{My} \quad 3.8$$

$$\text{z-momentum: } \frac{\partial}{\partial t} (\rho w) + \nabla \cdot (\rho w \mathbf{u}) = -\frac{\partial p}{\partial z} + \nabla \cdot (\mu \nabla w) + S_{Mz} \quad 3.9$$

in which  $S_M$  is the momentum source,  $\mu$  is the dynamic viscosity and the static pressure is denoted by  $p$ .

The energy equation is used to determine the energy of a fluid. This equation takes into consideration the internal energy, kinetic energy and gravitational potential energy of a fluid. The energy equation for a compressible Newtonian fluid is given in Equation 3.10 below [24]:

$$\frac{\partial (\rho E_{int})}{\partial t} + \nabla \cdot (\rho E_{int} \mathbf{u}) = -p \nabla \cdot \mathbf{u} + \nabla \cdot (\underline{k} \nabla T) + \Omega + S \quad 3.10$$

where  $E_{int}$  is the internal energy of the fluid and  $\Omega$  denotes the dissipation function given below [24]. Furthermore,  $\underline{k}$  is used to denote the thermal conductivity of the medium and  $S$  is used to denote a source term.

$$\Omega = \mu \left\{ 2 \left[ \left( \frac{\partial u}{\partial x} \right)^2 + \left( \frac{\partial v}{\partial y} \right)^2 + \left( \frac{\partial w}{\partial z} \right)^2 \right] + \left( \frac{\partial u}{\partial y} + \frac{\partial v}{\partial x} \right)^2 + \left( \frac{\partial u}{\partial z} + \frac{\partial w}{\partial x} \right)^2 + \left( \frac{\partial v}{\partial z} + \frac{\partial w}{\partial y} \right)^2 \right\} + \lambda (\nabla \cdot \mathbf{u})^2$$

$\lambda$  refers to the second viscosity of the fluid. The second viscosity can be omitted in the case of incompressible fluids.

It then became important to check whether or not the flow would behave in a laminar or turbulent manner. In order to determine the regime of the flow, the Reynolds number was calculated at the inlet of the data centre. The non-dimensional Reynolds number is given by [1]:

$$Re = \frac{\rho V_{\infty} D_h}{\mu} \quad 3.11$$

where  $V_{\infty}$  and  $D_h$  refer to the free-stream velocity and the hydraulic diameter of the duct respectively. For rectangular ducts, however, the hydraulic diameter is calculated from [1]:

$$D_h = \frac{(2)(duct\ height)(duct\ width)}{(duct\ height + duct\ width)} \quad 3.12$$

Assuming a duct height of 0.5 m, width of 1 m and a constant inlet velocity of 1 m/s, the density and dynamic viscosity are found (at a temperature of 298.15 K) to be 1.184 kg/m<sup>3</sup> and 1.849 x 10<sup>-5</sup> kg/m.s respectively [1]. This means that Equation 3.11 reduces to:

$$Re = \frac{(1.184)(1)(0.667)}{1.849e-5}$$

$$Re \approx 42\,711$$

The critical Reynolds number at which flow is deemed fully turbulent is given as 10 000 [1]. Since the Reynolds number is much larger than 10 000, fully turbulent flow is expected and the governing equations will therefore be modified to incorporate these effects.

Various methods may be implemented to solve turbulence in CFD models and normally the problem itself dictates which solver to use. Of all the methods used to predict turbulence, three have seen widespread use over the years. The three methods are as follows i) direct numerical simulation (DNS), ii) large eddy simulation (LES) and iii) Reynolds-averaged Navier-Stokes (RANS) simulation [24].

In DNS, the mean flow and all fluctuations are calculated. This method uses time steps small enough to determine the period of the fastest fluctuations [24]. Although this method typically yields very accurate results, the computational cost involved in this method normally exceeds the cost of the other two methods and it could potentially become too expensive to incorporate into industry.

LES focuses on the larger turbulent eddies by rejecting some of the turbulent effects at the smaller eddies. In this method, unsteady flow equations are solved and the computational resources are quite large (although in most cases not as great as DNS) [24].

In RANS simulations, the main emphasis is placed on the mean flow and the turbulent effects on these properties. The first step in this method is to take the time average of the Navier-Stokes equations. Once the time- (or Reynolds) averaged flow equations have been determined, extra terms appear in these equations that must be modelled with classic turbulence models [24]. This method has seen widespread use and was used in the study due to familiarity as well as computational resources.

In order to utilise the RANS methodology, the flow variables are replaced by the sum of the mean and fluctuating components [24]. For example, in Equation 3.7, the velocity  $u$  will be replaced by a mean and fluctuating component. The new form of  $u$  is given in Equation 3.13 below [25]:

$$u = \bar{u} + u' \tag{3.13}$$

with  $\bar{u}$  and  $u'$  denoting the mean and fluctuating components respectively. The same principle is applied to vectors.

In order to further simplify the mathematics involved in deriving equations, the Cartesian tensor notation (or suffix notation) is used. When using this notation,  $i$  or  $j = 1$  refers to the  $x$ -direction,  $i$  or  $j = 2$  the  $y$ -direction and  $i$  or  $j = 3$  the  $z$ -direction. By using the aforementioned notation and substituting Equation 3.13 into Equations 3.6-3.9, a new set of governing equations is found. The time average is then taken and the overbar on the mean velocity is dropped. The result is the RANS equations as given in Equations 3.14 and 3.15 below [25]:

Continuity:

$$\frac{\partial \rho}{\partial t} + \frac{\partial}{\partial x_i}(\rho u_i) = 0 \quad 3.14$$

Momentum:

$$\frac{\partial}{\partial t}(\rho u_i) + \frac{\partial}{\partial x_j}(\rho u_i u_j) = -\frac{\partial p}{\partial x_i} + \frac{\partial}{\partial x_j} \left[ \mu \left( \frac{\partial u_i}{\partial x_j} + \frac{\partial u_j}{\partial x_i} - \frac{2}{3} \delta_{ij} \frac{\partial u_l}{\partial x_l} \right) \right] + \frac{\partial}{\partial x_j}(-\rho \overline{u'_i u'_j}) \quad 3.15$$

Note that in Equation 3.15,  $\delta_{ij}$  is known as the Kronecker delta and has a value of 1 if  $i = j$  and 0 when  $i \neq j$ .

Note that in Equation 3.15, six additional unknown variables have now emerged. These unknowns in the momentum equations are referred to as the Reynolds stresses and are given by  $-\rho \overline{u'_i u'_j}$ . These unknown variables must be solved in order to use the RANS method. The RANS method is the most common method used to predict turbulence in CFD problems [27]. In order to solve these unknown variables, additional equations (known as turbulence models) are introduced and solved in conjunction with the RANS equations. The most popular turbulence models are given in Table 3.1 below [24].

**Table 3.1: Common RANS turbulence models [24]**

Name	Number of additional transport equations
Mixing length model	Zero
Spalart-Allmaras model	One
$k$ - $\epsilon$ model	Two
$k$ - $\omega$ model	Two
Reynolds stress model	Seven

The most commonly used and validated turbulence models given in Table 3.1 are the mixing length model and the  $k$ - $\varepsilon$  model [24]. Generally, the solution becomes more accurate if more transport equations are introduced. However, as the number of equations increases, so does the computational cost associated with the problem. Therefore, it becomes important to choose a turbulence model that will conform to the user's time and computational constraints. In this case, the  $k$ - $\varepsilon$  turbulence model was used due to familiarity and computational limits.

The  $k$ - $\varepsilon$  turbulence model, in turn, is divided into three separate models, namely: i) the standard  $k$ - $\varepsilon$  model, ii) the renormalisation group  $k$ - $\varepsilon$  (RNG) model and iii) the realisable  $k$ - $\varepsilon$  model. These three methods differ in calculation of the eddy viscosity, as well as the turbulent dissipation rate (discussed in greater detail below). The realisable  $k$ - $\varepsilon$  model has shown significant improvements over the other  $k$ - $\varepsilon$  turbulence models in certain conditions [25]. Due to the nature of the flow in the data centre, it was decided to use the realisable  $k$ - $\varepsilon$  turbulence model.

All the  $k$ - $\varepsilon$  turbulence models use the Boussinesq approach to solve the Reynolds stresses in Equation 3.15. The Reynolds stresses are solved using Equation 3.16 given below [25]. Most of the previous published work studied also used the Boussinesq approach [28-30].

$$-\rho \overline{u_i' u_j'} = \mu_t \left( \frac{\partial u_i}{\partial x_j} + \frac{\partial u_j}{\partial x_i} \right) - \frac{2}{3} \left( \rho k + \mu_t \frac{\partial u_k}{\partial x_k} \right) \delta_{ij} \quad 3.16$$

The eddy viscosity  $\mu_t$  is computed as a function of the turbulent kinetic energy  $k$ , as well as the turbulent dissipation rate  $\varepsilon$ , giving rise to the two new transport equations as previously discussed. The equations used to compute  $k$  and  $\varepsilon$  in the case of the realisable  $k$ - $\varepsilon$  model are given below [25]:

$$\frac{\partial}{\partial t} (\rho k) + \frac{\partial}{\partial x_j} (\rho k u_j) = \frac{\partial}{\partial x_j} \left[ \left( \mu + \frac{\mu_t}{\sigma_k} \right) \frac{\partial k}{\partial x_j} \right] + G_k + G_b - \rho \varepsilon - Y_M + S_k \quad 3.17$$

and

$$\frac{\partial}{\partial t} (\rho \varepsilon) + \frac{\partial}{\partial x_j} (\rho \varepsilon u_j) = \frac{\partial}{\partial x_j} \left[ \left( \mu + \frac{\mu_t}{\sigma_\varepsilon} \right) \frac{\partial \varepsilon}{\partial x_j} \right] + \rho C_1 S \varepsilon - \rho C_2 \frac{\varepsilon^2}{k + \sqrt{v \varepsilon}} + C_{1\varepsilon} \frac{\varepsilon}{k} C_{3\varepsilon} G_b + S_\varepsilon \quad 3.18$$

with

$$C_1 = \max \left[ 0.43, \frac{S_\varepsilon^k}{S_\varepsilon^k + 5} \right], \quad S = \sqrt{2 S_{ij} S_{ij}} \quad \text{and} \quad C_{3\varepsilon} = \tanh \frac{V_{\parallel}}{V_{\perp}}$$

Note that in Equations 3.17 and 3.18,  $\sigma_k$  and  $\sigma_\varepsilon$  are the turbulent Prandtl numbers for  $k$  and  $\varepsilon$  respectively. Furthermore,  $G_k$  is the generation of turbulent kinetic energy due to velocity

gradients, while  $G_b$  is used to denote the generation of turbulent kinetic energy due to buoyancy.  $Y_M$  is the ratio of fluctuating dilatation to the overall dissipation rate, which is normally neglected for incompressible flows.  $S_k$  and  $S_\varepsilon$  are user-defined source terms.  $V_{\parallel}$  and  $V_{\perp}$  are used to denote the velocity components parallel and perpendicular to the gravitational vector respectively. Finally,  $C_{1\varepsilon}$  and  $C_2$  are constants and  $S_{ij}$  is the mean rate-of-strain tensor [25].

The eddy (or turbulent) viscosity  $\mu_t$  in Equation 3.16 is then calculated using Equation 3.19 given below [25]:

$$\mu_t = \rho C_\mu \frac{k^2}{\varepsilon} \quad 3.19$$

The realisable  $k$ - $\varepsilon$  model differs from the standard and RNG  $k$ - $\varepsilon$  models in the sense that  $C_\mu$  is no longer treated as a constant, but is evaluated from Equation 3.20 given below [25]:

$$C_\mu = \frac{1}{A_0 + A_s \frac{kU^*}{\varepsilon}} \quad 3.20$$

with

$$U^* = \sqrt{S_{ij}S_{ij} + \tilde{\Omega}_{ij}\tilde{\Omega}_{ij}}$$

where

$$\tilde{\Omega}_{ij} = \Omega_{ij} - 2\varepsilon_{ijk}\omega_k \quad \text{and} \quad \Omega_{ij} = \overline{\Omega}_{ij} - \varepsilon_{ijk}\omega_k$$

$\overline{\Omega}_{ij}$  is the mean rate-of-rotation tensor with an angular velocity  $\omega$ . The alternating tensor or permutation symbol  $\varepsilon_{ijk}$  has a value of 0 if any two indices are the same. The alternating tensor has a value of 1 when indices are distinct (not the same) and cyclic ( $\varepsilon_{123}$ ,  $\varepsilon_{231}$  and  $\varepsilon_{312}$ ). Finally, the alternating tensor has a value of -1 if the indices are distinct and not cyclic ( $\varepsilon_{132}$ ,  $\varepsilon_{213}$  and  $\varepsilon_{321}$ ). The constants  $A_0$  and  $A_s$  are given below [25]:

$$A_0 = 4.04 \quad \text{and} \quad A_s = \sqrt{6} \cos \phi$$

with

$$\phi = \frac{1}{3} \cos^{-1}(\sqrt{6}W)$$

In turn,

$$W = \frac{S_{ij}S_{jk}S_{ki}}{\tilde{S}^3} \quad \text{and} \quad \tilde{S} = \sqrt{S_{ij}S_{ij}}$$

And finally, the mean rate-of-strain tensor is calculated from

$$S_{ij} = \frac{1}{2} \left( \frac{\partial u_j}{\partial x_i} + \frac{\partial u_i}{\partial x_j} \right)$$

The model constants  $\sigma_k = 1$ ,  $\sigma_\varepsilon = 1.2$ ,  $C_{1\varepsilon} = 1.44$  and  $C_2 = 1.9$  have been evaluated in Ansys Fluent for a wide variety of cases. These default values were also used in the simulations.

With the governing equations now derived, the next step is to determine whether or not compressibility of the fluid could occur. To do this, the Mach number needs to be calculated. According to [25], the Mach number is given by:

$$M = \frac{v}{c} \tag{3.21}$$

in which  $c$  is the speed of sound in the fluid. The speed of sound is calculated from [31]:

$$c = \sqrt{\frac{C_p}{C_v} RT} \tag{3.22}$$

$C_p$  and  $C_v$  refer to the specific heat capacities at a constant pressure and volume respectively while  $R$  is the gas constant of the fluid. As a quick check, it is determined that  $\frac{C_p}{C_v} = 1.4$  and  $R = 287 \frac{J}{kgK}$  of air at 25 °C and 100kPa [32]. Therefore, Equation 3.22 can be rewritten as

$$c = \sqrt{(1.4)(287)(298.15)}$$

$$c = 346.12 \frac{m}{s}$$

Now if the maximum velocity into the server room is assumed to be 1 m/s, then the Mach number is approximately equal to

$$M = \frac{1}{346.12}$$

$$M = 0.0289$$

It can therefore be seen that the Mach number in this case is significantly less than unity. This means that the flow is subsonic and the effects of compressibility can safely be ignored [25]. Slight variations in density will still be present, seeing that density is also a function of temperature, and the driving force behind buoyancy effects. However, the above calculations showed that these fluctuations would be minimal in nature. Seeing that the flow can now be modelled as



incompressible, steady and two-dimensional, the governing RANS equations are significantly simplified. These simplified equations are given in Equations 3.23 and 3.24 below:

*Continuity equation:*

$$\rho \frac{\partial u_i}{\partial x_i} = 0 \quad 3.23$$

*Momentum equation:*

$$\rho \frac{\partial}{\partial x_j} (u_i u_j) = -\frac{\partial p}{\partial x_i} + \frac{\partial}{\partial x_j} \left[ \mu \left( \frac{\partial u_i}{\partial x_j} + \frac{\partial u_j}{\partial x_i} - \frac{2}{3} \delta_{ij} \frac{\partial u_l}{\partial x_l} \right) \right] + \frac{\partial}{\partial x_j} (-\rho \overline{u'_i u'_j}) \quad 3.24$$

Apart from the RANS equations, the energy equation is also significantly simplified and can be rewritten as:

$$\rho C_p \left( \frac{\partial u_i T}{\partial x_j} \right) = \frac{\partial}{\partial x_i} (\underline{k} + \underline{k}_t) \frac{\partial T}{\partial x_i} \quad 3.25$$

where  $C_p$  is the specific heat capacity at constant pressure. The temperature is denoted by  $T$  while  $\underline{k}$  and  $\underline{k}_t$  refer to the thermal conductivity and the turbulent thermal conductivity respectively.

After the simplified versions of the governing equations were established, the numerical solver was selected.

### 3.5 Solver settings

In order to ensure that the governing equations were correctly modelled and the solver had a fast rate of convergence, certain setting and couplings were selected. The various solver settings as well as a brief description of each follow in greater detail.

Since the placement of the server racks are of importance to the study, the heat transfer was investigated at equilibrium operating conditions. Steady-state conditions were therefore imposed since the start-up and shut-down of these rooms were not investigated. Steady-state operating conditions have been a common assumption in previous studies [23, 28, 30].

For the simulations, the pressure-based solver was chosen. Although the pressure- and density-based solvers could arguably yield the same results, the pressure-based solver was specifically introduced to solve incompressible as well as slight compressible flows. The density-based solver on the other hand, was designed to simulate high-speed compressible flows [25].

Pressure-velocity coupling was achieved using the COUPLED algorithm in Ansys Fluent. The COUPLED algorithm will, in most cases, provide superior results compared with the segregated approach. The segregated approach solves the momentum and pressure correction equations separately and generally takes longer to reach a converged state [25].

The body-force-weighted spatial discretisation technique was used for the pressure. This is the recommended option when buoyancy or mixed convection is present [25].

Finally, the momentum, turbulent kinetic energy, turbulent dissipation and energy equations were solved using the second-order upwind technique. The second-order upwind technique provides greater accuracy than its first-order counterpart.

In order to speed up convergence, the pseudo-transient option was used. The pseudo-transient method speeds up convergence especially when used in conjunction with the COUPLED solver. The pseudo-transient method is a form of an implicit under-relaxation technique. The under-relaxation is achieved by calculating and using a pseudo-time step size. It is highly recommended for problems such as in this study to use the COUPLED solver as well as a pseudo-transient under-relaxation technique [25].

### **3.6 Boundary conditions and initial values**

It is noted in [24] that: “All CFD problems are defined in terms of initial and boundary conditions.” It therefore becomes necessary to assign boundary and operating conditions to the geometry. Boundary conditions in Ansys Fluent typically include walls, inlets, outlets, symmetry and cyclic boundary conditions [24]. Boundary conditions are assigned to certain edges or faces in CFD to replicate the real-world operating conditions of those surfaces. For instance, if a fluid is in contact with a wall, then the edge of the fluid would be given the “wall-type” boundary condition in Ansys Fluent. The operating conditions at the fluid-wall interface could then be set to incorporate the thickness of the wall as well as the outdoor conditions. By setting these specifications, the CFD program can (as an example) accurately calculate the heat loss or gain through the walls of the room by means of conduction, convection and radiation.

In order to determine the necessary boundary conditions, certain assumptions were made. Following is a short description of some of the boundary conditions as well as some of the assumptions relating to them.

The server racks, inlets and outlets were modelled as line sources. This means that the server racks extended into the page [21, 22]. The same is true for the inlet and outlets of the data centre. This was done because running the optimisation algorithm in three dimensions would require a much greater amount of computational resources. The two-dimensional cases are therefore seen as a “slice” of an actual three-dimensional simulation.

The walls, floor and ceiling of the room were kept at 293.15 K (20 °C). The assumption was that these faces would be treated as isothermal and insulated faces similar to [28], and would therefore not experience a change in temperature. The study focused on the spacing of the server racks and the temperatures inside the data centre. The heat transfer through the walls, floor and ceiling was therefore deemed to play a negligible role in determining the optimal configuration of the server racks.

The inlet temperature and velocity, at the leading edge of the inlet duct, were kept at a constant 288.15 K (15 °C) and 1 m/s respectively. These values coincided with previous literature [4] and seemed a reasonable range. As previously stated in Section 3.3, the additional section of inlet duct would ensure that the inlet velocity profile was somewhat parabolic in nature by the time the cool air entered the data centre.

The server panels were all kept at a constant temperature of 313.15 K (40 °C). The assumption was therefore made that the server racks themselves would utilise internal cooling and heat exchangers to keep from overheating. The server panels heat up due to the heat transfer from within the server rack. Typically, electronic equipment functions in a safe operating range of 10-60 °C [23]. By consulting with various server rack distributors, it was determined that the server panels should ideally not exceed 40 °C.

Gravity was assumed to work in the negative (downward)  $y$ -direction at a constant  $9.81 \text{ m/s}^2$ . The gravitational acceleration would ensure that buoyancy forces were accounted for in the simulations. The Boussinesq approximation was used to account for buoyancy forces. This assumption states that density changes are negligible except in the direction of gravity. Because numerous papers state that buoyancy effects play an important role when modelling indoor environments, a calculation was done to ensure that buoyancy effects should be included. To start off this calculation, the left face of the first (left) server rack in Figure 3-4 was chosen and the Reynolds and Grashof numbers were calculated. The dimensionless Reynolds number was calculated using Equation 3.5 at a film temperature of 300.65 K. The film temperature is the average temperature

between the hot surface (the server rack) and the ambient cool air. The Reynolds number in this case was determined to be approximately 126 202.

The Grashof number is the dimensionless ratio of buoyancy force to the viscous force acting on the fluid. Similar to the Reynolds number, the Grashof number is used to determine the flow regime when natural convection is present. In order to calculate the Grashof number, Equation 3.26 below was used [1]:

$$Gr = \frac{\bar{g}\beta(T_s - T_\infty)L_c^3}{\nu^2} \quad 3.26$$

where  $\bar{g}$  is the gravitational acceleration and  $\beta$  is the thermal expansion coefficient.  $T_s$  and  $T_\infty$  refer to the surface and ambient temperatures respectively. Once again,  $L_c$  refers to the characteristic length of the geometry and  $\nu$  is the kinematic viscosity of the fluid. The thermal expansion coefficient is calculated, in turn, using Equation 3.27 below:

$$\beta = -\frac{1}{\rho} \left( \frac{\partial \rho}{\partial T} \right)_p \quad 3.27$$

or simply the inverse of the temperature (K) when the fluid is assumed to behave as an ideal gas. The Grashof number was calculated using Equation 3.26 above and was found to be approximately  $2.68 \times 10^{10}$ . Coincidentally, the Grashof number was larger than  $1 \times 10^9$  indicating that the flow regime was still turbulent in nature [1]. With the Reynolds and Grashof numbers now known, the ratios between them were calculated as  $Gr/Re^2$ , which gave a value of 1.69. It could therefore safely be assumed that the effects of both forced and natural convection would be important since this ratio was close to unity [1, 31].

All other air properties were taken at 290.65 K (17.5 °C). After a few simulations were run, it was quickly determined (by means of an iterative approach) that the average air temperature inside the room was approximately 290.65 K between simulations.

### 3.7 Optimisation

According to [20], any problem in which certain parameters need to satisfy constraints may be formulated as an optimisation problem. The goal of optimisation is not only to find a set of feasible solutions to the problem at hand, but to find the optimum (or best) solution with regard to certain

parameters. Typically, optimisation is done to find the solution which would minimise effort or maximise profit.

The optimisation method used in the study was the response surface optimisation technique. In this technique, initial simulations were done in order to establish a response surface. The response surface was then refined until the difference between the actual and predicted results was within an acceptable range. Finally, an optimisation algorithm was applied to the response surface itself in order to obtain optimum solutions. Figure 3-8 below shows the typical steps involved in response surface optimisation.

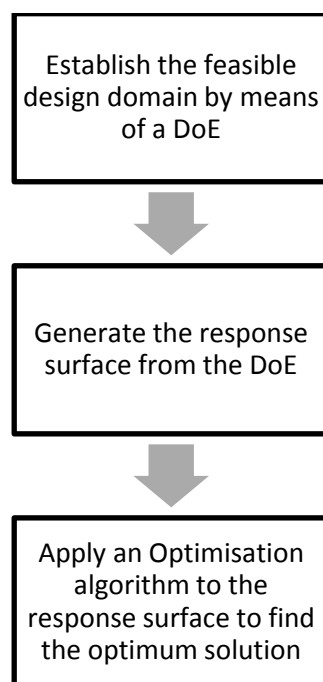


**Figure 3-8: Response surface optimisation outline**

With the dimensions of the room and server racks known, the first step (in Figure 3-8) was to determine the feasible points of the response surface. These points form the outer boundaries of the design space and any solution that falls outside this domain is deemed to be infeasible in nature. In order to create these points, Ansys DesingXplorer uses the design of experiments (DoE) feature. In the DoE phase, the goal is to find the global limits of the feasible design domain.

In order to determine the optimal configuration of data racks in the data centre, certain dimensions were assigned to be design parameters (or design variables) in Ansys. The design parameters have a

degree of freedom associated with them and are not seen as fixed dimensions. In order to illustrate this concept further, consider an enlarged view of the geometry shown in Figure 3-9 below.

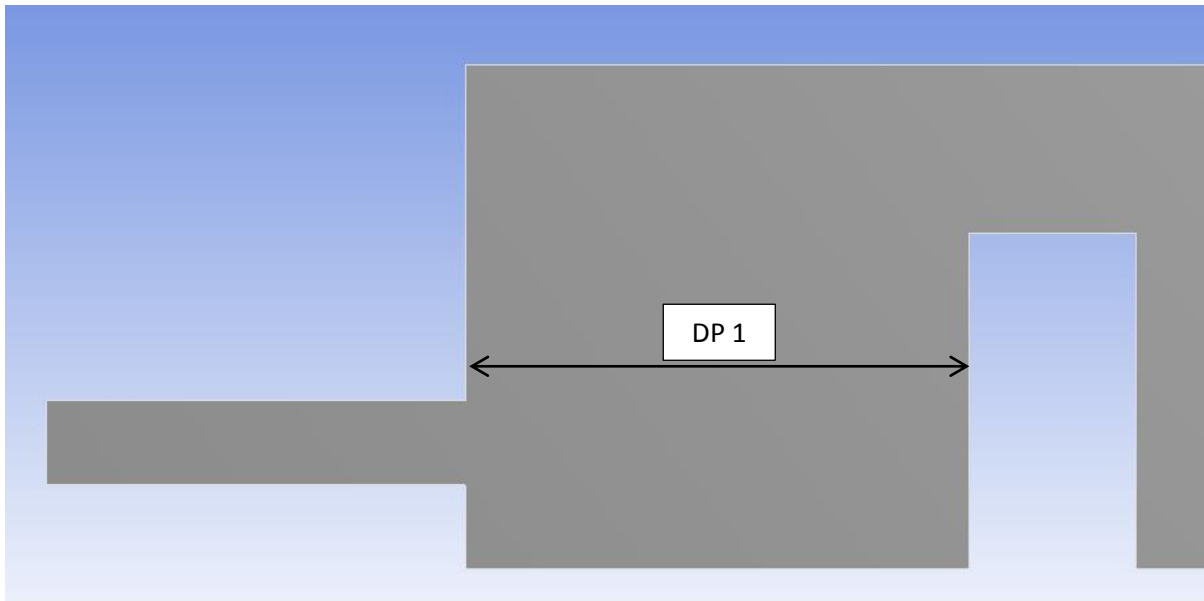


**Figure 3-9: Example of a dimension assigned to be a design parameter**

Note that in Figure 3-9, Design Parameter 1 (DP 1) is used to indicate that the dimension between the wall and the modelled server rack can change freely and is not a fixed dimension. By following this approach, the distances between server racks, the inlet height and the outlet height were set to design parameters. In Section 5.3, the height of the server racks formed additional design parameters.

With the design parameters established, the next step was to determine the DoE. One of the most common methods in generating the DoE, is to use the central composite design (CCD) method. The CCD method is an approach also known as the Box-Wilson design [25]. In this case, a custom face-centred CCD method was used. This CCD method assumes that a design parameter can have a minimum value of -1 and a maximum value of 1 while the average between the maximum and minimum values is set to 0. The face-centred CCD method is therefore a non-dimensional approach. A typical geometric representation of the face-centred CCD method is given in Figure 3-10 [25].

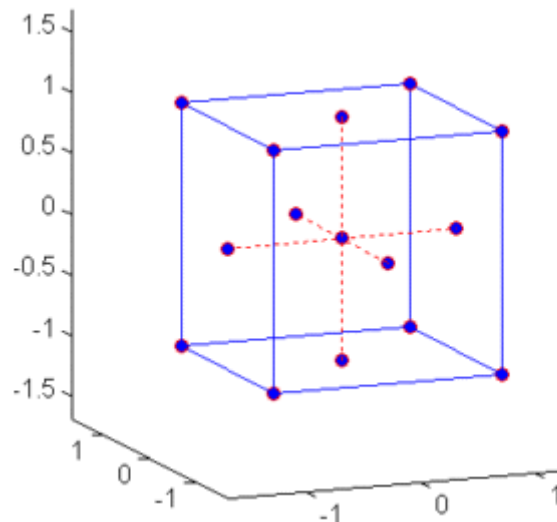


**Figure 3-10: Graphical representation of the face-centred CCD method [25]**

Note that in Figure 3-10, the design domain is fully enclosed between 1 and -1 on all three axes. The non-dimensional values obtained from the CCD method were then replaced by the dimensional values in order to obtain the maximum and minimum values for all the design parameters. Once these dimensional values were placed in the DoE matrix, the simulations were run in order to generate the sampling set.

The next step in Figure 3-8 was to generate the response surface itself. A response surface is an approximation built from the DoE, which ensures that an output can be evaluated anywhere in the design domain without having to run additional simulations [25]. From the sampling set generated by the DoE, the response surface was created using a combination of refinement points and verification points. The refinement points are design points added to the sampling set and are used (in conjunction with the initial sampling set) to generate the response surface. The verification points are design points evaluated independently from the response surface to check its accuracy.

The method in which the refinement points were added to the sampling set was by means of the Kriging method. The Kriging model fits the response surface exactly through all the design points (the DoE and the refinement points) and it therefore becomes necessary to check its accuracy using verification points. In order to explain the principle of the response surface, verification points and refinement points in greater detail, consider Figure 3-11 and Figure 3-12. Figure 3-11 below shows a response surface created using the Kriging method. Note that the response surface spans the entire length of the plausible design domain because, in this case, the server distance could only have values between 0.2 m and 5.8 m. At the same time, a constraint was placed on the outlet height

limiting it to values between 0.5 m and 2 m. The generated response surface is therefore an approximation of the sought-after output with regard to different variable inputs.

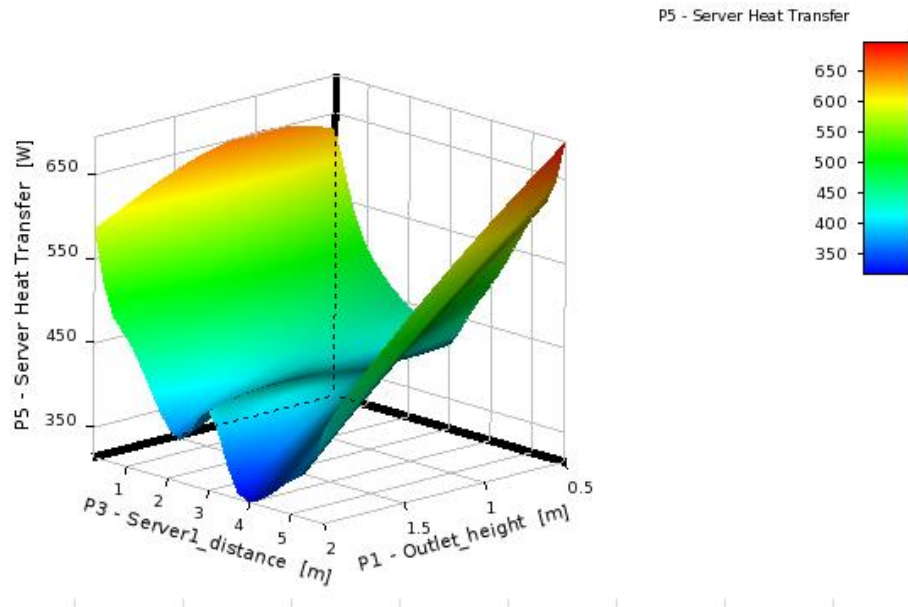


**Figure 3-11: Example of a response surface**

Once the response surface was generated, the next step was to ensure that the response surface was in fact accurate enough to predict simulations. In order to check the accuracy of the response surface, verification points were added and compared with the response surface. Figure 3-12 below is a graph comparing the server heat transfer as predicted by the response surface (squares) and the actual values computed from the verification points (circles).



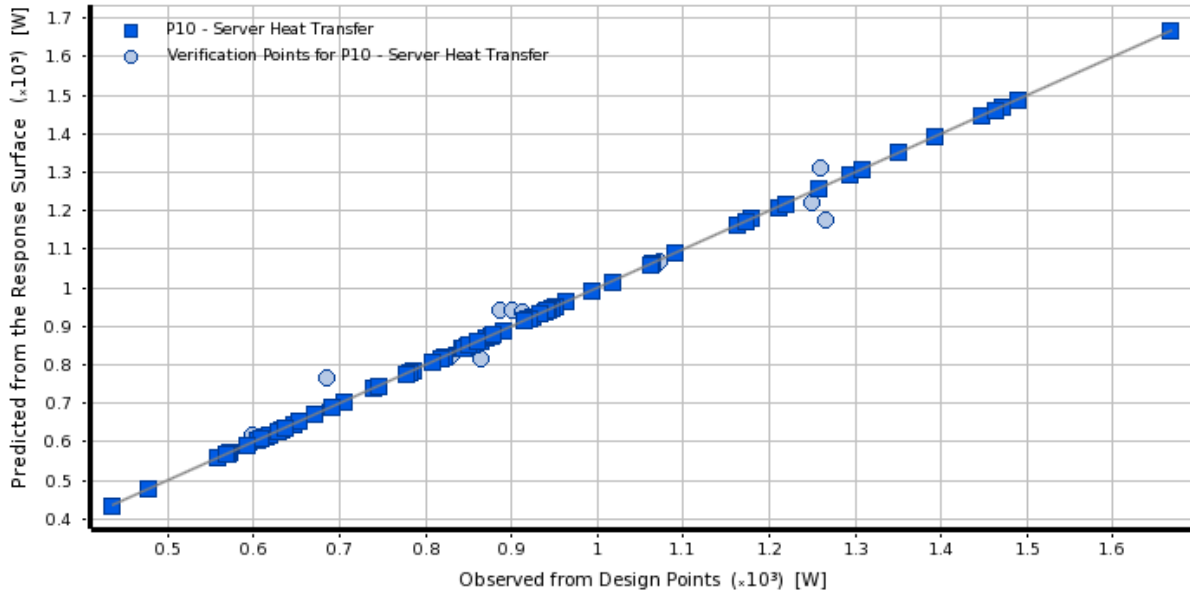


**Figure 3-12: Comparison between the response surface and verification points**

For the main part, the response surface was deemed accurate enough if the relative root mean square (RMS) error was less than 5%. This was deemed sufficient because the majority of the response surface would not be used. The area showing the highest amount of heat transfer (the objective function in this case) was refined even further before an optimisation algorithm was applied. Figure 3-13 below shows the additional verification points added to the response surface in the region of interest before additional refinement of this region commenced.

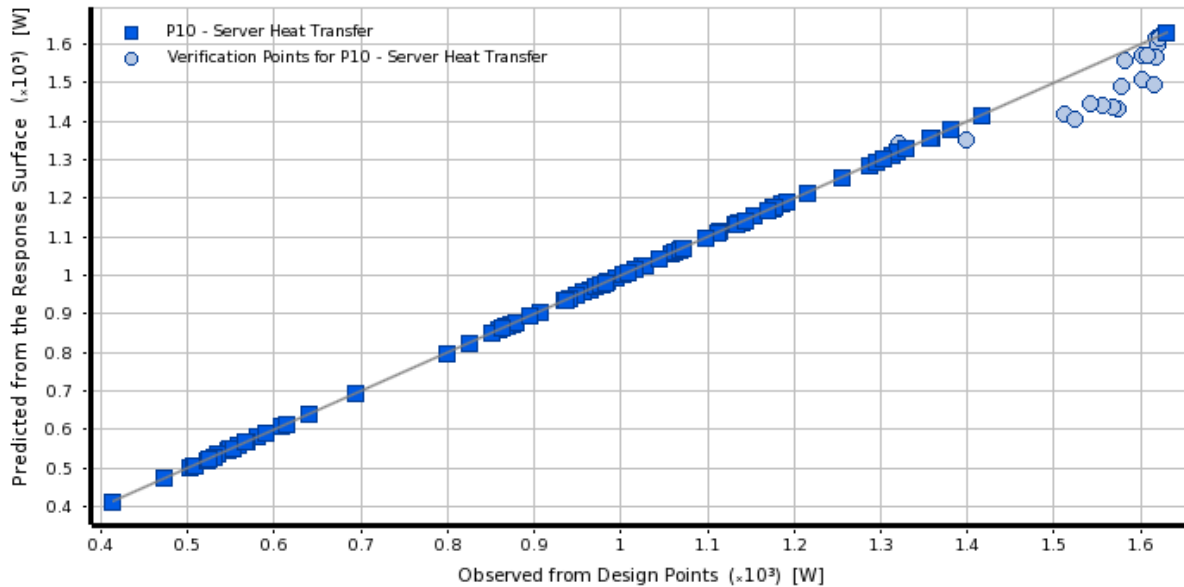


**Figure 3-13: Additional verification points added to the region of interest**

Note the additional verification points added to the region of highest heat transfer in Figure 3-13 above. After these verification points were added, they were also added as refinement points, thereby drastically increasing the accuracy of the response surface itself in this region.

Finally, once the response surface was deemed accurate enough, an optimisation algorithm was applied to find the optimum solution. Initially, a non-iterative approach known as screening was used to find the preliminary optimum points. Screening is also known as the shifted Hammersley sampling method and involves a quasi-random number generator to generate a sampling set. After the screening process was completed, a multi-objective generic algorithm (MOGA) optimisation was performed to refine the search. The MOGA approach uses a Pareto ranking method to determine optimal solutions.

The mixed-integer non-linear sequential quadratic programming (MISQP) method was also tested and it was found to converge much faster than the screening/MOGA method. The MISQP method solves mixed-integer non-linear programming (MINLP) problems by means of a modified sequential quadratic programming method. The MISQP method works by first approximating linear constraints and then constructing a quadratic approximation of the Lagrangian function. Optimal solutions are found when the Karush-Kuhn-Tucker (KKT) optimality conditions are satisfied [25].

In order to explain the KKT optimality conditions, consider the standard design optimisation problem as given in Equations 2.1-2.3. For the sake of convenience, the shortened form of these equations is provided below [20]:

Vector of design variables:  $\mathbf{x} = (x_1, x_2, \dots, x_n)$

Objective function:  $f(\mathbf{x}) = f(x_1, x_2, \dots, x_n)$  3.28

Equality constraints:  $h_i(\mathbf{x}) = 0; \quad i = 1 \text{ to } p$  3.29

Inequality constraints:  $g_i(\mathbf{x}) \leq 0; \quad i = 1 \text{ to } m$  3.30

The Lagrange multiplier theorem states that an optimisation problem subject to equality constraints of the form given in Equation 3.29 may be rewritten as a Lagrange function of the form

$$\underline{L}(\mathbf{x}, \mathbf{a}) = f(\mathbf{x}) + \mathbf{a}^T \mathbf{h}(\mathbf{x}) \tag{3.31}$$

where  $\underline{L}$  denotes a Lagrange function and  $\mathbf{a}$  is a Lagrange multiplier used for the equality constraints. Note that the transpose of the Lagrange multiplier is used in Equation 3.31 above. From Equation 3.31, necessary conditions arise, which must be satisfied in order for a design point to be considered a candidate minimum point. These conditions are given in [20] and are as follows:

$$\frac{\partial \underline{L}(\mathbf{x}^*, \mathbf{a}^*)}{\partial x_i} = 0 \quad i = 1 \text{ to } n \tag{3.32}$$

and

$$\frac{\partial \underline{L}(\mathbf{x}^*, \mathbf{a}^*)}{\partial a_j} = 0 \quad j = 1 \text{ to } p \tag{3.33}$$

where  $\mathbf{x}^*$  is a regular point that is a local minimum to the problem and  $\mathbf{a}^*$  is a set of unique Lagrange multipliers. The  $n$  number of design variables  $\mathbf{x}$  and the  $p$  number of Lagrange multipliers  $\mathbf{a}$  are unknowns that must be solved. Equations 3.32 and 3.33 are used to solve the unknowns and therefore the candidate minimum points can be found.

By following a similar approach, inequality constraints can also be solved using the method of slack variables and the Lagrange multiplier theorem. The inequality constraints (Equation 3.30) are transformed into equality constraints by adding a slack variable. Since the inequality constraints have either a zero or a negative value, the slack variable must be positive. An inequality constraint of the form in Equation 3.30 is the same as the equality constraint

$$g_i(\mathbf{x}) + s_i = 0 \quad 3.34$$

The introduced slack variable is denoted by  $s_i$  in Equation 3.34 above and as previously mentioned must be positive in nature. In order to eliminate the need for the additional constraint  $s_i \geq 0$ , the slack variable is squared and therefore must be positive or zero. This transforms Equation 3.34 into Equation 3.35 below:

$$g_i(\mathbf{x}) + s_i^2 = 0 \quad 3.35$$

By introducing Equation 3.35 into the Lagrange multiplier theorem, the necessary conditions for optimality can be determined. The new form of the Lagrange function including both equality and inequality constraints is given in Equation 3.36 below:

$$\underline{L}(\mathbf{x}, \mathbf{a}, \mathbf{b}, \mathbf{s}) = f(\mathbf{x}) + \mathbf{a}^T \mathbf{h}(\mathbf{x}) + \mathbf{b}^T (\mathbf{g}(\mathbf{x}) + \mathbf{s}^2) \quad 3.36$$

where  $\mathbf{b}$  is the Lagrange multiplier used for the inequality constraints. Similar to the necessary conditions (Equations 3.32 and 3.33) for equality constraints, the following necessary conditions arise for the inequality constrained problem. These necessary conditions are also known as the KKT conditions previously mentioned [20].

$$\frac{\partial f}{\partial x_k} + \sum_{i=1}^p a_i^* \frac{\partial h_i}{\partial x_k} + \sum_{j=1}^m b_j^* \frac{\partial g_j}{\partial x_k} = 0 \quad k = 1 \text{ to } n \quad 3.37$$

and

$$\frac{\partial \underline{L}}{\partial a_i} = 0 \quad i = 1 \text{ to } p \quad 3.38$$

and

$$\frac{\partial \underline{L}}{\partial b_j} = 0 \quad j = 1 \text{ to } m \quad 3.39$$

In addition to the necessary conditions of Equations 3.37-3.39, the following must also be true in order to satisfy the KKT conditions. First of all, the inequalities must be feasible, therefore

$$s_j^2 \geq 0 \quad j = 1 \text{ to } m \quad 3.40$$

Additionally, the switching conditions state that

$$\frac{\partial \underline{L}}{\partial s_j} = 0 \quad j = 1 \text{ to } m \quad 3.41$$

And finally, the Lagrange multipliers for the inequality constraints must be larger or equal to zero or

$$b_j^* \geq 0 \quad j = 1 \text{ to } m$$

3.42

The gradients of the active constraints must also be linearly independent in order for the Lagrange multipliers to be unique. With the KKT necessary conditions now established, the method in which the MISQP method searches for candidate points becomes clear.

The MISQP method is the suggested approach in DesignXplorer for problems involving only one objective function. Furthermore, this model has a fast rate of convergence since gradient information as well as line search methods are used in iterations [25]. The KKT convergence criterion was kept at the default value of 1E-6. Different starting locations were also tested to ensure that the starting point did not influence the optimal solution.

### 3.8 Conclusion

Following the outline set in Figure 3-1, the numerical solver was created. The various governing equations and boundary conditions were selected based on theory and past work. The numerical solver proved very stable and converged without problems. The convergence criteria for the  $x$ -velocity-,  $y$ -velocity,  $k$ -,  $\varepsilon$ - and energy equations were set to 1E-6. The convergence criterion for the continuity equation was set to 1E-5.

The optimisation part of the solver also proved to perform well. The optimum solutions were quite easily obtained after refinement of the region of interest. Typically, the optimisation required that the area of interest be refined (by means of adding verification and refinement points) three times in order to obtain an optimal solution.

With the numerical solver and optimisation algorithms now complete, the next step was to validate the solver in order to ensure that realistic solutions would be obtained.

## 4 Validation of numerical solver

### 4.1 Introduction

In this section, the numerical solver used to compute the temperature distribution in the data centre will be validated.

In order to fully validate the solver, the validation will have to prove that the two major contributing phenomena (that of buoyancy and forced convection) are modelled correctly. The first part of the validation would be to ensure that the solver accurately simulates the effects of buoyancy, or natural convection. If air is heated in a sealed room, for example, the warmer air will stratify (rise towards the ceiling), while the cooler air will collect near the floor of the room. This phenomenon occurs because the warmer air has less density associated with it. This warmer air is therefore characterised as being more buoyant than the cold air. Because the heat generated by the server racks is dissipated to the ambient air, it is important to simulate the effects of buoyancy-driven flows correctly.

The second part of the validation is to accurately model the effects of forced convection. Forced convection occurs when an external fan or blower is used to move a fluid. Mixed convection occurs if natural convection works in conjunction with forced convection. This has a significant influence in cases involving heat generation as well as fluid movement. Because an air-conditioning system will be modelled in the simulations, and natural convection will inevitably be present, the solver will have to accurately model the effects of mixed convection.

### 4.2 Experimental data

The experimental work of Blay *et al.* [33] was chosen to validate the numerical solver. This article includes experimental data and will therefore be compared with the results obtained from the numerical solver.

In his work, Blay constructed a small-scale experimental room with an inlet and outlet. The goal of the experiment was to determine whether CFD solvers could potentially yield accurate estimations of the fluid flow and temperature distribution in such a room. The problem geometry is given in Figure 4-1 below.

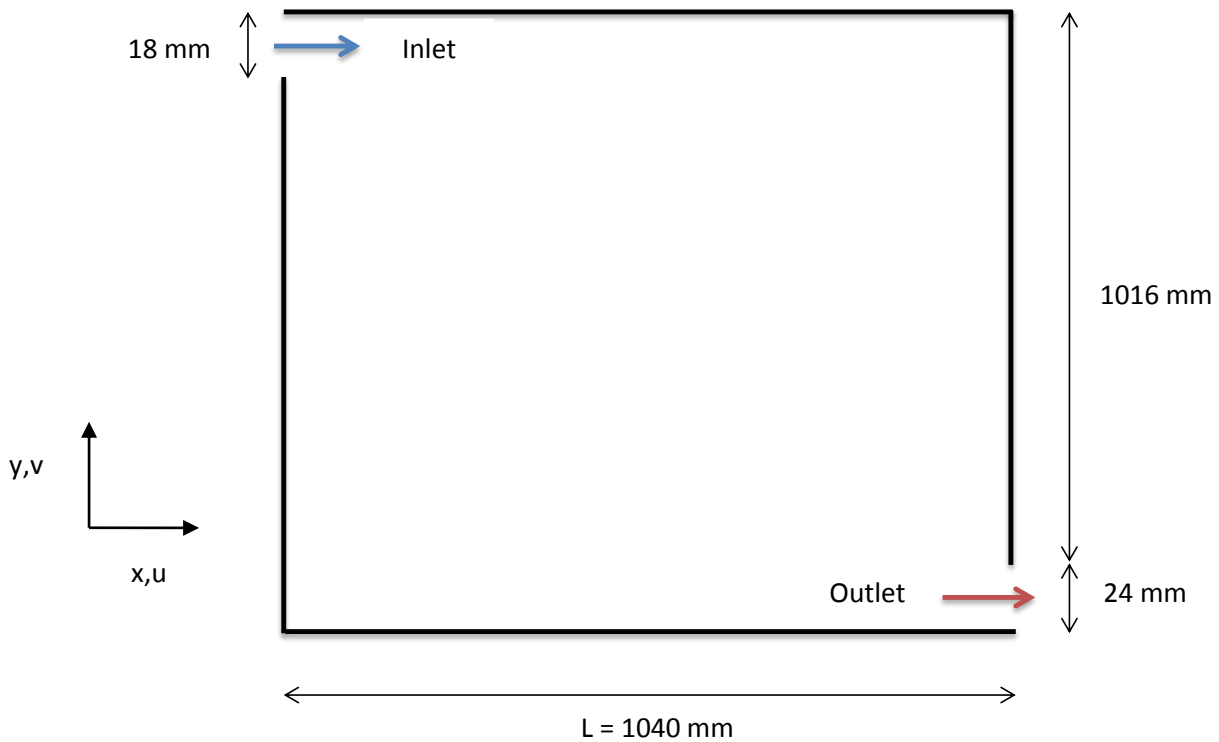


**Figure 4-1: Dimensions of the experimental room as derived from [33]**

As seen from Figure 4-1 above, the experimental room is square in nature. The room therefore has outer dimensions of  $1.04 \times 1.04 \times 0.7 \text{ m}$ . An inlet slot was constructed to be  $18 \text{ mm}$  in height and ran the entire length of the room. The inlet conditions are given in [33] as follows:

- Velocity in positive  $x$ -direction ( $u$ ) of  $0.57 \text{ m/s}$
- Velocity in  $y$ -direction ( $v$ ) of  $0 \text{ m/s}$
- Inlet air temperature ( $T$ ) of  $15 \text{ }^\circ\text{C}$  or  $288.15 \text{ K}$
- Turbulent dissipation rate ( $\epsilon$ ) of  $0 \text{ m}^2/\text{s}^3$
- Turbulent kinetic energy ( $k$ ) of  $0.00125 \text{ m}^2/\text{s}^2$

The walls and ceiling of the room were kept at a constant temperature of  $288.15 \text{ K}$  ( $15 \text{ }^\circ\text{C}$ ), while the floor was maintained at a constant temperature of  $308.65 \text{ K}$  ( $35.5 \text{ }^\circ\text{C}$ ). An outlet slot was manufactured in similar fashion to the inlet slot and also ran the length of the room. The outlet slot had a height of  $24 \text{ mm}$ .

Thermocouples and a laser Doppler device were used to capture the temperature and velocity readings throughout the experimental room. The temperature readings at different  $x$  and  $y$  locations are given in Figure 4-2 and Figure 4-3 below (as derived from [33]).

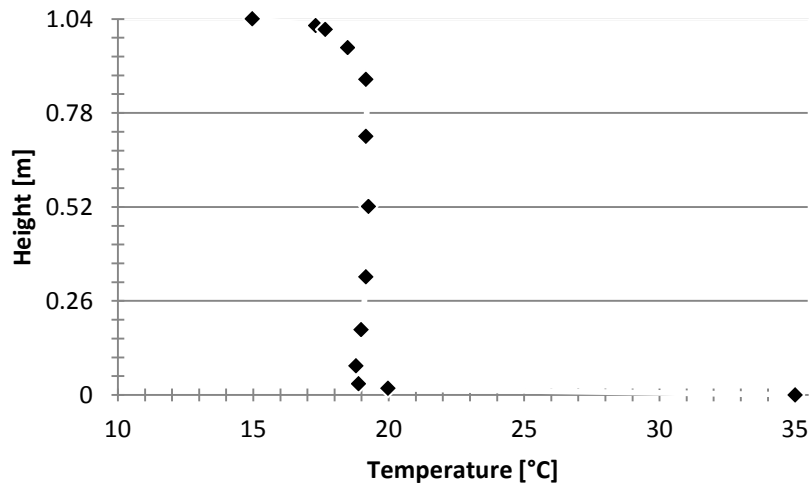


Figure 4-2: Measured temperature values as a function of height at  $x = 0.52$  m as derived from [33]

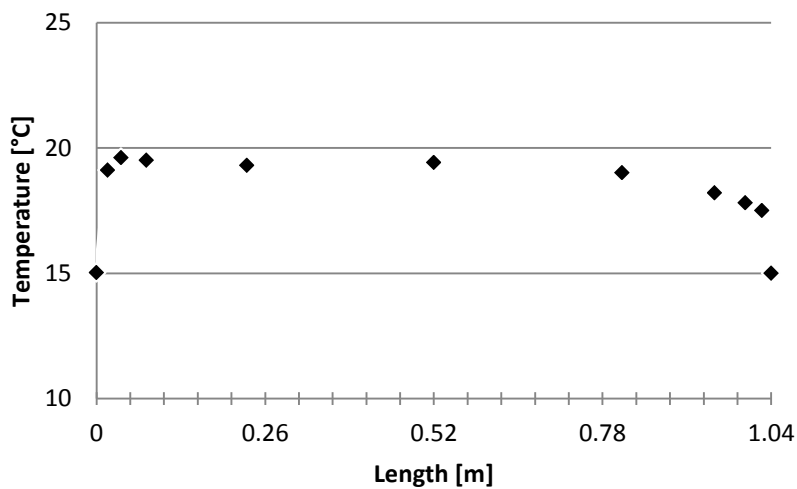


Figure 4-3: Measured temperature values as a function of length at  $y = 0.52$  m as derived from [33]

As seen in Figure 4-2 and Figure 4-3, the measured air temperature varies at different locations throughout the room. Since buoyancy forces and mixed convection are present, the temperature profiles are not expected to be linear.



The goal now was to construct a numerical solver capable of replicating these experimental results. If the results obtained from the CFD solver coincided with the experimental values, the CFD solver would then be considered validated.

### 4.3 CFD simulations

By using Ansys Fluent, the experimental case was recreated and solved using the settings described in Section 3. The results showed that the experimental and CFD results were in good agreement with each other. Below follows a short description of the necessary steps needed to create the CFD model.

The experimental room was drawn up in Ansys DesignModeler and given the same dimensions. The inlet and outlet slots were added to incorporate the various boundary conditions. It should be noted that two surfaces were created to ensure that a structured mesh would be present throughout the duration of the simulations (discussed later in this section).

Once the geometry was created, the geometry underwent the next step known as meshing. In order to accurately simulate flow at the wall regions, as well as any region which was expected to have high pressure or thermal gradients, inflation layers were added to the mesh. Inflation layers ensure that an even finer mesh is created in the desired regions, which, in turn, normally results in a more accurate prediction of flow.

Finally, additional sizing was added to the inlet and outlet regions of the geometry. In order to simulate the parabolic flow of air expected at the inlet, the inlet had to be divided into enough elements to ensure that this profile would be created accurately. If too few elements were used, then a parabolic flow might be simulated as a uniform flow or semi-circular flow. The geometry (after it has undergone meshing) is given in Figure 4-4 below.

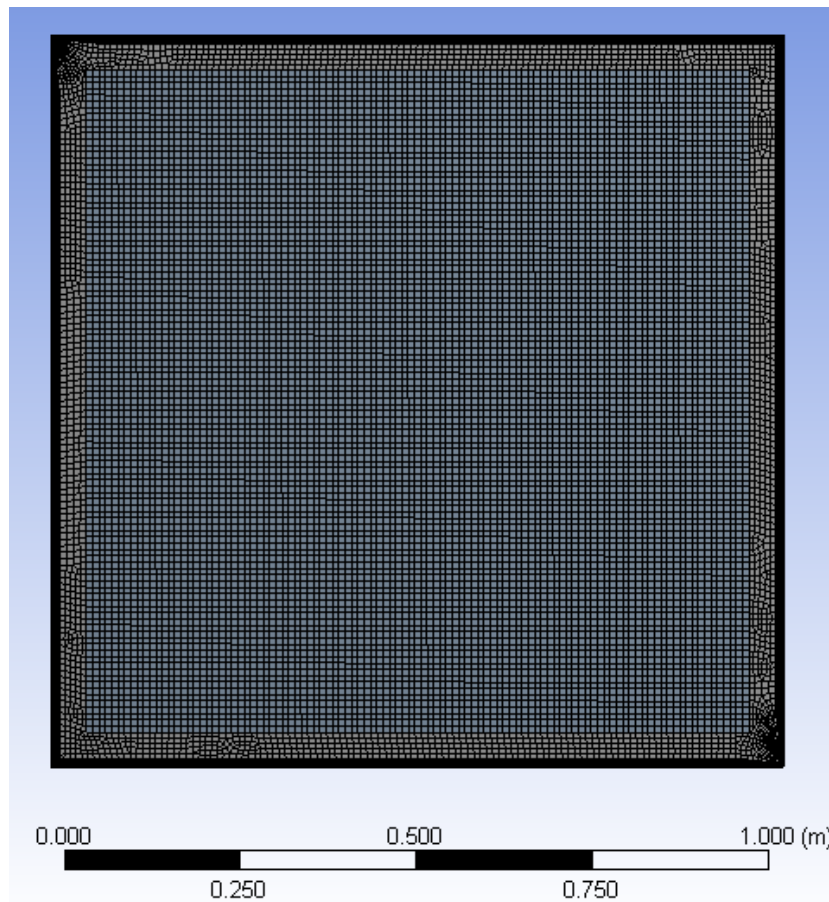


**Figure 4-4: Mesh used for validation of numerical solver**

The mesh shown in Figure 4-4 has 18 454 elements with 25 566 nodes. In order to ensure that the orthogonal quality of the mesh was satisfactory, the mesh should have an orthogonal quality of close to unity. Furthermore, the mesh should preferably have an aspect ratio of close to 1 [25]. The aspect ratio of a mesh is defined as the length of cell divided by the width of the same cell [25]. The aspect ratio therefore provides an indication of how square the cells are and subsequently how accurate the overall mesh is. A mesh with an orthogonal quality of unity means that the distance to each neighbouring cell is identical. If the distance to each neighbouring cell is not equal, then the mesh will also be skewed to some extent. If the orthogonal quality is close to zero, it means that the mesh is very skew in nature and could potentially yield inaccurate results. Franke *et al.* [27] mention that the mesh should not be overly skew.

A mesh convergence study was done to ensure that the mesh yielded accurate results, while still falling into the user's time constraints and computational resources. The three outputs chosen for the mesh convergence were that of average air temperature, the orthogonal quality of the mesh and the total heat transfer dissipated by the floor of the room.

Table 4.1 below shows the mesh convergence study similar to those in previous studies [21, 22, 34]. It is important to note that the percentage error between subsequent simulations should be checked to ensure that the mesh performs satisfactory. In the case of this convergence study, the mesh was deemed sufficient if percentage errors between simulations were less than 0.1% for both average air temperature as well as the heat transfer dissipated by the floor of the room. In addition to the aforementioned criteria, the orthogonal quality should show a difference of less than 1%.

**Table 4.1: Mesh convergence study**

	Number of Elements	Average Air Temperature [°C]	% Change	Heat Transfer [W]	% Change	Average Orthogonal Quality	% Change
<b>Case 1</b>	8357	18.6151		59.8729		0.96471	
<b>Case 2</b>	15386	18.6259	0.057984	59.99004	0.195266	0.98096	1.656541
<b>Case 3</b>	18465	18.6275	0.008589	60.03492	0.074756	0.98433	0.342365

From Table 4.1 above, it can be seen that Case 3 meets all the imposed requirements for the mesh. Once the mesh convergence was finished, the next step in validating the solver was to set the boundary conditions as well as the various operating conditions.

The operating and boundary conditions accurately simulated the conditions given by Blay *et al.* [33]. The inlet velocity, inlet temperature and wall temperatures were given the same values as measured during experimentation. Furthermore, the turbulent dissipation rate and turbulent kinetic energy were also given the same numerical values.

The same solver settings as discussed in Chapter 3 were used in the validation of the numerical solver. Finally, the properties of air at 293.15 K (20 °C) were assigned to the inner air region of the room. Buoyancy effects were accounted for by using the Boussinesq approximation.

## 4.4 Comparison

After the settings and boundary conditions were applied to the model geometry, the simulation ran and the numerical results were compared with the experimental values. Figure 4-5 and Figure 4-6 below show a comparison between the numerical results and the results obtained by Blay *et al.* [33].

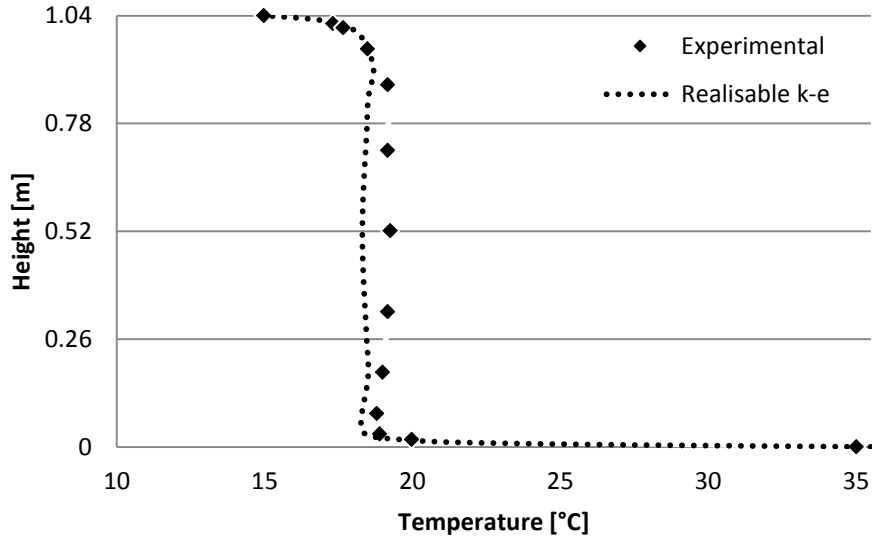


Figure 4-5: Comparison between numerical solver and experimental data [33] at  $x = L/2$

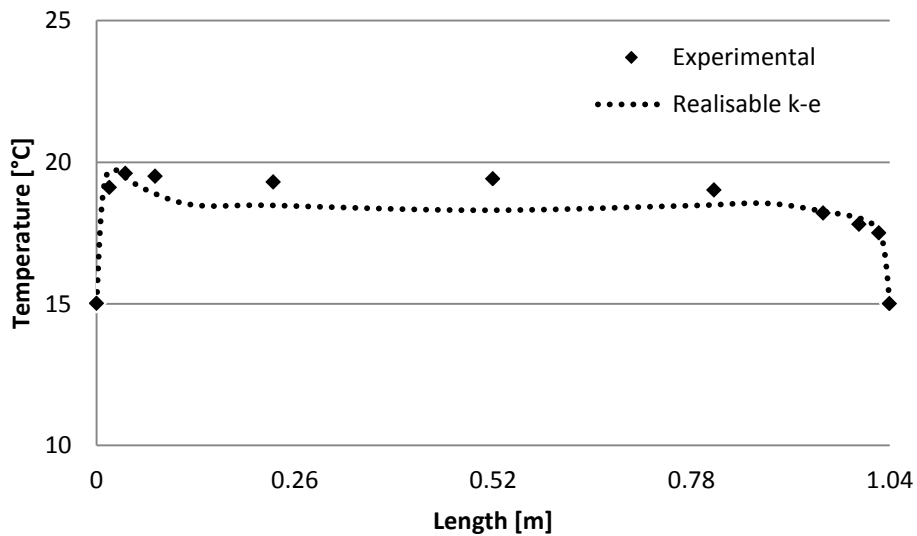


Figure 4-6: Comparison between numerical solver and experimental data [33] at  $y = L/2$

Note that in Figure 4-5, the experimental values are given by the squares. The results of the realisable  $k-\epsilon$  solver are represented by the dashed line. It can therefore be seen that the numerical solver is in good agreement with the experimental values. The highest recorded difference between the numerical and experimental values was 5.7%. The same trend can also be seen in Figure 4-6. The numerical results were once again in good agreement with the experimental data. The highest recorded error for this case was 4.9%.

Although the experimental and numerical results compared well with each other, differences are still noted. These differences range from numerical errors to physical limitations in the experimental model. It should be kept in mind that the thermocouple wires, for instance, cause an additional obstruction in the flow field when studying the experimental results. Numerical errors, in turn, range from simple round-off errors to discretisation errors. Round-off errors arise as a result of real numbers being presented as numbers with a set amount of significant digits [24]. Discretisation errors, in turn, are caused during the approximation of flow variables in the finite volume method. The approximations of these flow variables are, for example, based on the chosen mesh. In order to minimise the discretisation errors, the mesh should be extremely fine, which is not always feasible due to computational and time limits [24]. Input uncertainties can also contribute to the difference between the numerical and experimental values. The boundary conditions and fluid properties are not always known (such was the case for this study) and therefore assumptions have to be made. These assumptions could then, in turn, give rise to differences between the numerical and experimental values.

## 4.5 Conclusion

The suggested solver accurately predicted the results obtained from the experimental data. It can therefore be concluded that the numerical solver was able to predict the effects of mixed convection. Therefore, the finite volume method was chosen to solve the governing equations. In addition, the RANS method was chosen to predict the effects of turbulence. The realisable  $k-\varepsilon$  solver was chosen to solve the Reynolds stresses introduced when using the RANS turbulence model.

## 5 Results and discussions

### 5.1 Introduction

In order to determine the effect of server placement and height, it was decided to run two different main scenarios. The first scenario (Section 5.2) featured constant server rack heights. In the second scenario (Section 5.3), the effect of varying the server rack height was also investigated.

Server racks normally abide by a set of standard dimensions designated by the letter “U”. According to the Electronic Industries Alliance (EIA), one unit of “U” is 44.45 mm (1.75 inches) in height [10]. The EIA also specifies that the mounting rails in a typical server rack should be spaced to have internal dimension of 450.85 mm and 44.45 mm with regard to width and height respectively.

Furthermore, the EIA states that most modern data centres now utilizes the 42 U server racks, which means that the server racks have internal dimensions of 1.867 m in height. By studying various catalogues, it was decided to model typical IBM model 93074RX 42U server racks. From various catalogues, the model 93074RX server rack has the dimensions listed in Table 5.1 below.

**Table 5.1: IBM Model 93074RX 42 U server rack dimensions [26]**

External Height	External Width	External Depth	Static Weight Capacity
2000 [mm]	605 [mm]	1000 [mm]	1090 [kg]

Three different variations of inlet and outlet locations were investigated. The first case (Case A) had both the inlet and the outlet situated on the opposing walls of the data centre. The second case (Case B) had the inlet situated on the wall, while the outlet was located on the ceiling of the data centre. Finally, the third case (Case C) had the inlet located on the ceiling and the outlet on one of the walls. All three cases were tested on both fixed as well as varying server rack heights.

In order to find the optimum solutions, design parameters were assigned to certain dimensions as discussed in Chapter 3. The first design parameter was assigned to the inlet height. The inlet was free to move vertically for Case A and Case B and horizontally for Case C. A minimum and a maximum height were specified in order to ensure that the inlet would not touch the floor or the ceiling of the room. The minimum distance between the inlet and the floor was chosen to be 0.5 m.

The same distance was chosen between the inlet and the ceiling. As previously mentioned, the inlet itself had a height of 0.5 m. The case in which the inlet was placed on the ceiling (Case C) featured the same minimum distance between the inlet and the walls.

The outlet height was the second assigned design parameter and was treated the same as the inlet. The minimum gap of 0.5 m was specified between the outlet and the floor as well as the outlet and the ceiling. The outlet itself also had a height of 0.5 m. Case B (in which the outlet is placed on the ceiling) had the same minimum distance specified between the outlet and the walls.

Finally, the distance between the left wall and the left edge of the server rack was also set to a design parameter. If more servers were added to the room, then the gap between subsequent servers was selected as design parameters. It was decided that a small gap should exist between the server rack and the walls. The server racks were therefore not allowed to be placed within 0.2 m from any of the walls. The minimum distance between subsequent server racks was also set to 0.2 m.

After the results were obtained, the dimensions of the server distance, inlet height as well as the outlet height were non-dimensionalised. In the case of the server distances, the total distance between the left wall (not the inlet) and the server was divided by the room length of 7 m. The inlet and outlet heights were, in turn, non-dimensionalised by dividing the result by the total height of the room (3 m).

All simulations were done on an Acer Aspire 5750 notebook with 2 gigabytes of DDR3 memory and an Intel Core i3-2310M processor.

## **5.2 Fixed server height methodology and results**

As mentioned in Section 5.1, a number of IBM model 93074RX 42U racks were modelled and placed in the data centre. The response surface optimisation technique was then applied to ensure that an optimum solution was obtained. For the case of fixed server heights, approximately 924 simulations were run in order to obtain the optimum solutions.

### 5.2.1 Case A - Inlet and outlet located on walls

The scenario of fixed server heights was divided into three sub-cases as previously mentioned. The first of these cases had the inlet as well as the outlet on opposing walls of the data centre. By using the design parameter methodology as discussed in Chapter 3, the number of design parameters needed was established. The number of design parameters for the various sub-cases is given in Table 5.2 below. For the case of two server rows, for example, the design parameters were the inlet height, outlet height, the distance to the first server and the distance to the second server. This meant that for the case of two server racks with fixed heights, four design parameters were needed. The number of design parameters needed (Table 5.2) remained the same for Cases B and C respectively since only the inlet and outlet locations were changed.

**Table 5.2: Number of design parameters used for fixed server height simulations**

Number of Server Racks	1	2	3	4
Number of Design Parameters	3	4	5	6

After the simulations were run and the optimisation algorithm applied, the optimum placements of the server racks and the inlet and outlet locations were established. Table 5.3 below shows the non-dimensional optimal placements of the server racks as well as the inlet and outlet heights for the Case A fixed server height scenario. By non-dimensionalising the distances in this fashion, it can be seen from Table 5.3 that Server Rack 2 (for the case of two server racks) should be placed at 0.829 or 82.9% of the total room length from the left wall of the data centre. In the case of a 7 m room, this would mean that the server should be placed at a distance of  $7 \times 0.829 = 5.8$  m from the left wall. The same principle applies to the inlet height as well as the outlet height.



**Table 5.3: Fixed server height Case A optimal placements**

	Number of Server Racks			
	1	2	3	4
<b>Inlet Height [-]</b>	0.167	0.167	0.167	0.167
<b>Outlet Height [-]</b>	0.533	0.167	0.167	0.167
<b>Server Rack 1 Distance [-]</b>	0.029	0.029	0.029	0.029
<b>Server Rack 2 Distance [-]</b>	-	0.829	0.314	0.343
<b>Server Rack 3 Distance [-]</b>	-	-	0.829	0.586
<b>Server Rack 4 Distance [-]</b>	-	-	-	0.829
<b>Server Rack Size</b>	42 U	42 U	42 U	42 U
<b>Optimal Heat Transfer [W]</b>	830.044	1649.456	1890.826	2041.036

The following figures show a graphical representation of Table 5.3 above. The temperature distribution throughout the data centre is plotted in Ansys Fluent and is given for each case below. The velocity distribution plots for all the tested cases can be found in Annexure A.

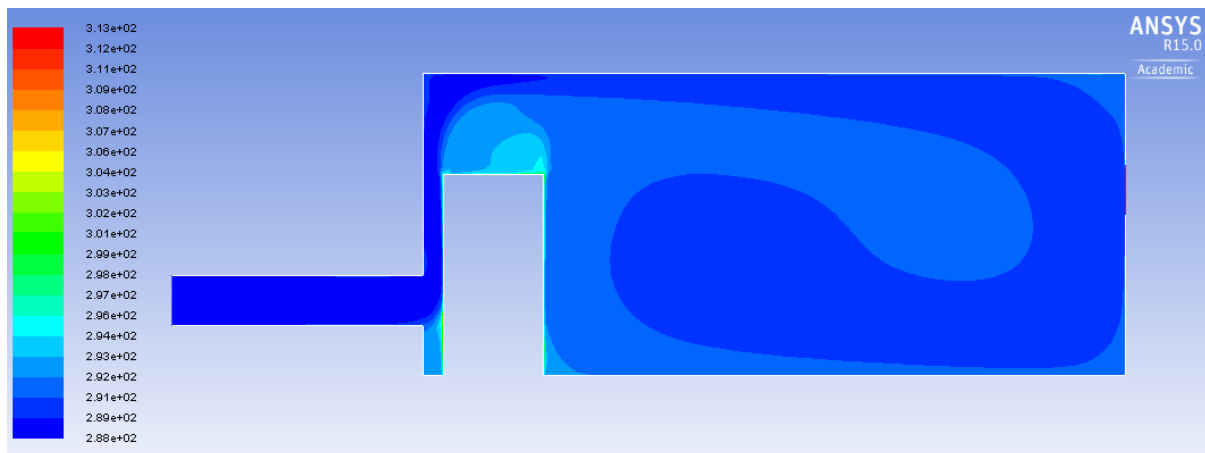


**Figure 5-1: Fixed server height Case A 1 server rack temperature distribution**

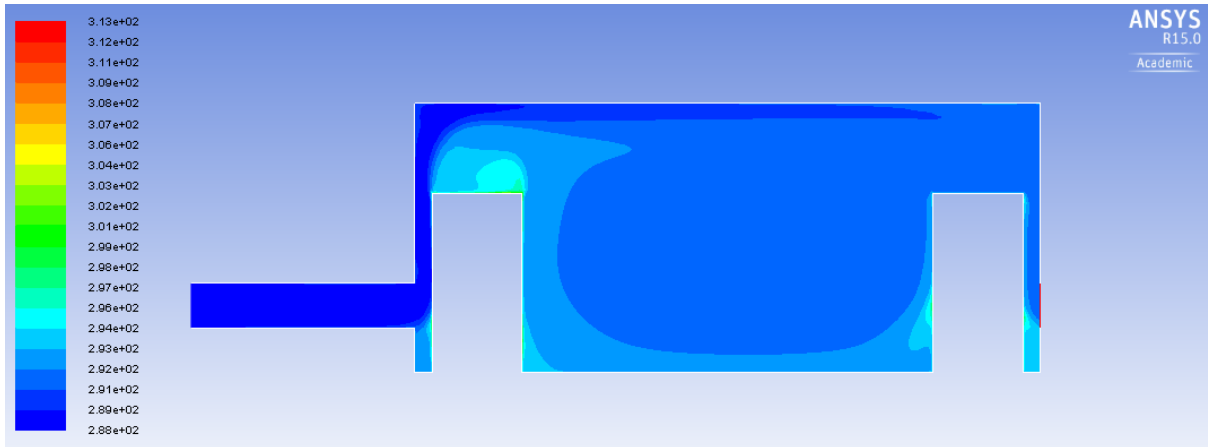


Figure 5-2: Fixed server height Case A 2 server racks temperature distribution

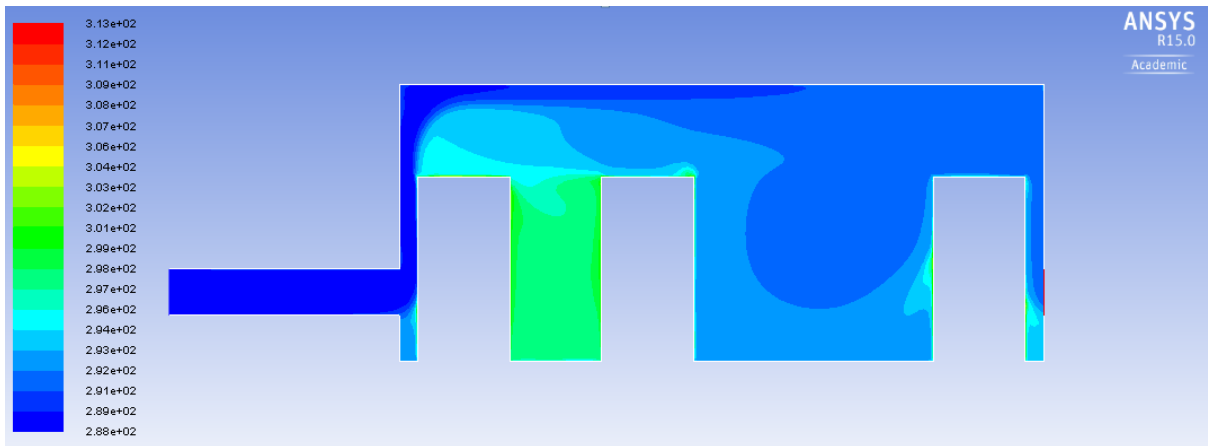


Figure 5-3: Fixed server height Case A 3 server racks temperature distribution

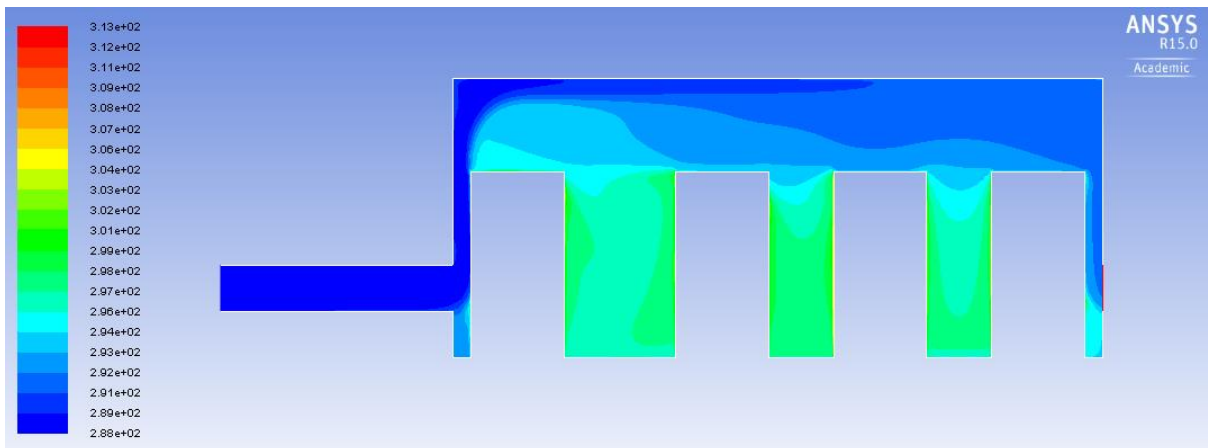


Figure 5-4: Fixed server height Case A 4 server racks temperature distribution

It is interesting to note from the above figures that optimum location of the first row of server racks was (in all four cases) as close to the inlet as possible. This means that the first server should be placed 0.2 metres or  $0.2/7 = 0.029$  (in non-dimensional format) from the left wall of the data centre. In turn, the last row of servers was placed as close to the outlet as possible. The result was that a cool air recirculation zone was formed in the centre of the room. This zone becomes smaller when more servers are added. It is evident from the case with four servers, that recirculation was limited due to the lack of available space.

The optimal inlet location for all four cases was as close to the floor as possible (at 0.5 metres or 0.167 for the non-dimensional case). The case of two, three and four server racks showed that the outlet should also be placed as close to the floor as possible. It is interesting to note that for the case of one server rack row, the outlet should be placed higher on the wall. This is due to the nature of the cool air recirculating zone.

The heat transfer (W) from the server panels to the ambient surroundings also showed interesting results. As expected, the heat transfer almost doubled when increasing the number of server racks from one (830.044 W) to two (1 649.456 W). However, the same was not true when a third (1 890.826 W) and fourth (2 041.036 W) row of servers were introduced, indicating that the air was already too warm to significantly cool the servers.

### **5.2.2 Case B - Inlet located on wall and outlet on ceiling**

As previously mentioned, the number of design parameters needed was the same as for the previous case (Table 5.2). The only difference between Case A and Case B was the location of the outlets. Table 5.4 below shows the non-dimensional optimal placements of the server racks as well as the inlet height and outlet distance. It should be noted that the outlet distance was non-dimensionalised by dividing it by the total room length of 7 meters. The outlet distance was therefore given from the left wall (not the inlet) of the server room.

**Table 5.4: Fixed server height Case B optimal placements**

	Number of Server Racks			
	1	2	3	4
<b>Inlet Height [-]</b>	0.167	0.167	0.167	0.167
<b>Outlet Distance [-]</b>	0.857	0.857	0.857	0.857
<b>Server Rack 1 Distance [-]</b>	0.029	0.029	0.029	0.029
<b>Server Rack 2 Distance [-]</b>	-	0.786	0.3	0.314
<b>Server Rack 3 Distance [-]</b>	-	-	0.829	0.557
<b>Server Rack 4 Distance [-]</b>	-	-	-	0.814
<b>Server Rack Size</b>	42 U	42 U	42 U	42 U
<b>Optimal Heat Transfer [W]</b>	779.967	1262.92	1491.822	1669.277

The following figures show a graphical illustration of Table 5.4 above. Note that in the following figures, the outlet was located on the ceiling of the data centre. Note that the velocity vector plots are given in Annexure A of the report.

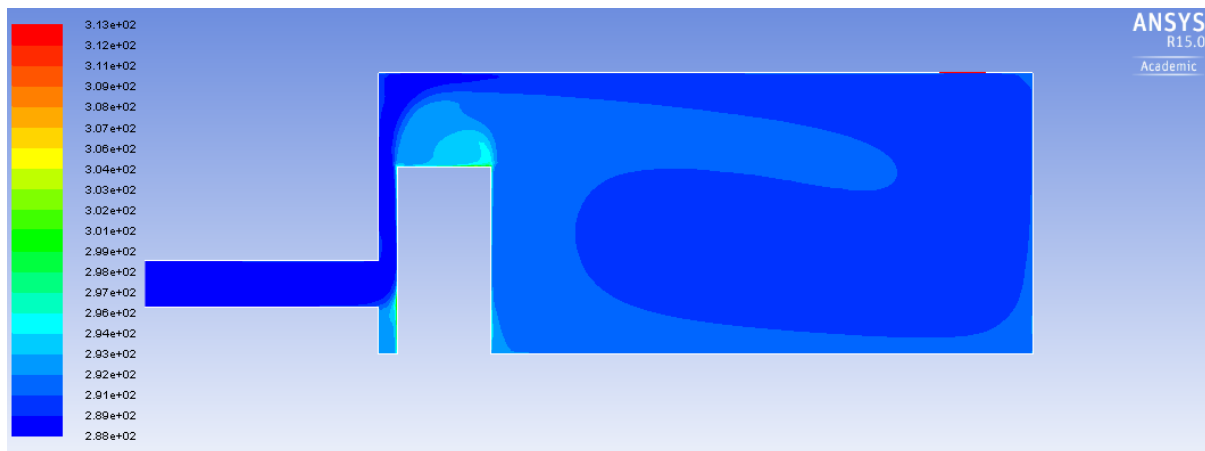


**Figure 5-5: Fixed server height Case B 1 server rack temperature distribution**

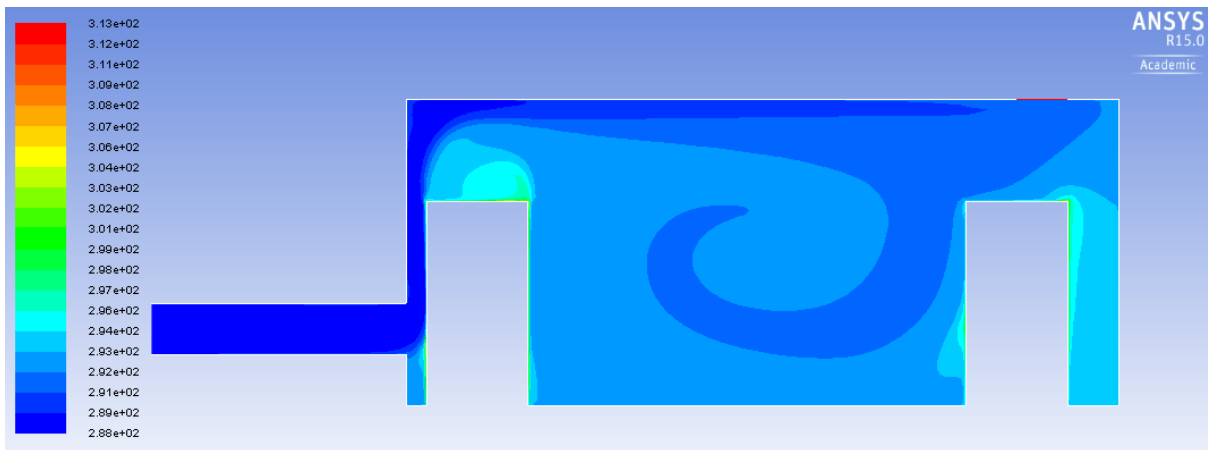


Figure 5-6: Fixed server height Case B 2 server racks temperature distribution

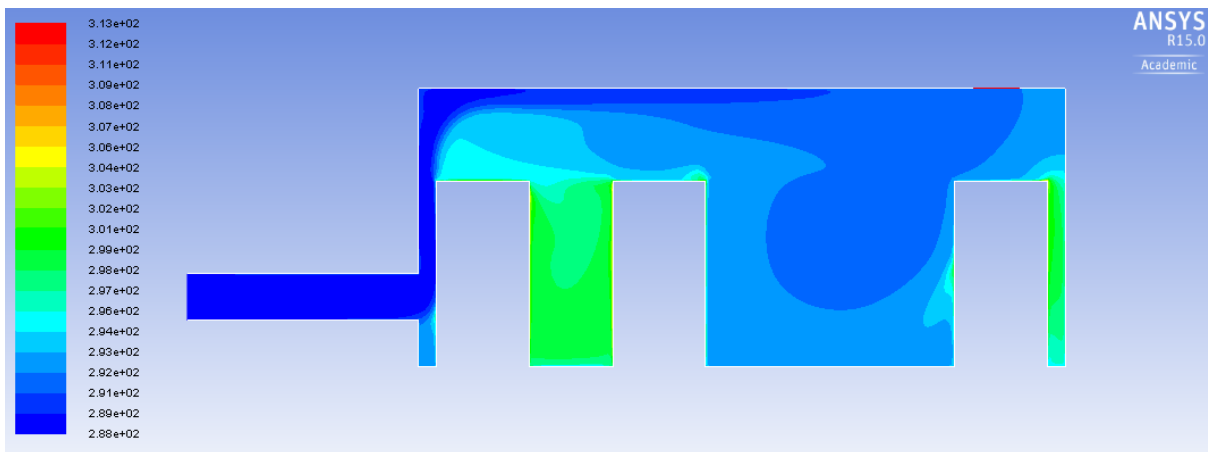


Figure 5-7: Fixed server height Case B 3 server racks temperature distribution

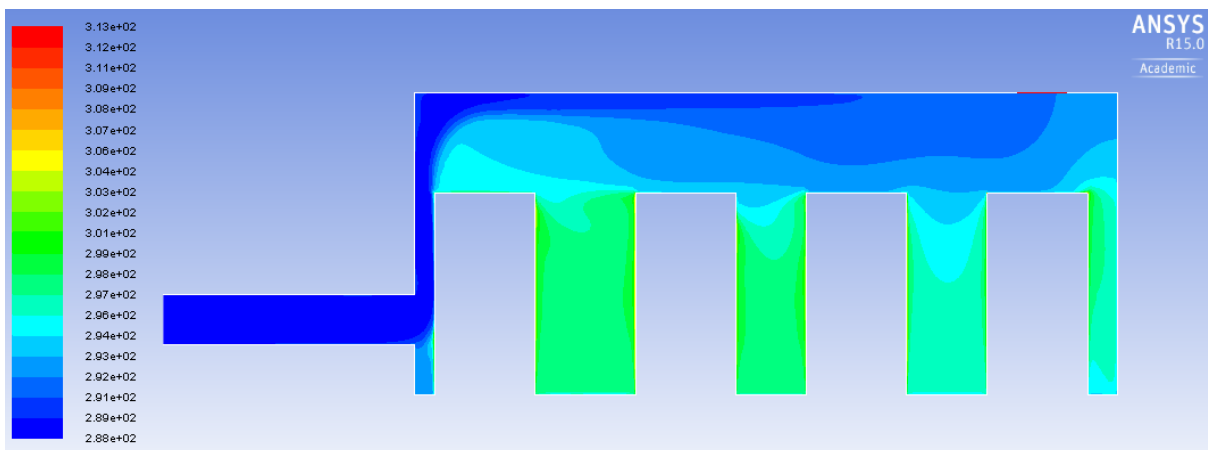


Figure 5-8: Fixed server height Case B 4 server racks temperature distribution

By studying the figures above, it quickly becomes clear that the first row of server racks should be placed (much the same as in Case A) as close to the inlet as possible. Once again, the inlet location proved to be most efficient as close to the floor of the room as possible (0.5 m). The outlet, on the other hand, should be placed as far away from the inlet as possible (6 m from the left wall).

Although slight variations were observed with regard to the placement of the last server rack row, a clear pattern was noted. For the case of two, three and four server rack rows, the last server should be placed close to the right wall and beneath the outlet.

The heat transfer from the server rack panels to the ambient surroundings showed similar results to those of Case A. When the number of server racks was increased from one (779.967 W) to two (1 262.92 W), a large difference in heat transfer was noted as expected. However, when a third (1 491.822 W) and a fourth (1 669.227 W) row were introduced, the heat transfer showed little increase. This showed that the air quickly heated up due to the server racks and for the case of three and four server rack rows, was already too warm to significantly cool the servers.

### 5.2.3 Case C – Inlet located on ceiling and outlet on wall

As with the previous two cases, the number of design parameters needed remained the same and is given in Table 5.2. The outlet location was now moved back to the right wall (as in Case A). The inlet location was now moved to the ceiling of the room much like the outlet in Case B. The optimal non-dimensional placements of the inlet, outlet and server racks are given in Table 5.5 below.

**Table 5.5: Fixed server height Case C optimal placements**

	Number of Server Racks			
	1	2	3	4
<b>Inlet Distance [-]</b>	0.071	0.1	0.071	0.086
<b>Outlet Height [-]</b>	0.167	0.167	0.167	0.167
<b>Server Rack 1 Distance [-]</b>	0.829	0.029	0.067	0.029
<b>Server Rack 2 Distance [-]</b>	-	0.829	0.483	0.243
<b>Server Rack 3 Distance [-]</b>	-	-	0.829	0.543
<b>Server Rack 4 Distance [-]</b>	-	-	-	0.829
<b>Server Rack Size</b>	42 U	42 U	42 U	42 U
<b>Optimal Heat Transfer [W]</b>	853.793	1249.211	1510.578	1629.948

Graphical representations of Table 5.5 are given in the following figures. Note that the inlet was located on the ceiling of the data centre in the following figures.

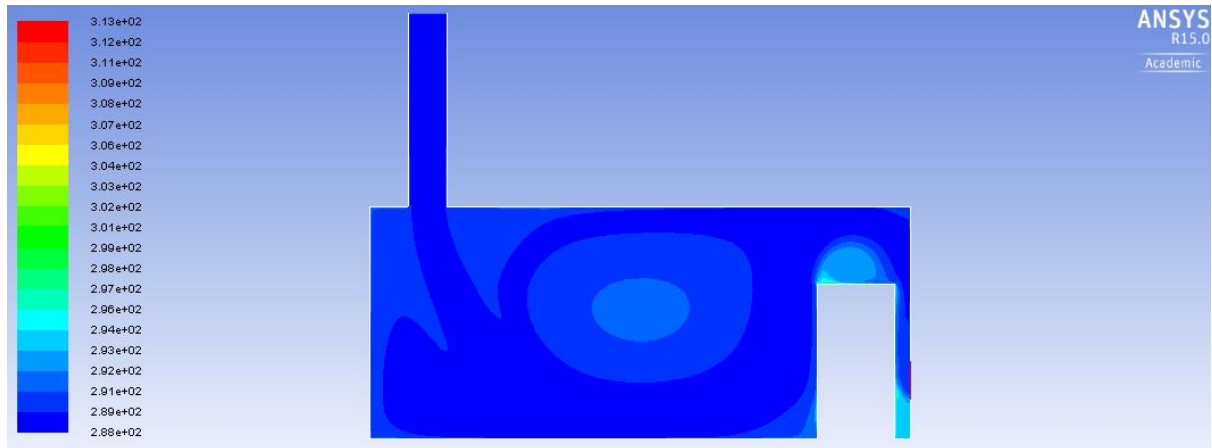


Figure 5-9: Fixed server height Case C 1 server rack temperature distribution

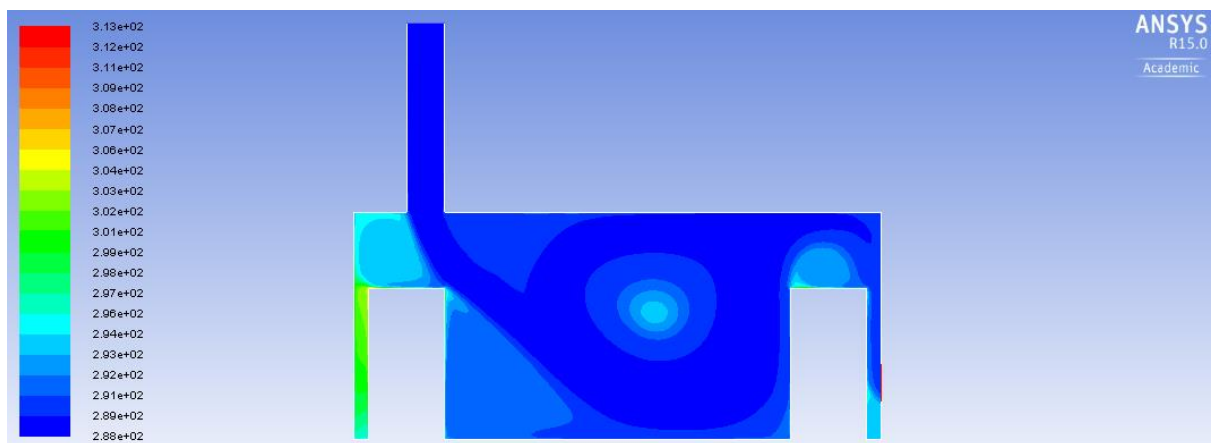
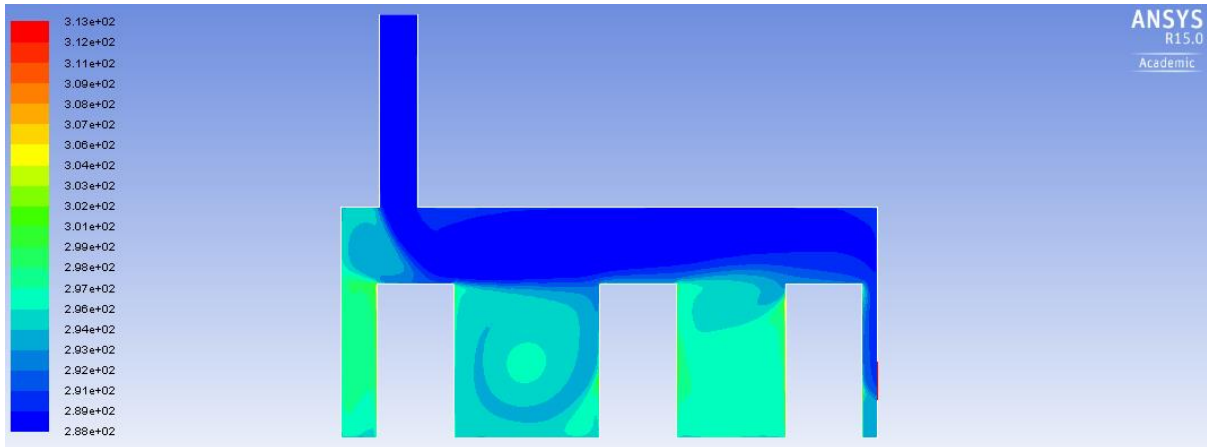
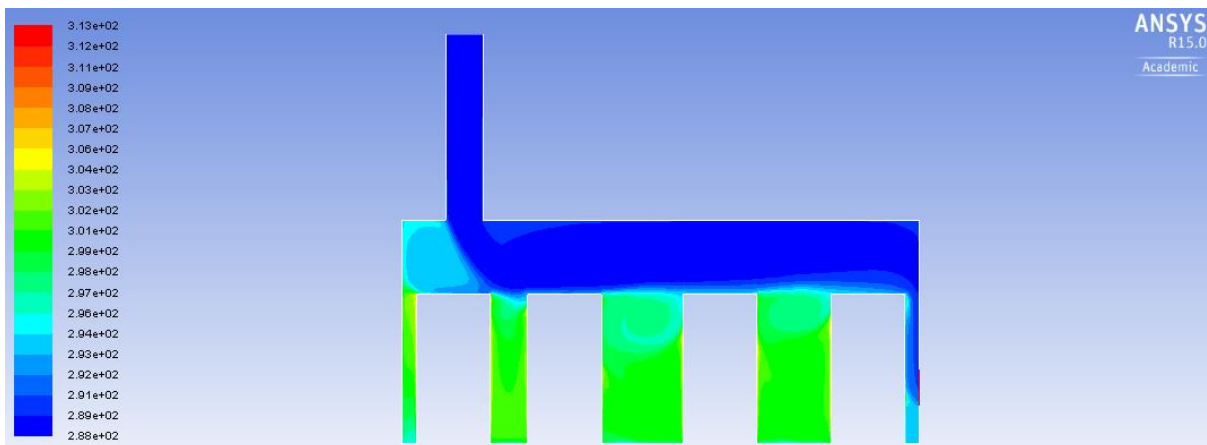


Figure 5-10: Fixed server height Case C 2 server racks temperature distribution



**Figure 5-11: Fixed server height Case C 3 server racks temperature distribution**



**Figure 5-12: Fixed server height Case C 4 server racks temperature distribution**

From the figures above, it can be seen that the inlet distance should be close to the left wall of the data centre. Although the inlet was free to move across the ceiling, results showed that in order to significantly cool the servers, the inlet should be placed far away from the outlet. This was the case for any number of server rows, although slight variations were observed.

The optimal outlet location proved to be as close to the floor of the data centre as possible (0.5 m). The optimal outlet height remained constant for any number of servers tested.

For the case of one server rack row, the server should be placed close to the outlet of the data centre. This proved different from Case A and Case B, in which the server should be placed close to the inlet. The inlet location (for the case of one server rack only) tended to already ensure a large cool air recirculation zone. The cool air entered the room from the ceiling and, after coming into



contact with the floor of the room, immediately formed a recirculation zone. In the case of one server rack, this recirculation zone would be smaller if the server was placed close to the inlet and not the outlet.

The same trend regarding heat transfer from the server panels to the ambient surroundings was witnessed by studying the results. For the case of one server rack only, the heat transfer was calculated to be 853.793 W. If another row of server racks was introduced, the heat transfer increased to 1 249.211 W. Subsequently, the addition of a third and a fourth row showed heat transfers of 1 510.578 W and 1 629.948 W respectively. It can therefore be seen that the difference in heat transfer between three and four servers was approximately 120 W. This is a clear indication that the recirculation of cool air was no longer efficient since the air itself had greatly increased in temperature.

#### **5.2.4 Comparison**

After all the fixed server height simulations were run, a comparison between the different cases was drawn up. When comparing the different cases, the subject of most importance is the amount of obtainable heat transfer. This would serve as an indication of how well a particular case performs with regard to other cases. Figure 5-13 below shows the different tested cases for fixed server heights. The measured heat transfer is given per number of server rack rows.

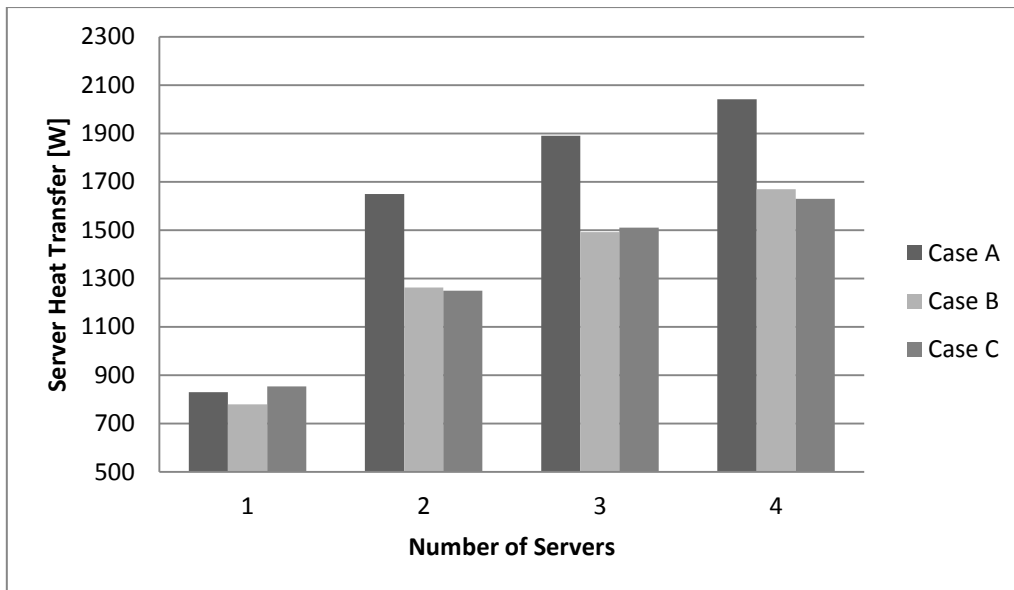


**Figure 5-13: Comparison between fixed server height cases**

From Figure 5-13 above, a few important conclusions can be made. Except for the case of one server rack row, Case A outperformed both Case B and Case C. Interestingly though is the case of one server rack row, in which Case C proved to have the highest amount of heat transfer. The heat transfer from Case A and Case C was similar, with an approximate 24 W difference. Nonetheless, Case C proved to be the better option for one server rack row. The reason for Case C having a higher heat transfer was due to the nature, size and direction of the cool air recirculation zone.

For the case of two server rack rows, Case A showed an increase of approximately 386 W with regard to Case B. Case B, in turn, showed an increase of almost 14 W with respect to Case C. It can, therefore, safely be concluded that Case A was the better option for cooling data centres with two rows of server racks.

The case of three server rows showed much the same results in that Case A once again outperformed the other two cases. The measured optimal heat transfer for Case A was 380 W higher than that of Case C. Case C, in turn, showed a heat transfer increase of 19 W over Case B. Case A, therefore, should be the set-up in data rooms with three server rack rows.

Finally, the case of four server rack rows showed similar results. Once again the calculated heat transfer between Case B and Case C was relatively close, with Case B showing an increase of 39 W. Case A, on the other hand, showed a heat transfer of 2 041.036 W which was approximately 372 W higher than that of Case B.

The server rack spacing showed somewhat of a pattern between cases. For two server rack rows, the first server was placed at the inlet and the second at the outlet. The gap between servers was therefore, as large as possible to promote the recirculation of cool air.

Another interesting observation was that Case A and Case B, when three server rack rows were used, showed a similar spacing of discrete heat sources to the previously mentioned work of Bejan *et al.* [21]. The servers were spaced in close proximity to one another at the inlet and then spread further apart at the outlet. For Case C, however, this was not the case as having the inlet on the ceiling produced entirely different cool air recirculation zones.

For the case of four server rack rows, the spacing was somewhat more random in the sense that the different placements of server racks showed little impact on the obtainable heat transfer. As previously discussed, this was due to lack of available room for the formation of cool air recirculation regions.

### **5.3 Variable server height methodology and results**

After the optimal placements for the fixed server rack height scenario was established, the racks were given another degree of freedom in that their height was also allowed to change. By setting the server rack heights as additional design parameters, the data centre was now no longer limited to only 42 U rack servers. It should be noted that in order to compare the variable server height cases with those of fixed server heights, the total area of server space was kept constant. This meant that if two servers were placed in the data centre, the sum of their respective heights should be equal to that of two 42 U racks. These cases would therefore only be done for the case of two, three and four server racks.

The same three inlet and outlet locations (Case A, Case B and Case C) were also investigated for variable server heights.

Although the height of the servers was free to change, the width of the servers was still kept constant at 1 m (as given in Table 5.1). The response surface optimisation technique was applied to ensure that an optimum solution was obtained. For the case of variable server heights, approximately 2 143 simulations were run in order to obtain the optimum solutions.

### 5.3.1 Case A - Inlet and outlet located on walls

The first tested case for variable server heights was Case A. Case A consisted of having the inlet located on the left wall of the data centre. In turn, the outlet was placed on the right wall of the data centre. Case A for the variable server height scenario therefore had the same inlet and outlet location as Case A for the fixed server height scenario. The same was true for Case B as well as Case C.

With the addition of variable server heights, the number of design parameters increased dramatically. Each server rack now had a corresponding distance as well as height associated with it. The number of design parameters for the case of variable server rack heights is given in Table 5.6 below. For the case of two server rack rows, the design parameters were the inlet and outlet distances, the server distances as well as the server heights. This meant that six design parameters were needed for the case of two servers with variable heights. The number of design parameters needed remained constant for Case B and Case C.

**Table 5.6: Number of design parameters used for variable server height simulations**

Number of Server Racks	2	3	4
Number of Design Parameters	6	8	10

The same minimum and maximum gaps for distances and heights were used for the case of fixed and variable server heights. The 42 U server rack, as previously discussed, had a height of 2 metres. The room, on the other hand, had a height of 3 metres. It was therefore decided that the server rack heights could be 2.8 metres at a maximum and 1.2 metres at a minimum. This would ensure that the minimum distance between the walls and the server racks would now apply between the ceiling of the room and the server racks.

After the simulations were run and the optimisation algorithm applied, the optimum locations of the server racks, inlets and outlets were established. Table 5.7 below shows the non-dimensional optimal placements of the server racks as well as the inlet and outlet heights for the Case A variable server height scenario. Note that the dimensions were non-dimensionalised in the same fashion as those of fixed server heights. The size (height) of each server rack is also given in Table 5.7 below.

The server rack heights were kept in the “U” notation since, by definition, they are already non-dimensional in nature and adhered to certain standards.

**Table 5.7: Variable server height Case A optimal placements**

	Number of Server Racks		
	2	3	4
Inlet Height [-]	0.167	0.167	0.167
Outlet Height [-]	0.167	0.167	0.167
Server Rack 1 Distance [-]	0.029	0.029	0.029
Server Rack 2 Distance [-]	0.829	0.586	0.396
Server Rack 3 Distance [-]	-	0.829	0.657
Server Rack 4 Distance [-]	-	-	0.829
Server Rack 1 Size	25.2 U	42 U	58.8 U
Server Rack 2 Size	58.8 U	25.2 U	25.2 U
Server Rack 3 Size	-	58.8 U	25.2 U
Server Rack 4 Size	-	-	58.8 U
Optimal Heat Transfer [W]	1908.794	2290.293	2900.017

Following is a set of figures which gives a graphical illustration of Table 5.7 above. Note that the servers were no longer the same height and that the same inlet and outlet locations were used. The following temperature distributions were created in Ansys Fluent. The corresponding velocity distributions can be found in Annexure A.

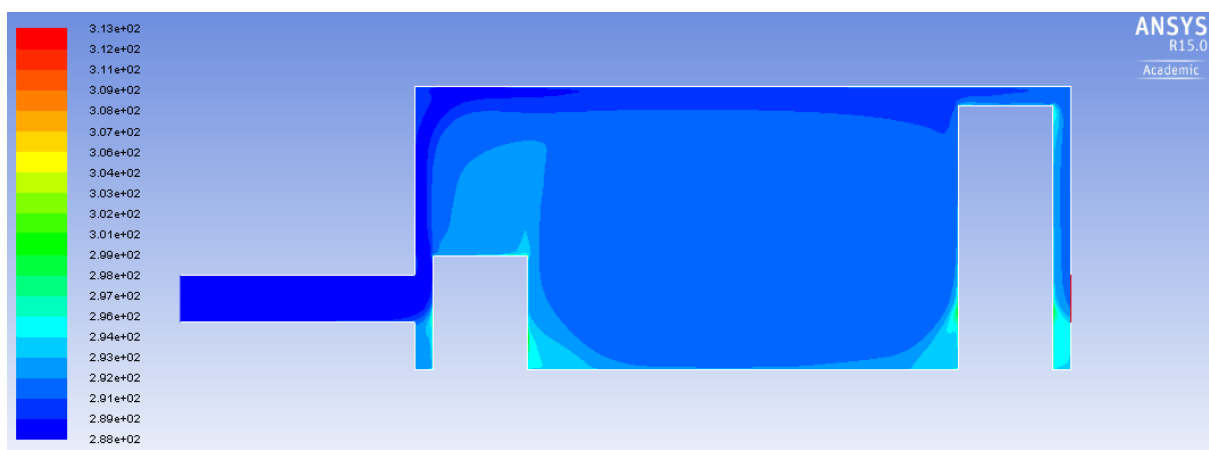


**Figure 5-14: Variable server height Case A 2 server racks temperature distribution**

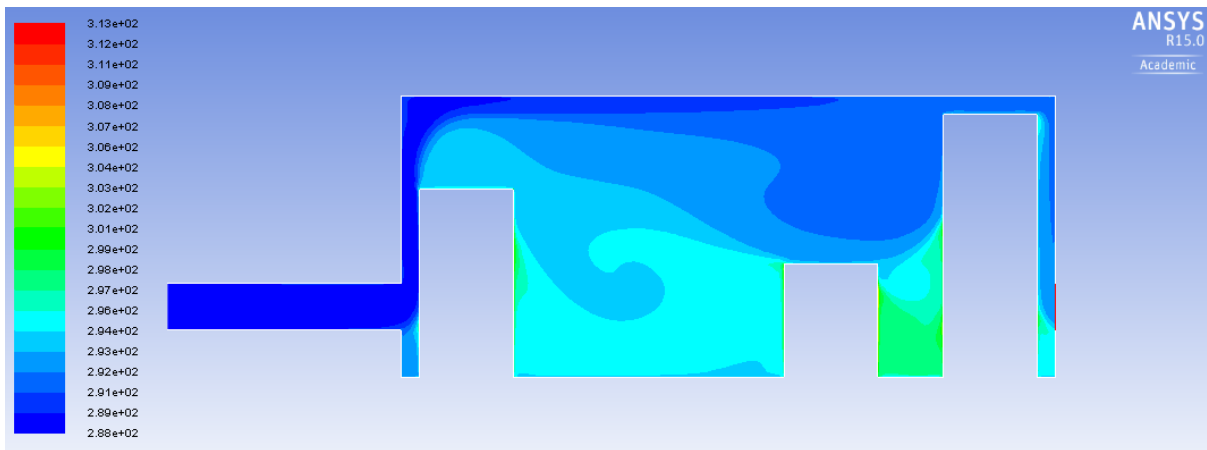


**Figure 5-15: Variable server height Case A 3 server racks temperature distribution**

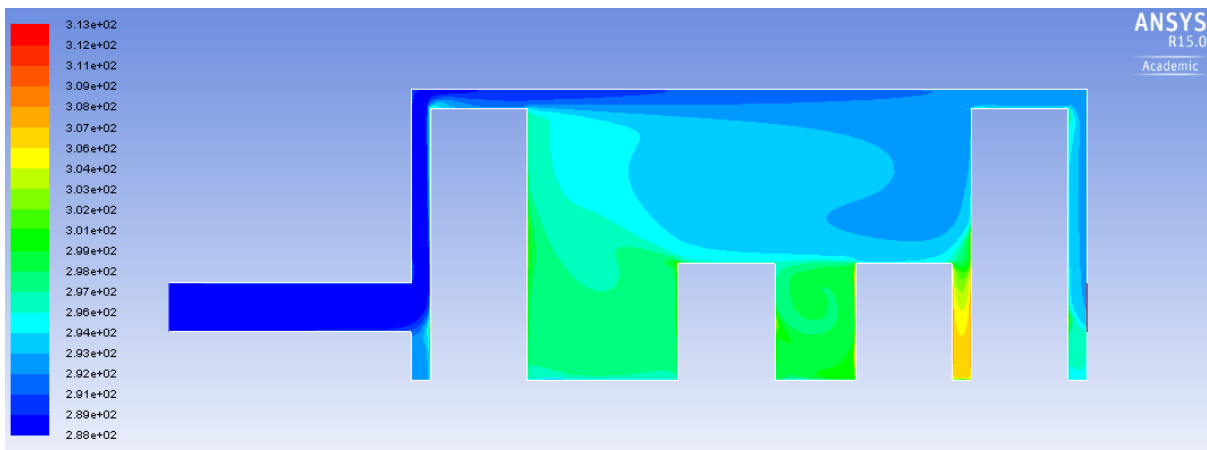


**Figure 5-16: Variable server height Case A 4 server racks temperature distribution**

Much like the fixed server height scenario, the first row of server rack rows proved to be most efficient if placed as close to the inlet as possible. This was true for the case of two, three and four server rack rows. The last server in turn, should once again be placed as close to the outlet as possible. This ensured that cool air recirculation would be present in the centre of the data room and therefore promote heat transfer.

The inlet height as well as the outlet height proved to be most efficient if placed as close to the floor as possible. This was again true regardless of the number of server racks used.

The heat transfer from the server panels to the ambient air was 1 908.794 W, 2 290.293 W and 2 900.017 W for the case of two, three and four server rack rows respectively. Therefore, it can be seen that the heat transfer showed a much more steady increase than for the fixed server height

scenario. The servers were now allowed to change in height and could, in turn, more efficiently utilise the cool air recirculation zones. Note that a comparison between all scenarios and cases is given in Section 5.4.

### 5.3.2 Case B – Inlet located on wall and outlet on ceiling

The second-to-last case tested for the variable server height scenario was Case B. Similar to Case B for the fixed server height scenario, the inlet was located on the left wall of the data centre, while the outlet was placed on the ceiling of the room.

As previously mentioned, the number of design parameters needed was the same as for the previous case (Table 5.6). The only difference between Case A and Case B was the location of the outlets. Table 5.8 below shows the non-dimensional optimal placements of the server racks as well as the inlet height and outlet distance.

**Table 5.8: Variable server height Case B optimal placements**

	Number of Server Racks		
	2	3	4
<b>Inlet Height [-]</b>	0.167	0.167	0.167
<b>Outlet Distance [-]</b>	0.857	0.857	0.857
<b>Server Rack 1 Distance [-]</b>	0.029	0.029	0.029
<b>Server Rack 2 Distance [-]</b>	0.577	0.336	0.329
<b>Server Rack 3 Distance [-]</b>	-	0.829	0.629
<b>Server Rack 4 Distance [-]</b>	-	-	0.8
<b>Server Rack 1 Size</b>	25.2 U	58.8 U	58.8 U
<b>Server Rack 2 Size</b>	58.8 U	42 U	25.2 U
<b>Server Rack 3 Size</b>	-	25.2 U	58.8 U
<b>Server Rack 4 Size</b>	-	-	25.2 U
<b>Optimal Heat Transfer [W]</b>	1632.654	1796.781	2487.198

Graphical illustrations of Table 5.8 are again given below. Note that the outlet was now moved to the ceiling of the room, while the inlet was still located on the left wall of the data centre.

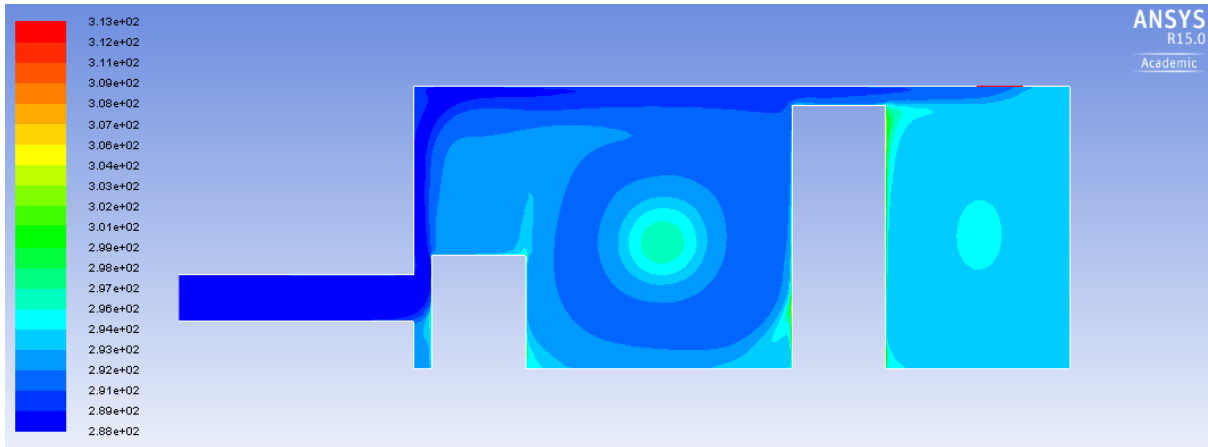


**Figure 5-17: Variable server height Case B 2 server racks temperature distribution**

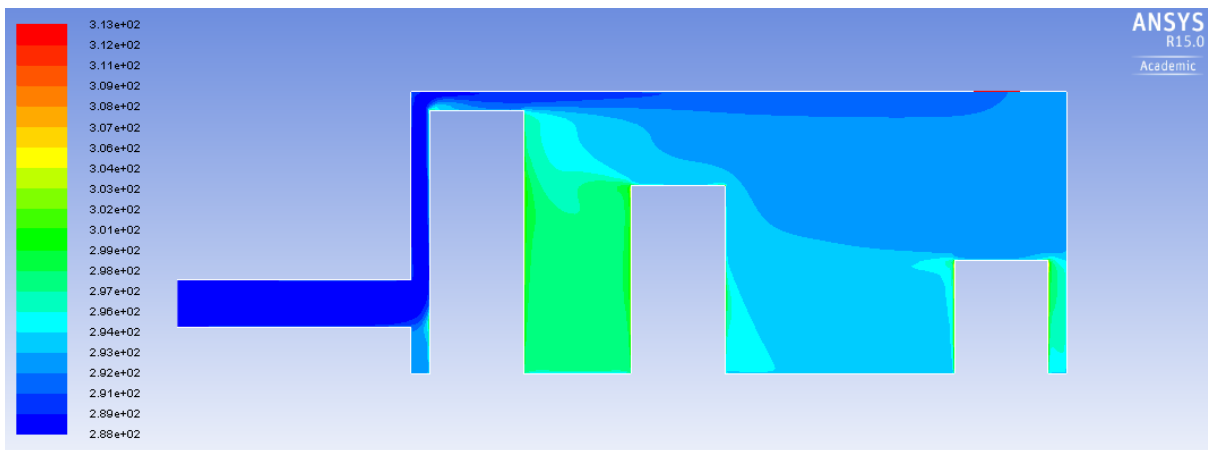


**Figure 5-18: Variable server height Case B 3 server racks temperature distribution**

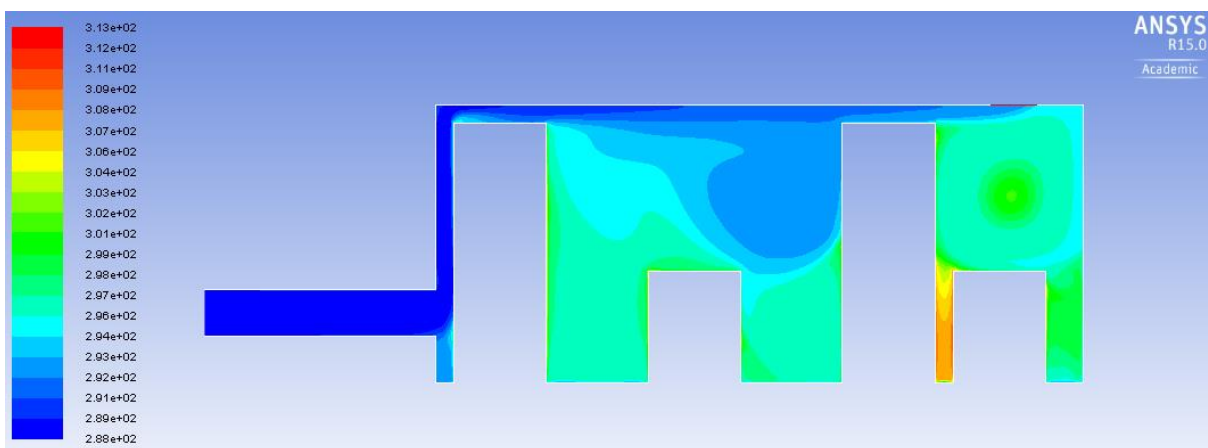


**Figure 5-19: Variable server height Case B 4 server racks temperature distribution**



From the above figures, it can be concluded that the first row of server racks should yet again be placed close to the inlet of the room. This proved to be the same regardless of the number of server racks. The last row of servers showed no clear pattern across the number of server rows, but generally should be close to the outlet of the data room. For the case of two servers, the second server proved to be most efficient if placed almost in the centre of the room. This resulted in the last server having two large cool air recirculation zones adjacent to it as seen in Figure 5-17.

Simulations proved yet again that the optimal location for the inlet was as close to the floor of the room as possible (0.5 m). The outlet, in turn, should be placed as far away from the inlet as possible (6 m) in all cases.

The heat transfer from the server panels again showed that by having a degree of freedom for server heights, the heat transfer greatly improved from the fixed server height scenario. The calculated heat transfers for two, three and four server rack rows was 1 632.654 W, 1 796.781 W and 2 487.198 W respectively.

### **5.3.3 Case C - Inlet located on ceiling and outlet on wall**

The last case tested was Case C, which featured the inlet on the ceiling of the data centre. The outlet was placed on the right wall of the data centre. Once again, the number of design parameters remained the same compared with Case A and Case B above and is given in Table 5.6. The optimal placements for the inlet, outlet and servers are given in Table 5.9 below. Also given in Table 5.9 is the size (or height) of each individual server rack.

**Table 5.9: Variable server height Case C optimal placements**

	Number of Server Racks		
	2	3	4
<b>Inlet Distance [-]</b>	0.071	0.071	0.071
<b>Outlet Height [-]</b>	0.167	0.167	0.167
<b>Server Rack 1 Distance [-]</b>	0.13	0.216	0.1
<b>Server Rack 2 Distance [-]</b>	0.829	0.509	0.4
<b>Server Rack 3 Distance [-]</b>	-	0.829	0.614
<b>Server Rack 4 Distance [-]</b>	-	-	0.829
<b>Server Rack 1 Size</b>	25.2 U	42 U	25.2 U
<b>Server Rack 2 Size</b>	58.8 U	25.2 U	58.8 U
<b>Server Rack 3 Size</b>	-	58.8 U	25.2 U
<b>Server Rack 4 Size</b>	-	-	58.8 U
<b>Optimal Heat Transfer [W]</b>	1613.42	1767.246	2478.211

Graphical illustrations of Table 5.9 are given in the following figures below. Note that the inlet was now located on the ceiling of the data centre, while the outlet was placed on the right wall of the data storage room.

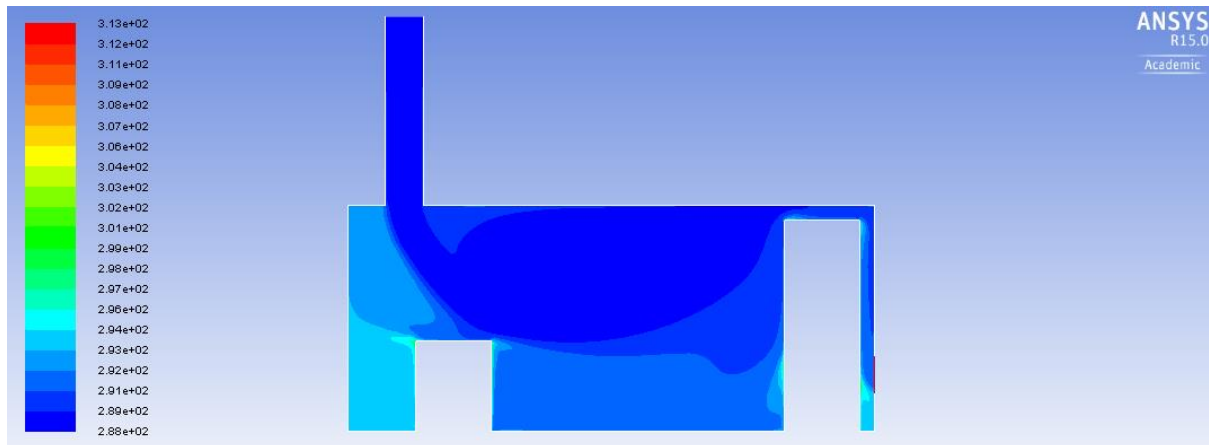


**Figure 5-20: Variable server height Case C 2 server racks temperature distribution**

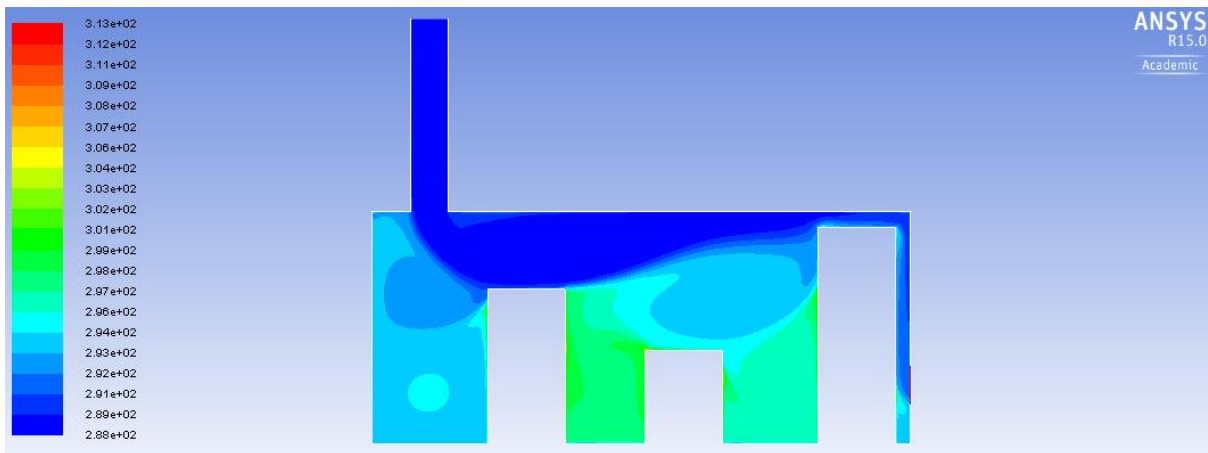


**Figure 5-21: Variable server height Case C 3 server racks temperature distribution**

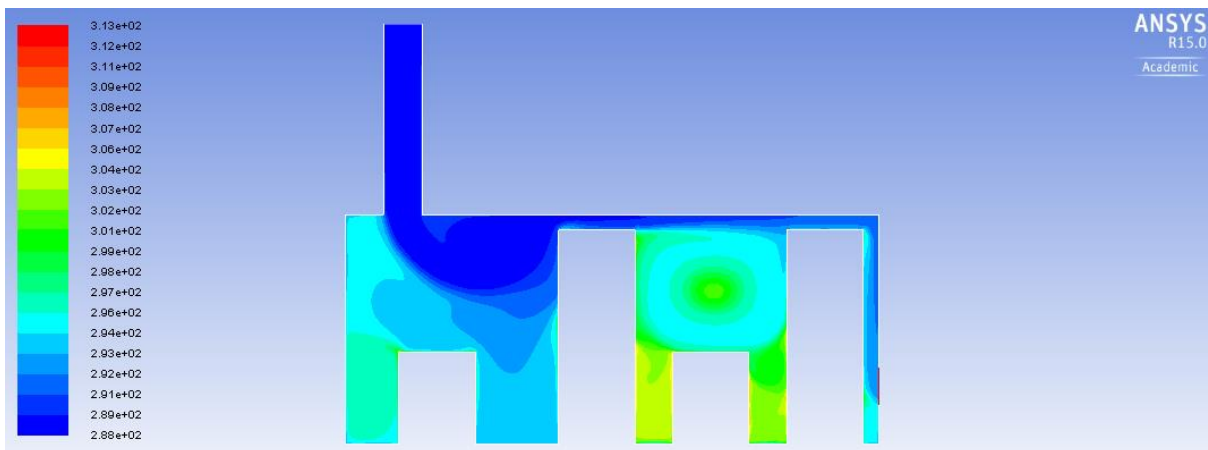


**Figure 5-22: Variable server height Case C 4 server racks temperature distribution**

From the figures above, it can be concluded that the first row of server racks should be placed relatively close to the left wall. For the case of two, three and four servers, the first server was placed slightly to the right of the inlet. This ensured that the first row of servers was in direct contact with the cool air supply to the room. The final row of server rack rows, in turn, should be placed as close to the outlet as possible (0.2 m). This was true for the case of two, three and four server rack rows.

The optimal inlet location proved to be (for all tested cases) as close to the left wall as possible. The inlet should therefore be placed at 0.5m or  $0.5/7 = 0.071$  (in non-dimensional format) from the left wall of the data centre. The outlet should be placed as close to the floor of the data centre at 0.5 m

or  $0.5/3 = 0.167$  in non-dimensional notation. This was the case for two, three or four server rack rows.

The heat transfer once again showed a dramatic increase with regard to the fixed server height scenario. The calculated heat transfer for the case of two server rack rows was 1 613.42 W. Adding server racks resulted in heat transfers of 1 767.246 W and 2 478.211 W for the case of three and four server rack rows respectively.

### 5.3.4 Comparison

After the optimal placements for the variable server height scenario were established, a comparison between the different cases was drawn up. The total amount of heat transfer again formed the basis of the comparison. With the heat transfer known, the different cases could be evaluated against each other to determine the optimal inlet and outlet placements. A comparison between all tested cases for the variable server heights scenario is presented in Figure 5-23 below.

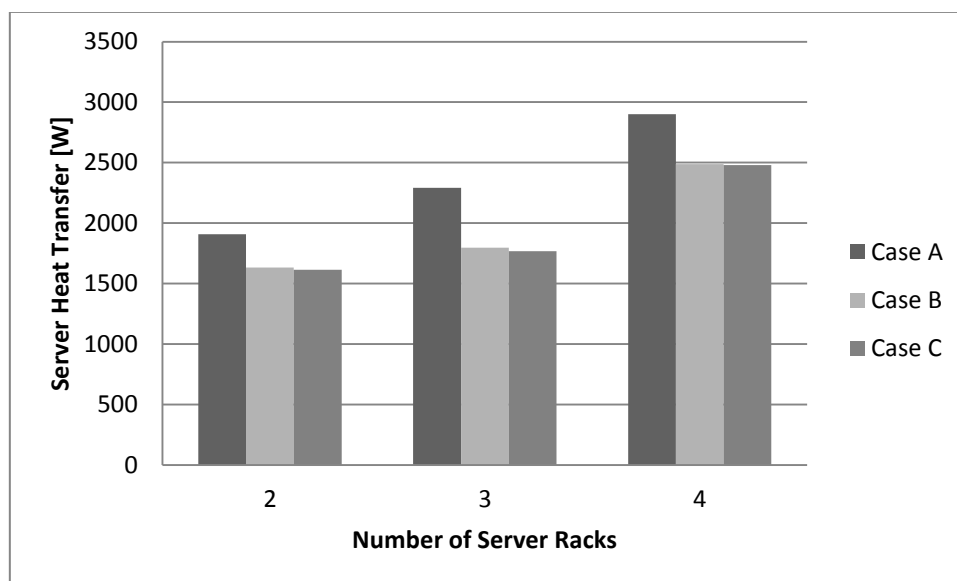


**Figure 5-23: Comparison between variable server height cases**

From Figure 5-23 above, it can be seen that, similar to the fixed server height scenario, Case A proved to have the highest amount of available heat transfer. It therefore became clear that the air-conditioning inlet and outlet should be placed on opposing walls of the data centre.

For the case of two server rack rows, Case A showed a 276.14 W increase over Case B. Case B, in turn, had an increase of approximately 19 W with regard to Case C.

When three rows of server racks were used, the difference between Case A and Case B increased even more. Case A showed an approximate 493.5 W increase over Case B. The difference between Case B and Case C was also slightly larger, with Case B exhibiting a 29.5 W increase in heat transfer over Case C.

Finally, the case of four server rack rows revealed the same trend as in both the previous numbers of server racks. Case A showed an increase of approximately 413 W with regard to Case B. Case B, in turn, had an approximate 9 W increase in heat transfer over Case C.

It was therefore safe to assume that Case A yielded the best results with respect to cooling the data centre. Case B proved to be the second best option, although the difference between Case B and C was not as significant.

It is interesting to note from the optimal placements and figures, that when two rows of server racks were used, one was as small as possible (25.2 U), while the other was as large as possible (58.8 U). This pattern was true for Cases A, B and C. It is also interesting to note that the smaller of the two should be placed at the inlet of the room. The larger rack proved to be efficient near the outlet of the data centre.

It was also found that when three server rack rows were used, one should be as small as possible (25.2 U), one as large as possible (58.8 U) and the third should be a standard 42 U rack. This was true for Case A, B and C, although the placements of the aforementioned racks differed between cases. For Case A (Figure 5-15), the 42 U rack should be placed close to the inlet of the room. The second server row should then be a 25.2 U rack, followed by the 58.8 U rack. Both the 25.2 U and 58.8 U racks should be placed near the outlet of the server room. The optimal placement for Case B (Figure 5-18) showed that the 58.8 U rack should be placed near the inlet of the room. The 25.2 U rack should be placed close to the outlet of the room, with the 42 U rack spaced in between these servers. Finally, Case C (Figure 5-21) showed that the 42 U rack should be placed at the inlet of the room. The 58.8 U server rack, in turn, was placed at the outlet of the room with the small 25.2 U rack placed approximately in the middle of the data centre.

The final observation was made for the case of four server rack rows. In this configuration, it was noted that the optimal solutions consisted of having two servers as small as possible (25.2 U) and two as large as possible (58.8 U). This proved true once again for Case A, B and C although the placement of these servers changed for the different cases. Case A (Figure 5-16) showed that the

first server should be a 58.8 U rack placed close to the inlet of the room. The next two servers should both be 25.2 U racks. Finally, the last server should be a 58.8 U rack and should be placed close to the outlet of the room. Case B (Figure 5-19) showed that the first server should be placed close to the inlet and should be a 58.8 U rack. The second, third and fourth servers should be 25.2 U, 58.8 U and 28.8 U racks respectively, with the last being close to the outlet once again. Finally, the optimal placements for Case C (Figure 5-22) suggested that the first, second, third and fourth servers should be 25.2 U, 58.8 U, 25.2 U and 58.8 U racks respectively. This first row of server racks should once again be placed at the inlet of the server room, while the last row should be placed at the outlet.

## 5.4 Conclusion

In total, approximately 3 070 simulations were needed in order to determine the optimal placements of the server racks in a data centre. The simulations included both fixed server heights, as well as variable server heights.

For both the fixed and variable server height scenarios, Case A proved to be the best strategy with regard to cooling the server room, with only one exception. When a single row of server racks was used, Case C proved to be the better option for the fixed server height scenario (although the difference between Cases A and C was not significant). Figure 5-24 below shows a heat transfer comparison of all the tested cases.

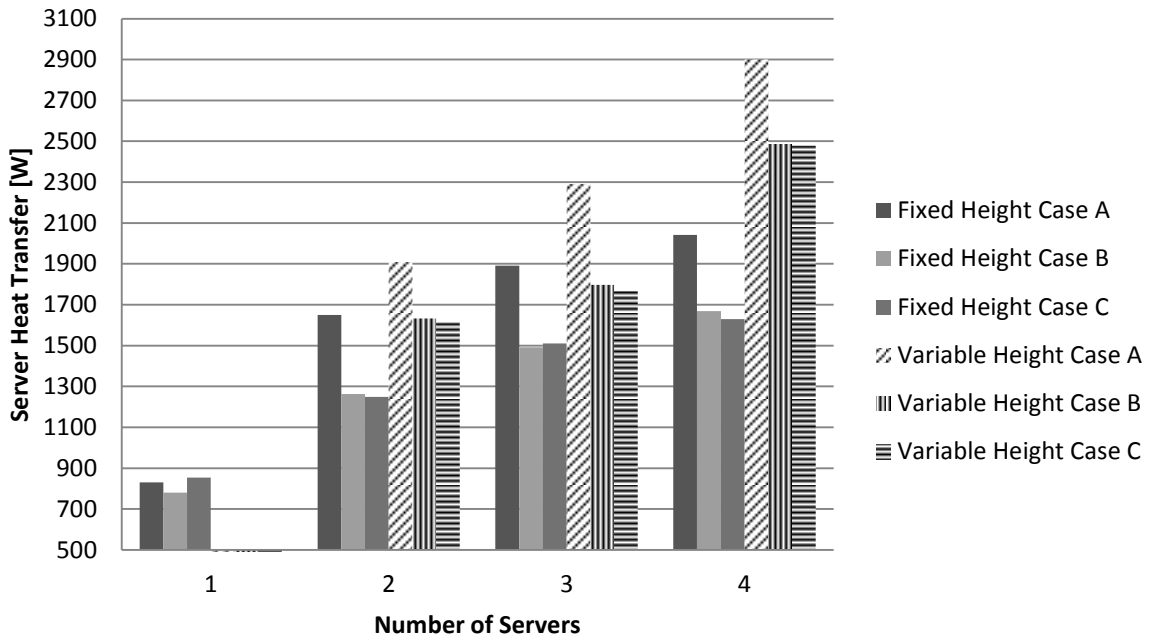


**Figure 5-24: Server heat transfer comparison of all tested cases**

Although the optimal distribution of the discrete heat sources in a two-dimensional data centre was determined, it was still necessary to do a sensitivity check. This would give a clear indication of the design parameters that had the largest impact on the solutions. In order to check the sensitivities of the design parameters, a Case A variable server rack height geometry was selected. All design parameters were then given a 10%, 20% and 30% increasing perturbation respectively and the change in total heat transfer was recorded. Figure 5-25 below shows the geometry that was used to determine the sensitivities.

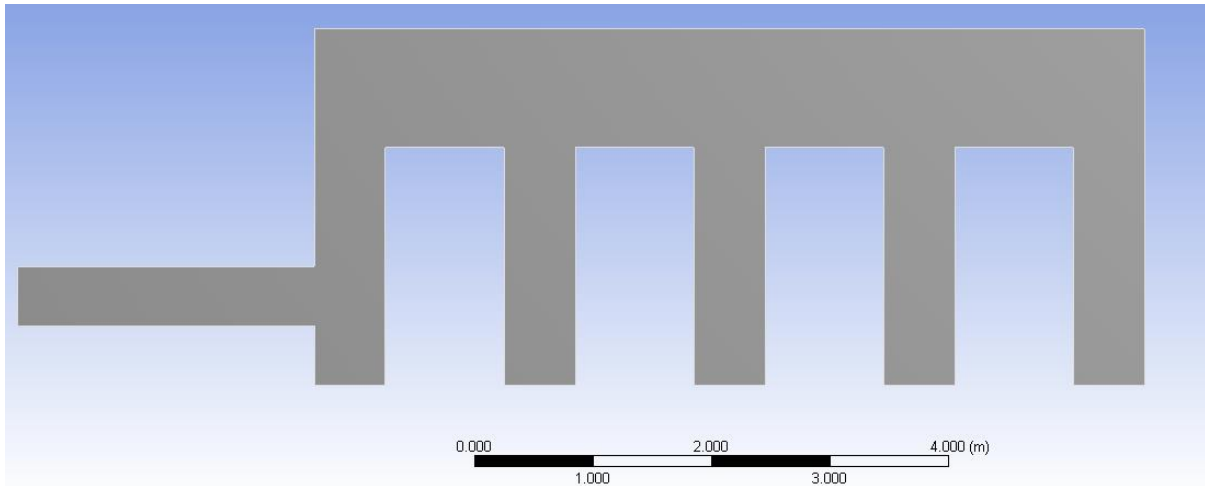


**Figure 5-25: Geometry used to determine input sensitivities**

Note that in Figure 5-25, all the servers were spaced exactly 0.6 metres apart and all servers started off as 42 U servers. The inlet and outlet of the data centre were located 0.5 metres from the floor of the server room. The total heat transfer from the server panels to the ambient air was calculated to be 1 375.713 W. The inlet was now moved to 0.55 m, 0.6 m and 0.65 respectively, while all other design parameters were kept constant. The same process was then repeated for each individual design parameter. Figure 5-26 below shows the impact of a change in a design parameter on the obtainable heat transfer of the system.

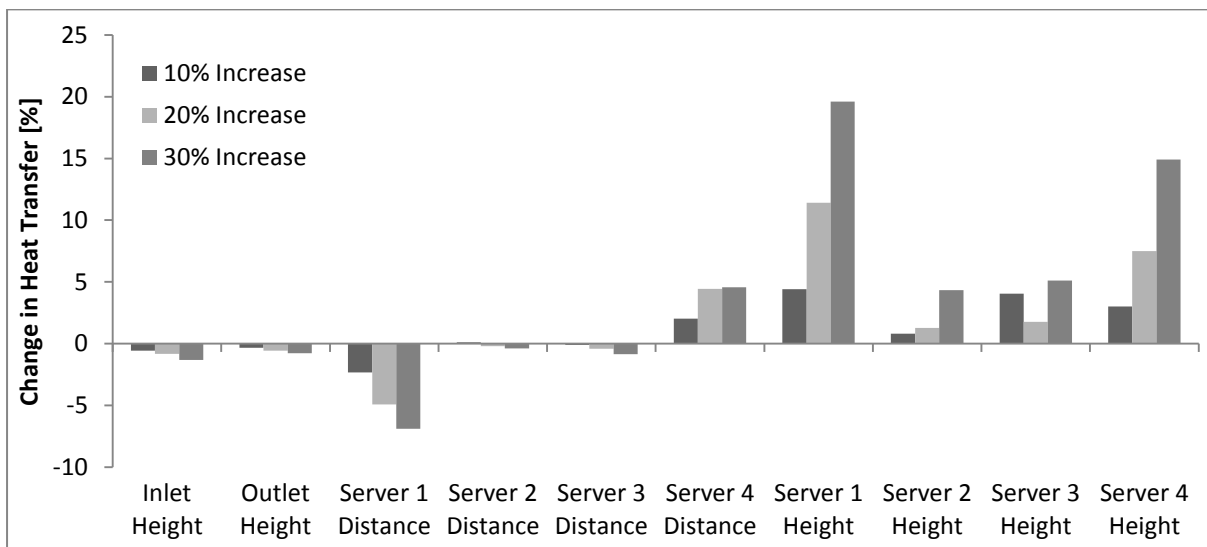


**Figure 5-26: Sensitivity analysis of design parameters**



The results from the sensitivity analysis supported the outcome of the simulations. From the sensitivity analysis, it can be seen that the first and last server (Server 1 and 4) distances have a large impact on the obtainable heat transfer. The first and last server heights proved to have the highest impact on the heat transfer as seen in Figure 5-26 above. From Figure 5-26, it can be seen that a 20% height increase in Server 1 would result in an 11% increase in the obtainable heat transfer of the system. These input parameters are so important because they dictate the manner in which the cool air flows throughout the data centre. The sensitivity analysis therefore supports the answers obtained by means of the optimisation process.

## 6 Conclusions and recommendations

The study showed that by using a numerical approach, the optimal distribution of discrete heat sources (server racks) in a two-dimensional data centre could be determined. The first step of the study was a review of literature involving heat source optimisation as well as data centre cooling strategies. Various numerical models and approaches were studied in order to determine an appropriate solution strategy.

After the literature study was completed, a solution strategy was chosen. Ansys Fluent was used to solve the CFD code. After realistic dimensions for the server room, server racks, inlets and outlets were chosen, a geometry was created using Ansys DesignModeler. The geometry next underwent meshing at which stage inflation layers were added to refine the mesh. Inflation layers were added to the mesh in regions where high gradients (or differences) were expected in order to accurately solve these regions.

The next step was the addition of boundary conditions and initial values. It was quickly determined that turbulent flow of air in the data centre was expected and various turbulence models were investigated. By consulting previous articles, it was decided to use a Reynolds-averaged Navier-Stokes (RANS) turbulence model. The  $k-\epsilon$  realisable transport equations were used to solve the RANS equations. The governing equations were therefore solved using the finite volume method.

The numerical solver was validated to ensure that the model would in fact yield accurate results. The values obtained by the numerical solver were in good agreement with the experimental results, showing an error of less than 6%.

An optimisation algorithm was applied in order to find the optimum server placements. A goal-driven optimisation approach was followed using a response surface. The main objective function was to maximise the heat transfer from the servers to the ambient air. The heat transfer would therefore serve as an indication of how effectively the supplied cool air would be in contact with the warm server panels.

The optimal locations for various numbers of server rack rows, as well as inlet and outlet locations for three different cases were determined. The optimal locations were first established for server racks having the same height. After the optimal locations for the fixed server height scenario were determined, the effect of varying the server heights was also investigated and the optimal locations

were subsequently determined. It was found that the air-conditioning inlet and outlet should be placed on opposing walls of the data centre to maximise cooling.

A sensitivity analysis was also conducted to determine the effect of a change in design parameter on the outcome of the solution. The sensitivity analysis supported the results obtained by means of the optimisation process.

The author recommends that the following be changed or included in future studies:

- Conduct a three-dimensional study using the same approach as this study.
- Investigate the effects of modelling the server racks as porous media. This can be achieved by including internal heat generation, a porous media as well as inlet and outlet fans on the server racks themselves.
- Investigate different objective functions such as minimum room temperature.
- Investigate the effects of adding more servers to the data centre.
- Investigate the effects of using a larger data centre.

## References

1. Çengel, Y.A., *Heat and Mass Transfer: A Practical Approach* 2006: McGraw-Hill.
2. Bash, C.E., C.D. Patel, and R.K. Sharma, *Efficient thermal management of data centers - Immediate and long-term research needs*. HVAC and R Research, 2003. 9(2): p. 137-152.
3. Shah, A.J., et al., *Exergy analysis of data center thermal management systems*. Journal of Heat Transfer, 2008. 130(2).
4. Patel, C.D., et al. *Thermal considerations in cooling large scale high compute density data centers*. in *Thermomechanical Phenomena in Electronic Systems -Proceedings of the Intersociety Conference*. 2002.
5. Schmidt, R.R. and M. Iyengar, *Best practices for data center thermal and energy management - Review of literature*. ASHRAE Transactions, 2007. 113 PART 1: p. 206-218.
6. Schmidt, R.R., E.E. Cruz, and M.K. Iyengar, *Challenges of data center thermal management*. IBM Journal of Research and Development, 2005. 49(4-5): p. 709-723.
7. Rasmussen, N., *Raised Floors vs Hard Floors for Data Center Applications*. APC White Paper # 19 (Revision 3), 2014.
8. Herrlin, M.K. *Rack cooling effectiveness in data centers and telecom central offices: The Rack Cooling Index (RCI)*. in *ASHRAE Transactions*. 2005.
9. Sorell, V., S. Escalante, and J. Yang. *Comparison of overhead and underfloor air delivery systems in a data center environment using CFD modeling*. in *ASHRAE Transactions*. 2005.
10. Patel, C.D., et al. *Computational Fluid Dynamics Modeling of High Compute Density Data Centers to Assure System Inlet Air Specifications*. in *Advances in Electronic Packaging*. 2001.
11. Zhai, Z., et al., *Evaluation of various turbulence models in predicting airflow and turbulence in enclosed environments by CFD: Part 1 - Summary of prevalent turbulence models*. HVAC and R Research, 2007. 13(6): p. 853-870.
12. Jones, P.J. and G.E. Whittle, *Computational fluid dynamics for building air flow prediction-current status and capabilities*. Building and Environment, 1992. 27(3): p. 321-338.
13. Chen, Q. and J. Srebric, *A procedure for verification, validation, and reporting of indoor environment CFD analyses*. HVAC and R Research, 2002. 8(2): p. 201-216.
14. Launder, B.E. and D.B. Spalding, *The numerical computation of turbulent flows*. Computer Methods in Applied Mechanics and Engineering, 1974. 3(2): p. 269-289.
15. Yakhot, V., et al., *Development of turbulence models for shear flows by a double expansion technique*. Physics of Fluids A, 1992. 4(7): p. 1510-1520.

16. Shih, T.H., et al., *A new  $k$ - $\epsilon$  eddy viscosity model for high reynolds number turbulent flows*. Computers and Fluids, 1995. 24(3): p. 227-238.
17. Lu, W., A.T. Howarth, and A.P. Jeary, *Prediction of airflow and temperature field in a room with convective heat source*. Building and Environment, 1997. 32(6): p. 541-550.
18. Zhang, Z., et al., *Evaluation of various turbulence models in predicting airflow and turbulence in enclosed environments by CFD: Part 2 - Comparison with experimental data from literature*. HVAC and R Research, 2007. 13(6): p. 871-886.
19. Abanto, J., et al., *Airflow modelling in a computer room*. Building and Environment, 2004. 39(12): p. 1393-1402.
20. Arora, J.S., *Introduction to Optimum Design*2011: Academic Press.
21. da Silva, A.K., S. Lorente, and A. Bejan, *Optimal distribution of discrete heat sources on a plate with laminar forced convection*. International Journal of Heat and Mass Transfer, 2004. 47(10-11): p. 2139-2148.
22. da Silva, A.K., S. Lorente, and A. Bejan, *Optimal distribution of discrete heat sources on a wall with natural convection*. International Journal of Heat and Mass Transfer, 2004. 47(2): p. 203-214.
23. Radhakrishnan, T.V., C. Balaji, and S.P. Venkateshan, *Optimization of multiple heaters in a vented enclosure - A combined numerical and experimental study*. International Journal of Thermal Sciences, 2010. 49(4): p. 721-732.
24. Versteeg, H.K. and W. Malalasekera, *An Introduction to Computational Fluid Dynamics: The Finite Volume Method*2007: Pearson Education Limited.
25. Wei, X., et al. *Functional Electrical Stimulation as a Neuroprosthetic Methodology for Enabling Closed-loop Urinary Incontinence Treatment*. in *5th International IEEE EMBS Conference on Neural Engineering*. 2011. Cancun, Mexico.
26. IBM. *Rack cabinets and options* [Online] [cited 2015 10 January]; Available from: <http://www-03.ibm.com/systems/xbc/cog/rackcabinetsoptions/rackcabinetsoptions.html>.
27. Franke, J., et al., *The Best Practice Guideline for the CFD simulation of flows in the urban environment: an outcome of COST 732*, in *The Fifth International Symposium on Computational Wind Engineering*2010: Chapel Hill, North Carolina, USA.
28. Chuang, S.H., J.S. Chiang, and Y.M. Kuo, *Numerical simulation of heat transfer in a three-dimensional enclosure with three chips in various position arrangements*. Heat Transfer Engineering, 2003. 24(2): p. 42-59.
29. Calcagni, B., F. Marsili, and M. Paroncini, *Natural convective heat transfer in square enclosures heated from below*. Applied Thermal Engineering, 2005. 25(16): p. 2522-2531.

30. Heindel, T.J., F.P. Incropera, and S. Ramadhyani, *Enhancement of natural convection heat transfer from an array of discrete heat sources*. International Journal of Heat and Mass Transfer, 1996. 39(3): p. 479-490.
31. Fluent Inc., *Ansys FLUENT User's Guide Version 14.0 Release*, 2011
32. Borgnakke, C. and R.E. Sonntag, *Fundamentals of Thermodynamics* 2009: Wiley.
33. Blay, D., S. Mergui, and C. Niculae. *Confined turbulent mixed convection in the presence of a horizontal buoyant wall jet*. in *American Society of Mechanical Engineers, Heat Transfer Division, (Publication) HTD*. 1992.
34. Boukhanouf, R. and A. Haddad, *A CFD analysis of an electronics cooling enclosure for application in telecommunication systems*. Applied Thermal Engineering, 2010. 30(16): p. 2426-2434.

# I. Annexure A- Velocity vector plots

## Fixed server height simulations

Case A

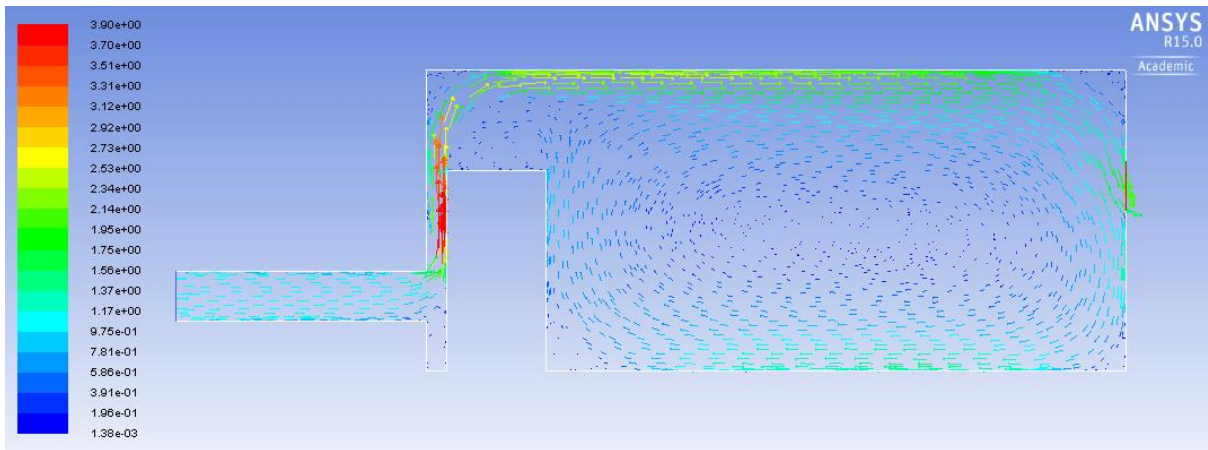


Figure I-1: Fixed server height Case A 1 server rack velocity vector plot

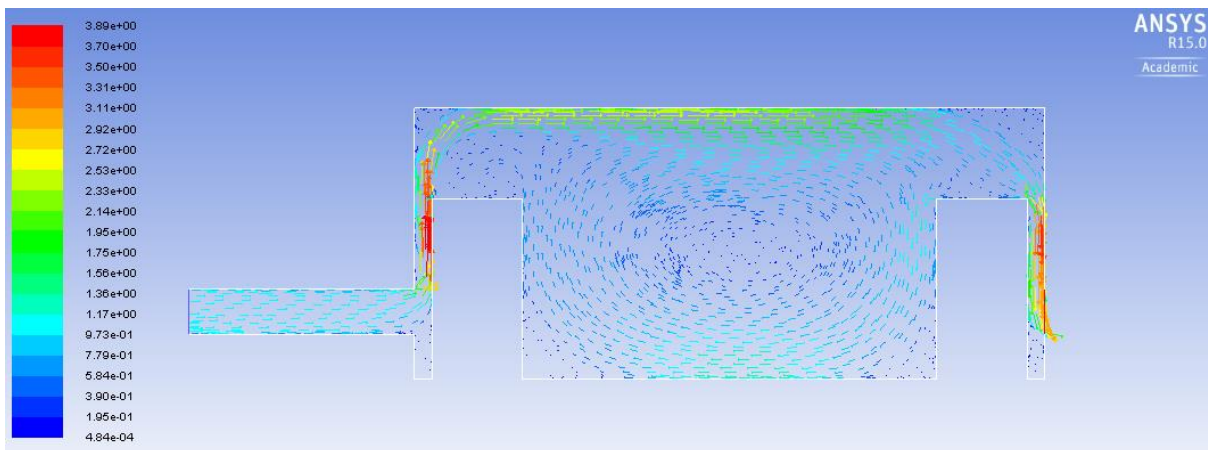


Figure I-2: Fixed server height Case A 2 server racks velocity vector plot



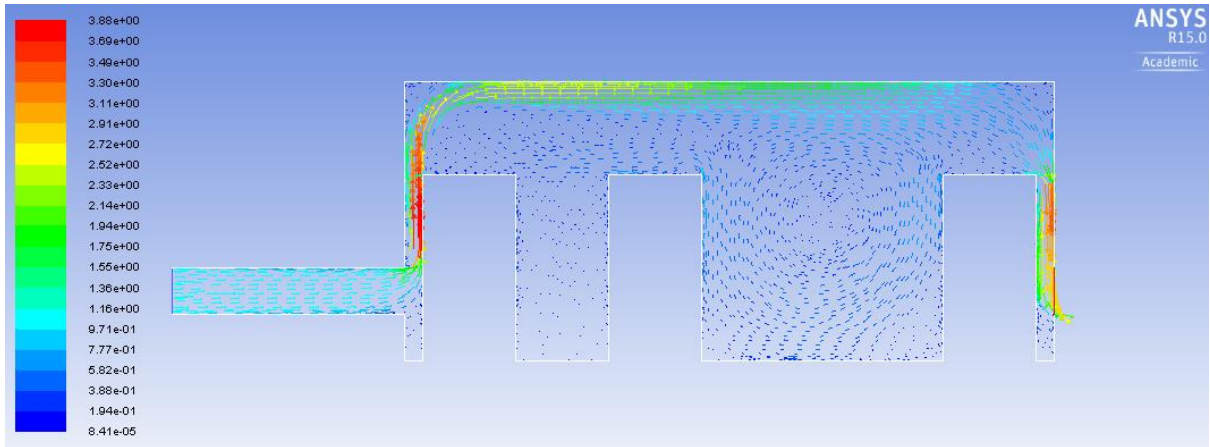


Figure I-3: Fixed server height Case A 3 server racks velocity vector plot

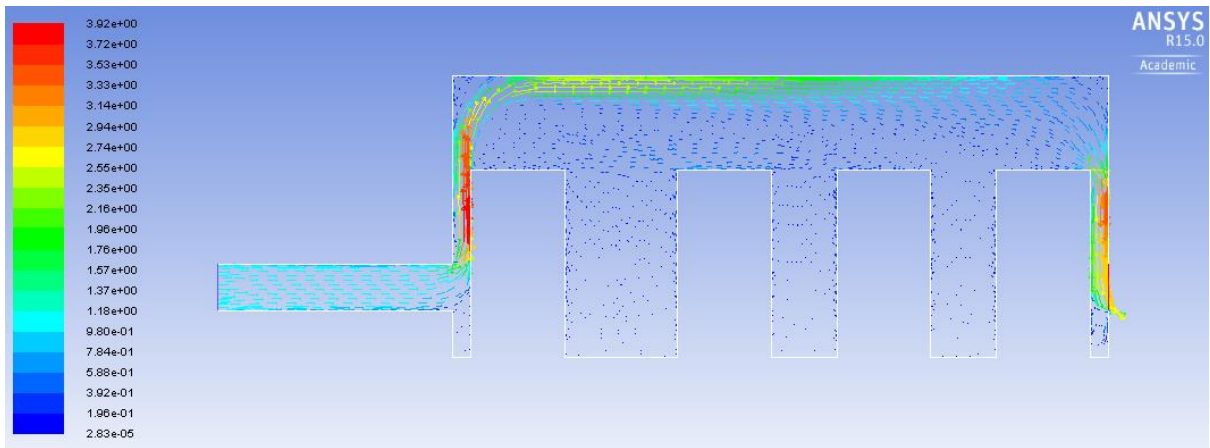


Figure I-4: Fixed server height Case A 4 server racks velocity vector plot

Case B

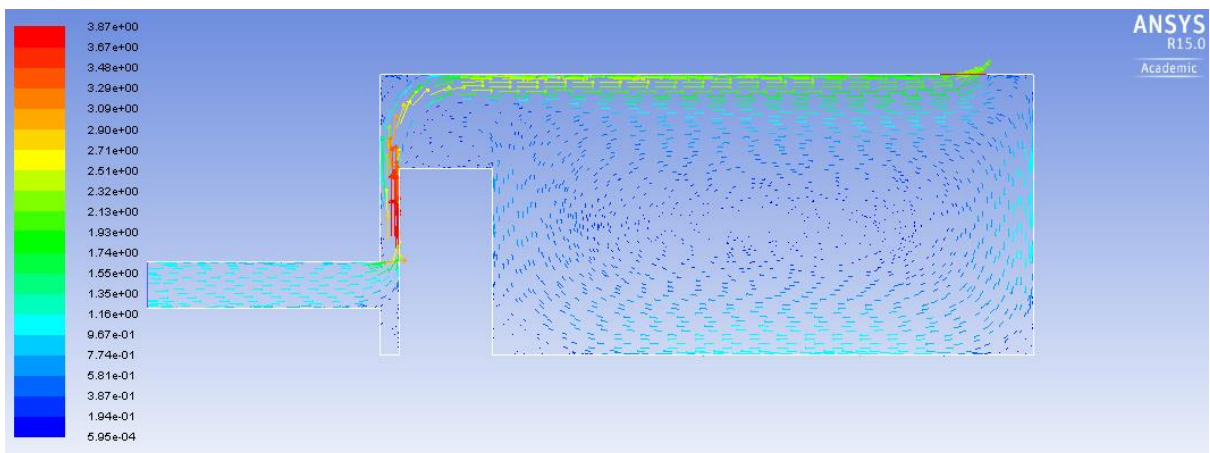


Figure I-5: Fixed server height Case B 1 server rack velocity vector plot



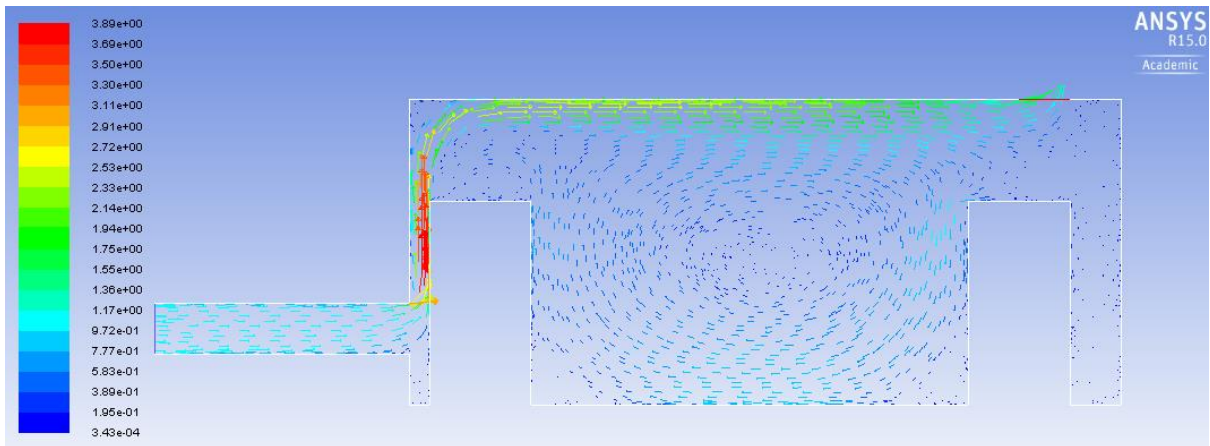


Figure I-6: Fixed server height Case B 2 server racks velocity vector plot

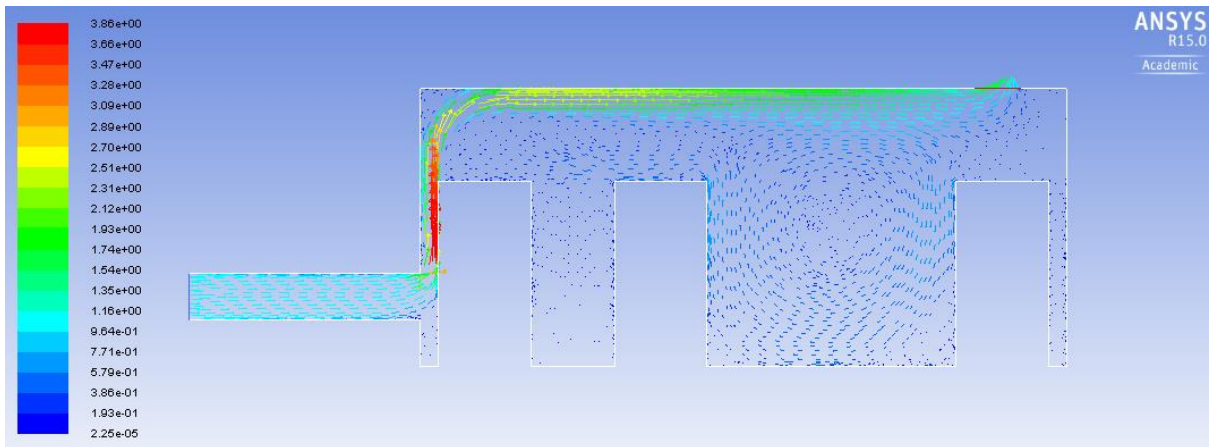


Figure I-7: Fixed server height Case B 3 server racks velocity vector plot

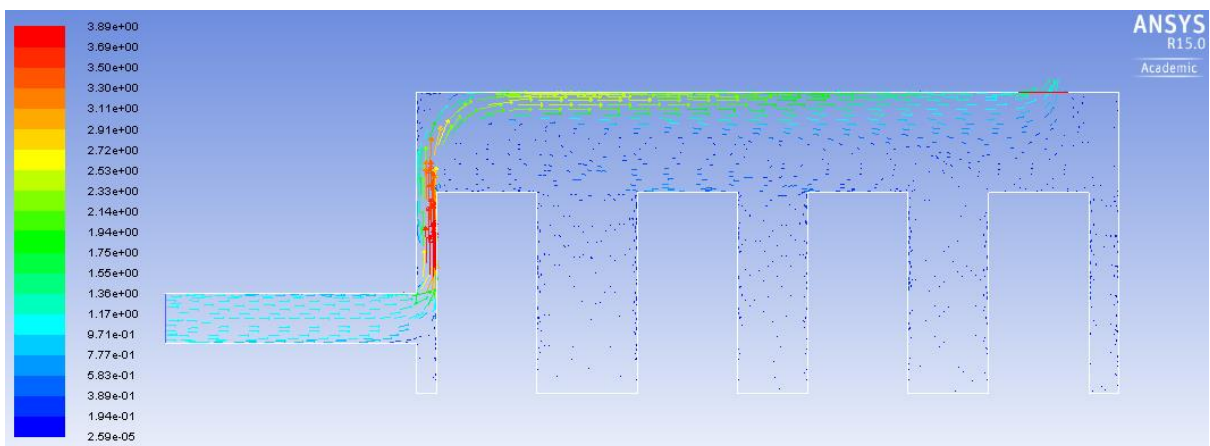


Figure I-8: Fixed server height Case B 4 server racks velocity vector plot

Case C

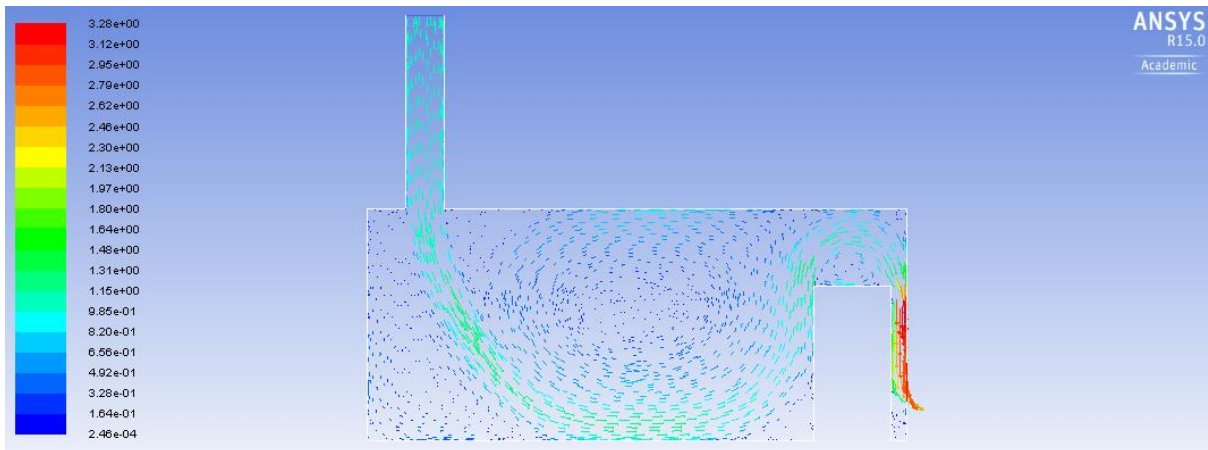


Figure I-9: Fixed server height Case C 1 server rack velocity vector plot

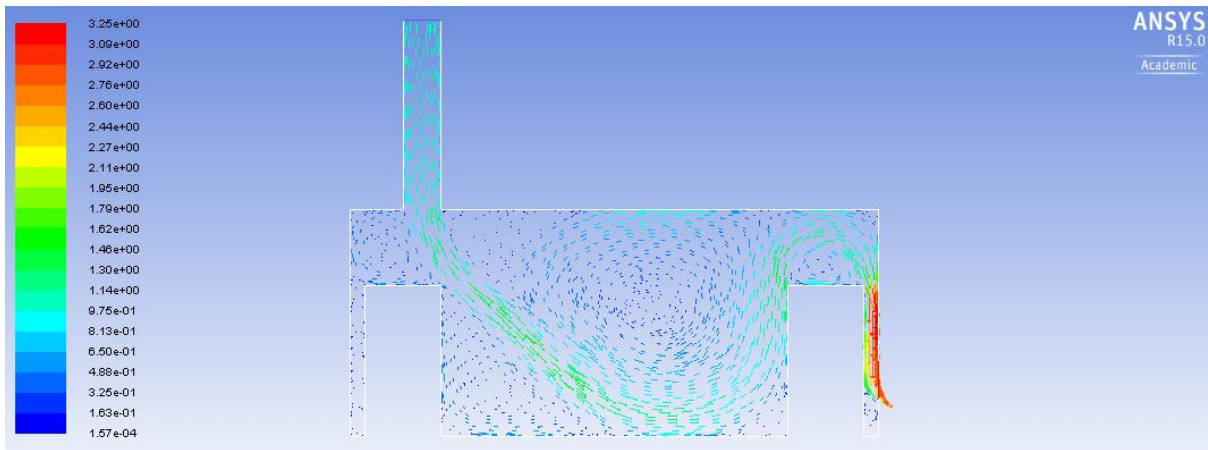


Figure I-10: Fixed server height Case C 2 server racks velocity vector plot

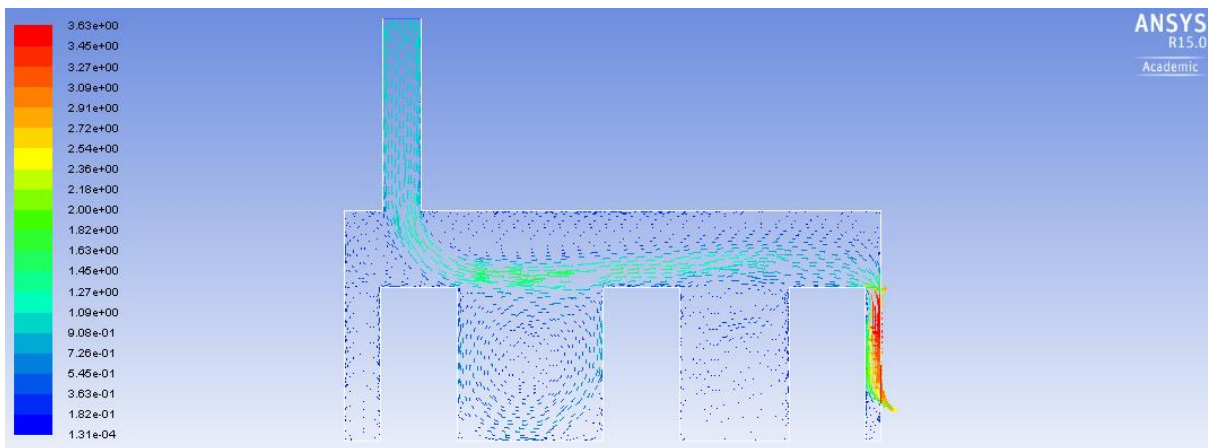


Figure I-11: Fixed server height Case C 3 server racks velocity vector plot

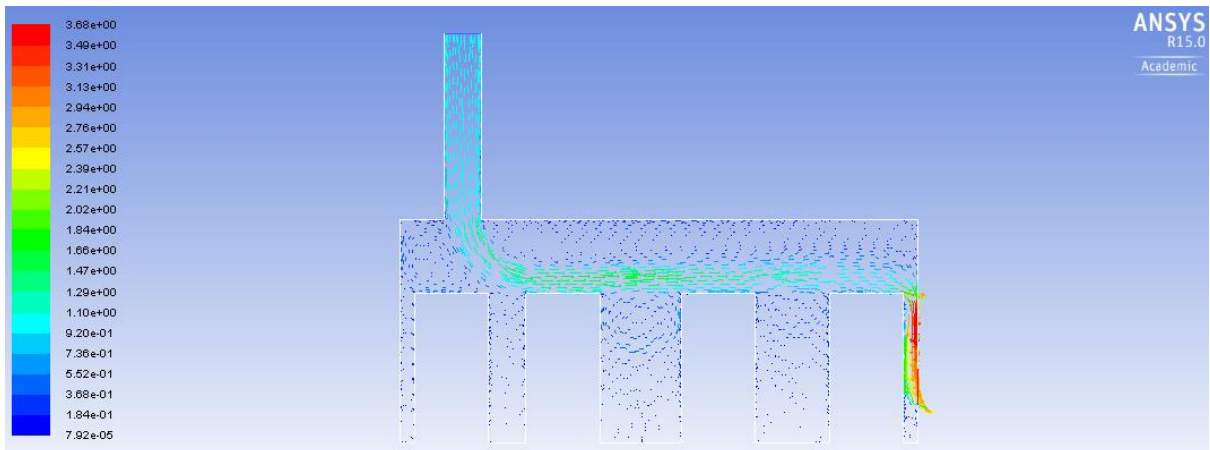


Figure I-12: Fixed server height Case C 4 server racks velocity vector plot

## Variable server height simulations

Case A

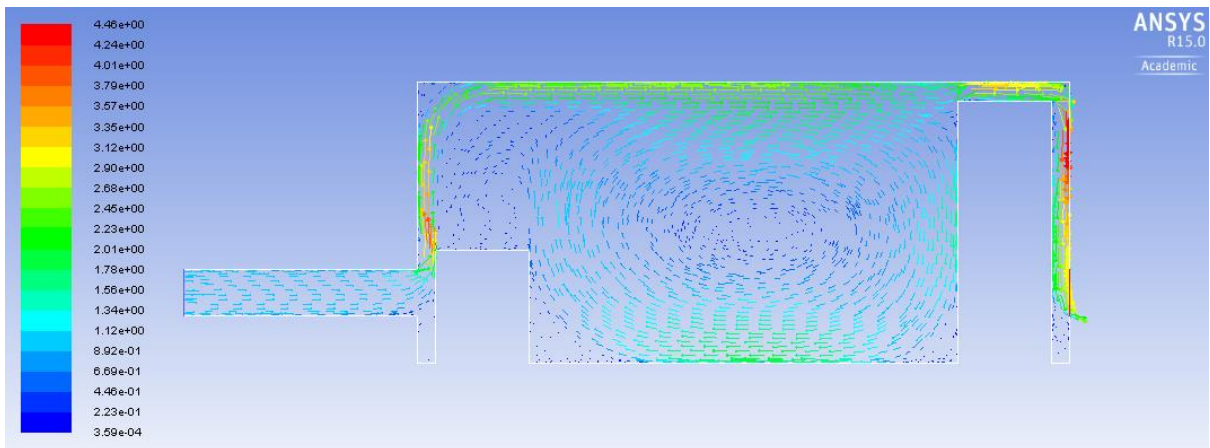


Figure I-13: Variable server height Case A 2 server racks velocity vector plot



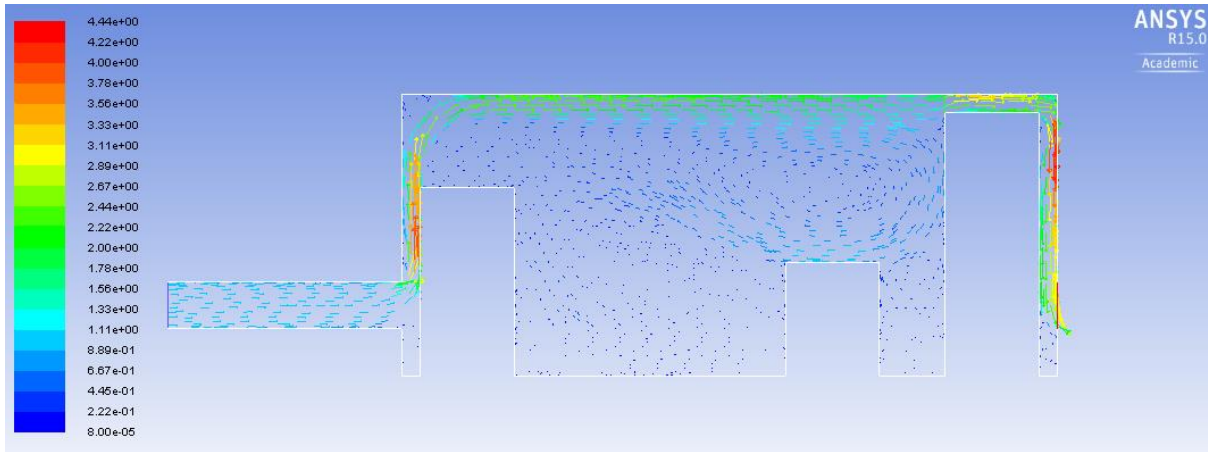


Figure I-14: Variable server height Case A 3 server racks velocity vector plot

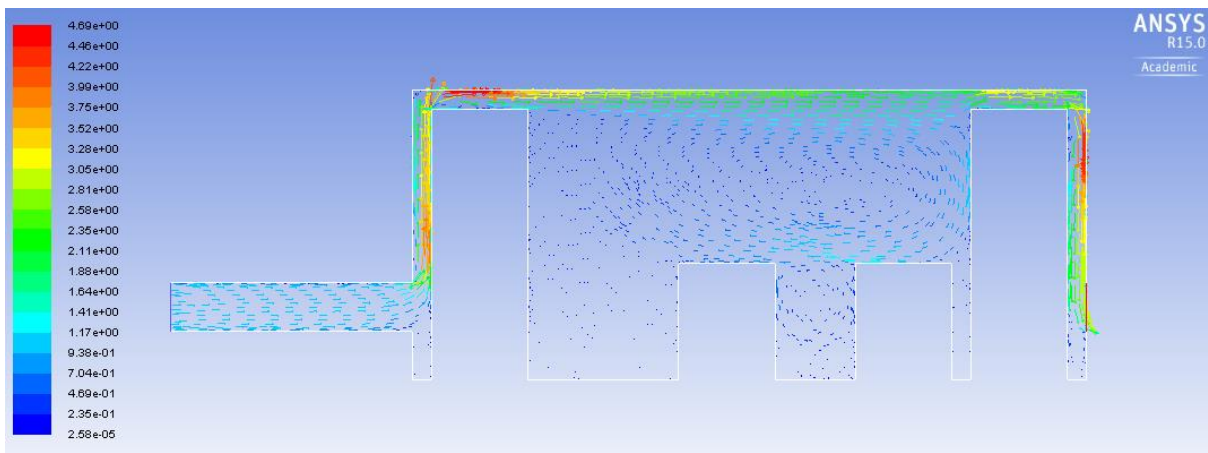


Figure I-15: Variable server height Case A 4 server racks velocity vector plot

Case B

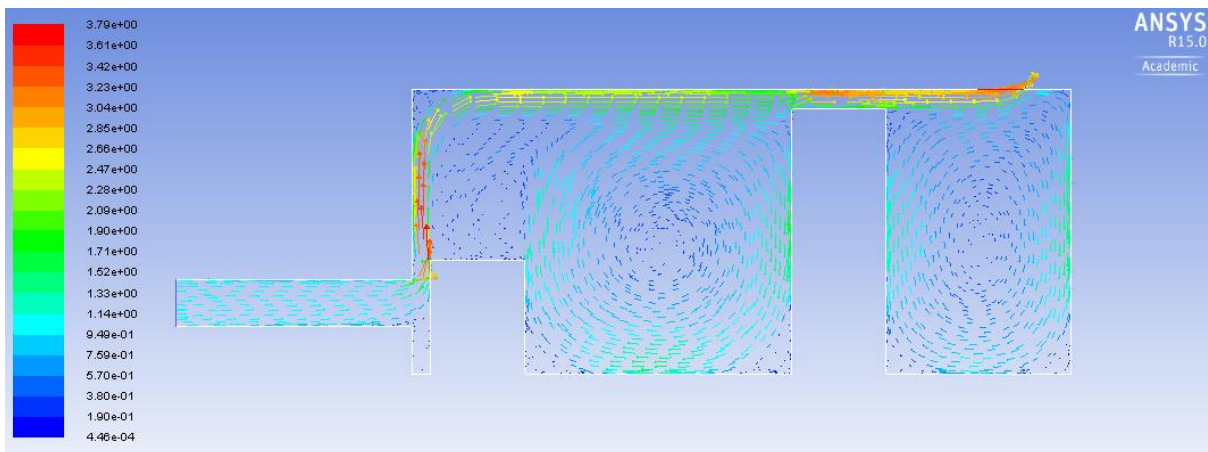


Figure I-16: Variable server height Case B 2 server racks velocity vector plot

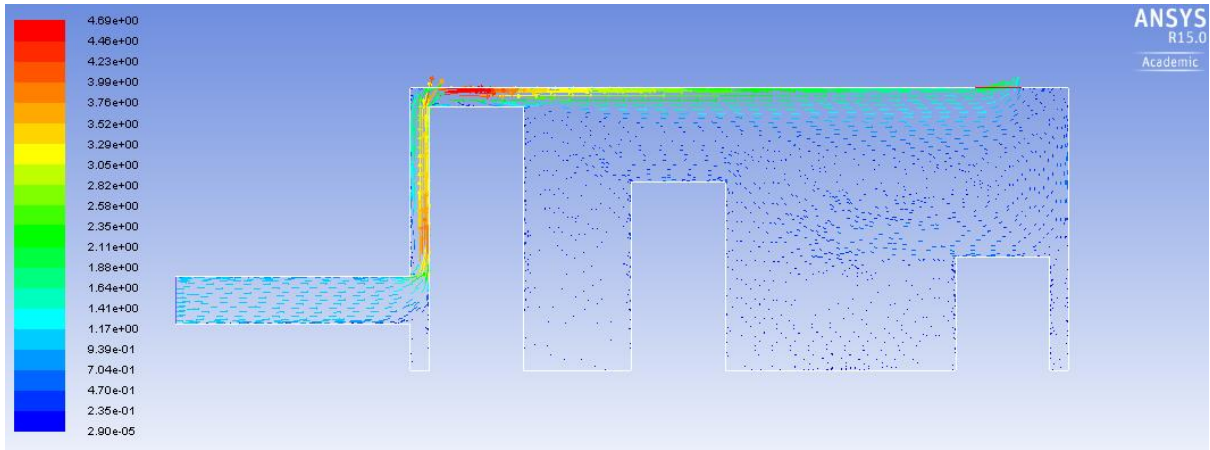


Figure I-17: Variable server height Case B 3 server racks velocity vector plot

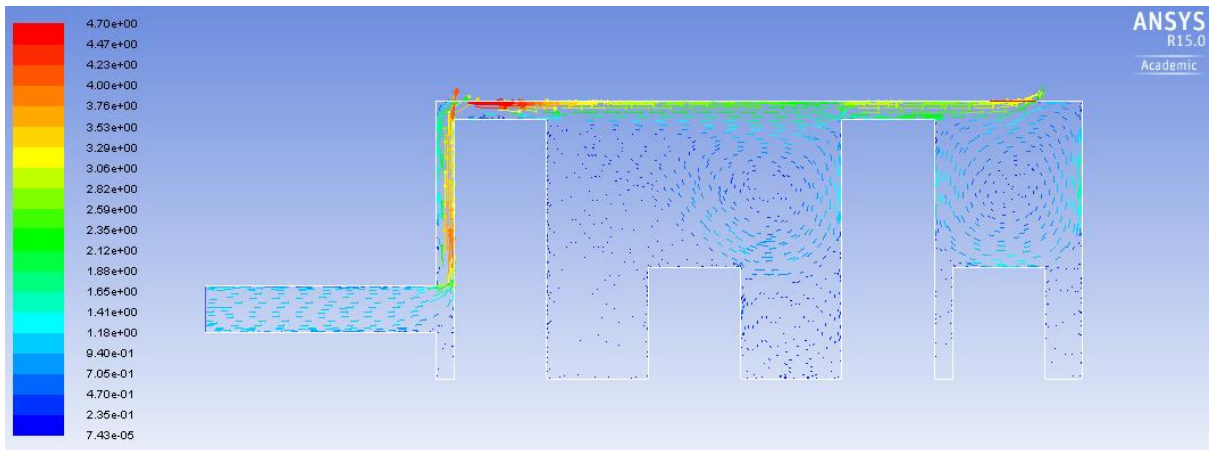


Figure I-18: Variable server height Case B 4 server racks velocity vector plot

Case C

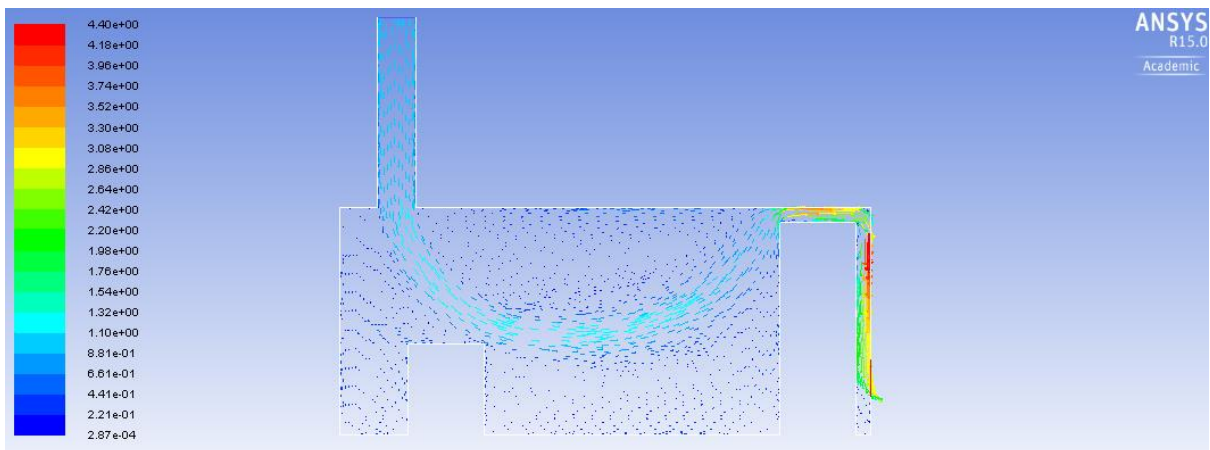


Figure I-19: Variable server height Case C 2 server racks velocity vector plot

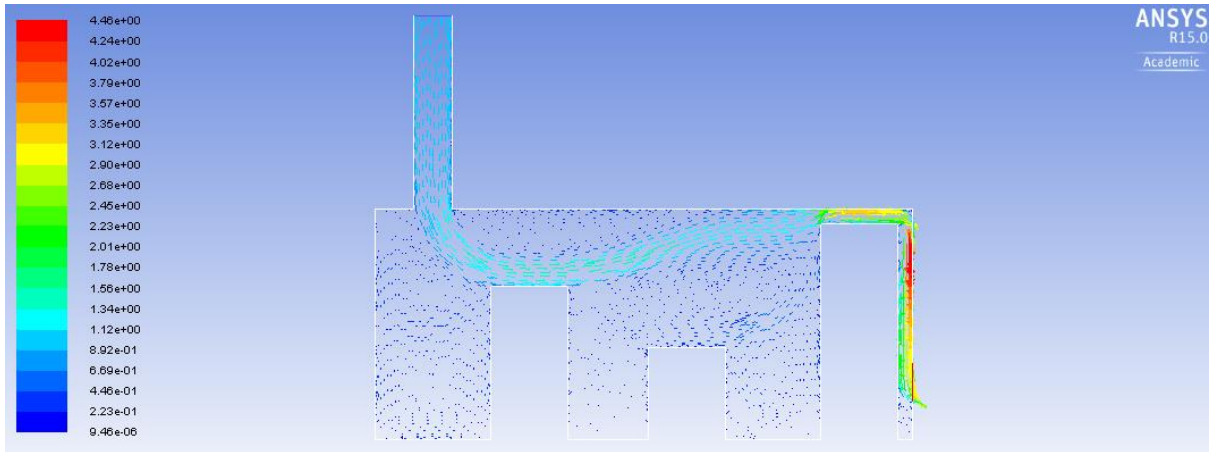


Figure I-20: Variable server height Case C 3 server racks velocity vector plot

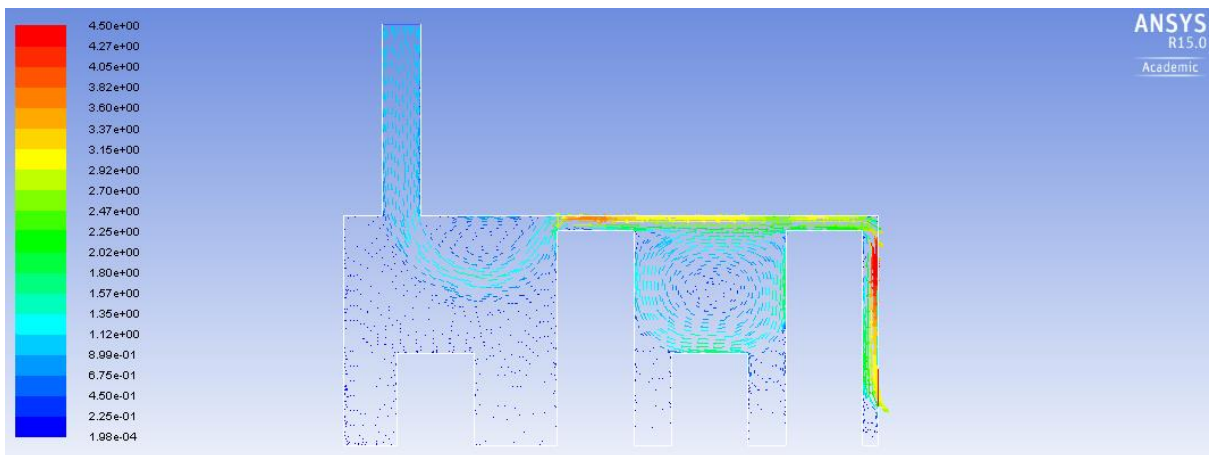


Figure I-21: Variable server height Case C 4 server racks velocity vector plot